Universität Potsdam

MASTERARBEIT

Origin of the SERS Background and its Potential as Nanothermometer

Jan Kutschera

Matrikel-Nr. 767752

eingereicht im Studiengang

Master of Science
Physik

Universität Potsdam
Institut für Physik und Astronomie

im Oktober 2023

Diese Arbeit entstand in Zusammenarbeit mit der Arbeitsgruppe

Ultraschnelle Dynamik in kondensierter Materie

1. Gutachter:

Prof. Dr. Matias Bargheer

2. Gutachterin:

Prof. Dr. Svetlana Santer

Contents

Kurzfassung

Die oberflächenverstärkte Raman-Spektroskopie (SERS) ist seit mehreren Jahrzehnten ein wertvolles Werkzeug in der biochemischen Sensorik, der Detektion von Einzelmolekülen und der Photokatalyse. Die molekularen Fingerabdrücke in SERS-Spektren sind immer von einem breiten Hintergrund begleitet, der von den plasmonischen Nanopartikeln stammt. Das Verständnis dieser Nanopartikelreaktion ist entscheidend, um die Mechanismen hinter plasmonenverstärkten Phänomenen wie Photochemie, Photovoltaik und Magnetismus zu begreifen. Während die Diskussion über die zugrunde liegenden Prozesse dieses Nanopartikelsignals andauert, liefert diese Arbeit Einblicke in die Rolle der Interbandübergänge bei der Entstehung des SERS-Hintergrunds unter Verwendung von Photolumineszenzanregungsspektroskopie (PLE).
Des Weiteren können die Temperaturen der Nanopartikel und ihrer unmittelbaren Umgebung aus dem Anti-Stokes SERS-Hintergrund ermittelt werden. Hier wurden bestehende Anti-Stokes-Thermometrietechniken erweitert, um konsistente Temperaturmessungen über verschiedene Nanopartikelcluster auf inhomogenen Proben hinweg durchführen zu können. Dies ermöglicht die gleichzeitige Messung von chemischen Reaktionen und Temperaturen in Cluster-Systemen mit hoher Photokatalyseaktivität.
Zuletzt wurde ein Abklingen des SERS-Hintergrunds im Verlauf von wenigen Minuten beobachtet. Dieses Phänomen wird vermutlich durch Elektronentransfers von den Nanopartikeln in die Umgebung verursacht. Diese Arbeit präsentiert erste Ergebnisse zu der Abhängigkeit der Hintergrundabnahme von verschiedenen Eigenschaften. Auf Grundlage dieser Ergebnisse werden weitere Experimente vorgeschlagen.

Abstract

Surface-enhanced Raman spectroscopy (SERS) has been a valuable tool in biochemical sensing, single-molecule detection, and photocatalysis for several decades. The molecular fingerprints in SERS spectra are always accompanied by a broad background originating from the plasmonic nanoparticles. Understanding this nanoparticle response is crucial for comprehending the mechanisms behind plasmonic-enhanced phenomena such as photochemistry, photovoltaic, and magnetism. While the discussion regarding the underlying processes of this nanoparticle response is ongoing, this thesis provides insights into the role of interband transitions in the creation of the SERS background, utilizing photoluminescence excitation (PLE) spectroscopy.
Furthermore, the temperatures of the nanoparticles and their close environment can be determined from the anti-Stokes SERS background. Here, existing anti-Stokes thermometry techniques have been extended to accomplish consistent temperature measurements across various nanoparticle clusters on inhomogeneous samples. This enables simultaneous measurements of chemical reactions and temperatures in clustered systems with high photocatalytic activity.
At last, a decay in the SERS background on the timescale of a few minutes was observed. This phenomenon is suspected to result from electron transfers from the nanoparticles into the environment. This thesis presents initial results regarding the dependencies of this decay on multiple properties. Based on these results further experiments are suggested.

Chapter 1

Introduction

Nearly half a century after the first observation of Raman spectra on a roughened silver surface by Fleischmann, Hendra, and McQuillan [35] in 1974 and the introduction of surface-enhanced Raman spectroscopy (SERS) by Jeanmaire and van Duyne [54] three years later, SERS is an essential tool for biochemical sensing [27, 31, 42, 66, 92], single-molecule detection [24, 60, 65, 70, 104, 106], and photocatalysis [10, 11, 18, 47, 59, 63, 86, 96, 99, 102, 106].
Metal nanoparticles show substantial enhancement of electromagnetic fields, scattering, and absorption due to their localized surface plasmon resonance (LSPR), enabling SERS [2, 92]. The LSPR is a characteristic of the shape, size, and material of the nanoparticles as well as the environment [2, 88, 92].
The group for ultrafast dynamics in condensed matter at the University of Potsdam uses gold nanoflowers [63, 83] among others. Gold nanoparticles, in general, offer optical enhancements in the visual light regime [85], but high-faceted particles, like nanoflowers, show even higher enhancement factors in SERS measurements, aid molecule adsorption, and are more active in photocatalytic reactions [14, 68, 96]. This increases even further if they are clustered [37, 39, 65, 76, 90]. Therefore, the main focus of this thesis is on clustered gold nanoflower samples.
A typical SERS spectrum of 4-Nitrothiophenol (4-NTP) coated on a gold nanoflower substrate is illustrated in Figure 1.1. SERS spectra contain two main features. Firstly, they show narrow peaks that can be assigned to the vibrational modes of molecules adsorbed to the nanoparticle surfaces. Hence, these peaks form fingerprints, well known for a variety of more or less complex molecules. For 4-NTP, the most prominent peaks are around $1300\,\mathrm{cm}^{-1}$ as visible in the Stokes region of Figure 1.1. The vibrational peaks are also apparent in the anti-Stokes (AS) region if the sensitivity of the measurement is high enough. In addition, a broad background (BGND) is observed in most SERS spectra [1, 50]. The origin of this background is still under debate. While some scientists attribute the BGND to photoluminescence (PL) [7, 16, 69, 82], others relate it to electronic Raman scattering (ERS) [1, 26, 28, 49, 51, 75] or provide different theories [6, 36, 73] involving interaction with the adsorbed molecules. However, the background is commonly associated with the response of the nanoparticles and their electron distribution, as it can be observed even in the absence of any attached molecules [16, 49]. Since the optical properties of metals are influenced by the excitation wavelength, the SERS background is as well [16, 23, 87, 97]. This thesis discusses this dependence and

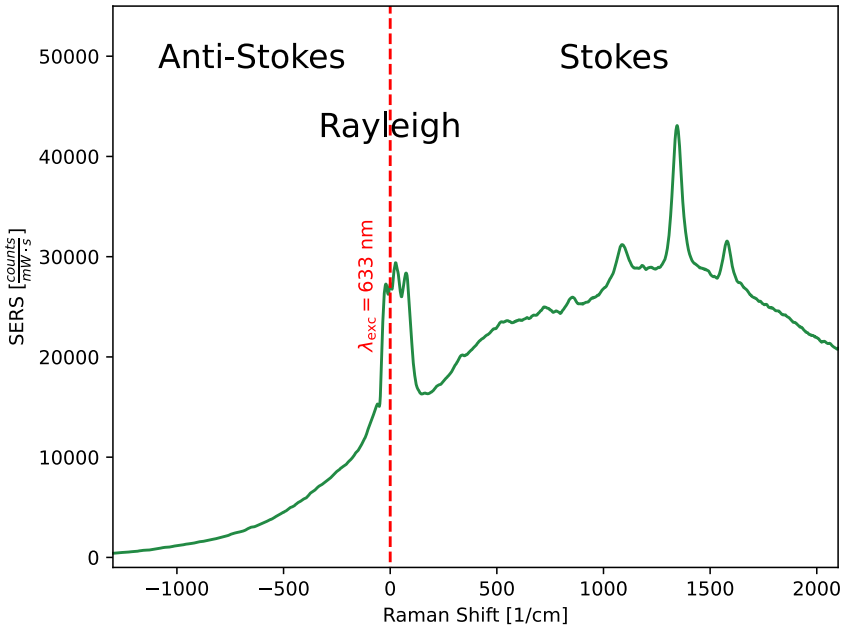

Figure 1.1: SERS spectrum of 4-Nitrothiophenol (4-NTP) coated on clustered Au nanoflowers. They show great signal enhancements in the optical range and were therefore excited at a wavelength of $\lambda_{exc} = 633\,nm$. Vibrational peaks of 4-NTP are observed in the Stokes region. These peaks are accompanied by a continuous background caused by the nanoparticles themselves which also extends into the anti-Stokes region. Despite the use of bandpass filters, a fraction of the Rayleigh scattered peak from the laser remains noticeable.

derives statements about the origin of the SERS background that suggest extending the existing theories by a significant contribution of interband transitions. The results of photoluminescence excitation spectroscopy supporting this are discussed in chapter 4.
Considering its origin and characteristics, knowledge about the nanoparticle response is crucial not only for enabling background-free SERS imaging. The SERS BGND is linked to the electron distribution in the nanoparticle. This connects the background to the photocatalytic activity of the system, as the enhancement of chemical reactions of adsorbed molecules relies on charge transfer from the nanoparticle [10, 11, 13, 59, 77, 101]. Also, fully understanding the nanoparticle response can provide insights into the mechanisms behind other plasmonic-enhanced phenomena such as photovoltaic [32, 38, 102] and magnetism [3, 22]. Hence, properties of the investigated systems can be derived from the SERS background. The Anti-Stokes BGND signal for instance can be used for non-invasive temperature measurements at the nanoscale [5, 15, 19, 49, 94, 95]. This thesis establishes a data processing method based on the calibrated thermometry of Xie and Cahill [95], which enables a comparison of different hot spots on inhomogeneous nanoparticle samples by eliminating the effects due to varying plasmonic enhancements, as discussed in chapter 5.
In addition, while investigating the SERS background of the gold nanoflowers, a decay

of the BGND on the timescale of a few minutes was observed that has not been reported yet. In chapter 6, the decay and its dependencies on several factors are analyzed, but its source can only be suspected and further investigations are proposed.
Preceding that, the next chapter covers fundamentals and existing literature on the origin of the SERS background and also explains Anti-Stokes Nanothermometry. Subsequently, chapter 3 describes the methods and samples used in the experiments of this thesis before delving into the discussion of the results as outlined above.

Chapter 2

Fundamentals and State of the Art

In the field of light-matter interactions, plasmonic materials have fascinated researchers for many decades. With their unique ability to amplify electromagnetic fields at the nanoscale, these materials have opened up new horizons for various applications, ranging from ultrasensitive sensing [24, 27, 31, 42, 60, 65, 66, 70, 92, 104, 106] to efficient light harvesting [47, 66, 102]. One prominent application is surface-enhanced Raman spectroscopy (SERS), a powerful analytical technique to achieve remarkable enhancements of Raman signals of molecules adsorbed to metal nanoparticles, enabled by their plasmonic properties [8, 43, 54, 67, 106]. Gold nanoparticles, in particular, are often favored for their ability to induce plasmonic resonance in the visible range. [85]. Therefore, they are the focus of this thesis.
This chapter covers the fundamentals of SERS and the response of metal nanoparticles to incident light. Moreover, preceding research in the literature on the origin and the properties of the background of SERS spectra is introduced.

2.1 Surface Enhanced Raman Spectroscopy

Raman spectroscopy uses inelastic scattering of photons by matter to investigate the composition of materials [74]. In most cases, molecules and their vibrational modes are observed, as depicted in Figure 2.1. In the scattering process, the incident photons are not resonant with electronic transitions of the molecule. Therefore, the excitation occurs via virtual levels [74]. Most scattering processes are Rayleigh scattering, where the final photon has the same energy as the initial photon. If, in contrast, excitation or relaxation of the vibrational modes occurs, the emitted photon is shifted to lower (Stokes) or higher energies (anti-Stokes), respectively. These inelastic processes are called Raman scattering and the corresponding Raman shifts are characteristic of the vibrational modes [74]. Hence, a discrete spectrum emerges, containing fingerprints of the investigated molecules, known for countless substances. For 4-Nitrothiophenol (4-NTP), they are illustrated in Figure 1.1 with the most prominent peaks around $1300\,\mathrm{cm}^{-1}$. Due to the low resolution of this specific recording, they are not visible in the anti-Stokes (AS) region.
Raman spectroscopy can be used to measure time-resolved, chemical reactions in situ since it is a non-destructive technique [106]. However, the strength of the Raman peaks

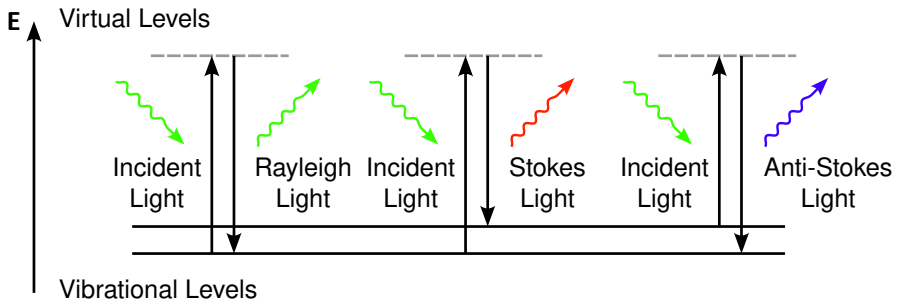

Figure 2.1: Vibrational scattering in molecules. Scattered light can have the same energy E as the incident light (Rayleigh) or be shifted (Raman) to the red due to excitation (Stokes) or to the blue due to relaxation (anti-Stokes) of vibrational modes.

is extremely low due to low scattering cross-sections [89, 99]. The optical cross-sections σ resemble the power P removed from an initial optical mode by a process like scattering or absorption. This power is normalized to the incident intensity I_i [105]. Hence, the optical cross-section of a single object is defined by Equation 2.1 [74, 105].

$$\sigma \equiv \frac{P}{I_i} \tag{2.1}$$

For example, in the case of resonance with an electronic state, the fluorescence cross-section is about six orders of magnitude larger than the Raman cross-section [89]. Therefore, either high concentrations of the molecules or laser intensities are required to measure meaningful Raman spectra [72]. This gladly changes in the vicinity of surfaces of plasmonic nanoparticles. Here, the incident light induces a collective oscillation of the free electrons. More precisely it excites localized surface-plasmon polaritons (LSPP) [104]. Suppose the excitation wavelength falls within the resonance of the LSPP, the localized surface plasmon resonance (LSPR), strong enhancements of the local electric field at the surface, absorption, and scattering are caused [2]. As the molecule is adsorbed to the nanoparticle surface, it is influenced by the local electric field. I. e., in the scattering process at the molecule, the incident light is plasmonic enhanced [76]. Since the energy shift due to Raman scattering is in general much smaller than the LSPR width, the scattered electric field is enhanced as well by the LSPP [74]. Consequently, the intensity of the scattered light $I_{\text{scatt}} = |\vec{E}_{\text{scatt}}|^2$ scales as the fourth power of the local electric field enhancement [61]. This ultimately results in much higher Raman cross-sections by up to fifteen orders of magnitude [60, 89, 92, 106]. The use of noble metal nanoparticles not only enables the detection of molecules via this so-called surface-enhanced Raman spectroscopy (SERS). Their inert nature and capability to adsorb molecules on their surface also provide chemical enhancement due to charge transfers onto the molecules [10, 11, 13, 47, 59, 76, 77, 101] and make metal nanoparticles great photocatalysts. SERS is therefore a powerful tool to measure chemical reactions as they happen [24, 63, 84] and even single-molecule Raman spectroscopy is possible with this technique [24, 60, 106]. In addition to the peaks corresponding to molecule vibrations, SERS spectra always show a more or less strong and broad background [20, 34, 50, 73]. This BGND can be attributed to a phenomenon caused by the nanoparticles themselves [16, 20, 49]. Especially, high-faceted nanoparticles like gold nanoflowers, which show a rather

strong background, also offer high photocatalytic activity [14, 68, 96]. Therefore a connection between both is likely. section 2.3 covers existing theories about the origin of this nanoparticle response. Before that, the next section explains basic principles of light-metal interactions.

2.2 Permittivitiy and Refractive Index

In general, the effect of light-matter-interaction can be described by the electric Polarization $\vec{P}$. In the linear approximation, this represents the creation of dipole moments due to an incident electric field. In the visible spectrum, this mostly happens due to the displacement of more or less mobile electrons in contrast to the rigid atom nuclei in solids [99]. The capability of matter to polarize due to an electric field $\vec{E}$ is given by the electronic polarizability α. Hence, polarizability and polarization are connected via the following equation [40]:

$$\vec{P} = \varepsilon_0 n_V \alpha \vec{E} \tag{2.2}$$

Where ε_0 is the vacuum permittivity and n_V is the particle density of independent atoms. In crystal structures, it has to be taken into account that the electric field at an atom site is influenced by the surrounding dipoles. Thus, the local electric field differs from the external electric field. For cubic crystals, like gold, this leads to a relation between the polarizability α and the relative permittivity or dielectric function ε called the Clausius-Mossotti equation [40]:

$$\frac{1}{3} n_V \alpha = \frac{\varepsilon - 1}{\varepsilon + 2} \tag{2.3}$$

Due to its connection to the electric polarization, the relative permittivity is a valuable optical parameter of the material that is also dependent on the frequency of the electric field. Since it is a complex parameter, it can be split into real part $\varepsilon_{\text{real}}$ and imaginary part $\varepsilon_{\text{imag}}$.

$$\varepsilon = \varepsilon_{\text{real}} + i\,\varepsilon_{\text{imag}} \tag{2.4}$$

While the real part indicates the phase difference between the driving electric field and the material's response, the imaginary part is a quantity of the field dissipation inside the material. The dielectric function can also be related to the complex index of refraction $\tilde{n}$ [30, 99].

$$\begin{aligned} \tilde{n} &= \sqrt{\varepsilon\mu} \\ &= n + i\kappa \end{aligned} \tag{2.5}$$

Here, μ is the relative permeability, n indicates the ratio of the vacuum speed of light to the phase velocity inside the medium, and κ is the extinction coefficient. For non-magnetic materials, μ is equal to one. Hence, the real and imaginary parts of the dielectric function can be written as:

$$\varepsilon_{\text{real}} = n^2 - \kappa^2 \tag{2.6}$$

$$\varepsilon_{\text{imag}} = 2n\kappa \tag{2.7}$$

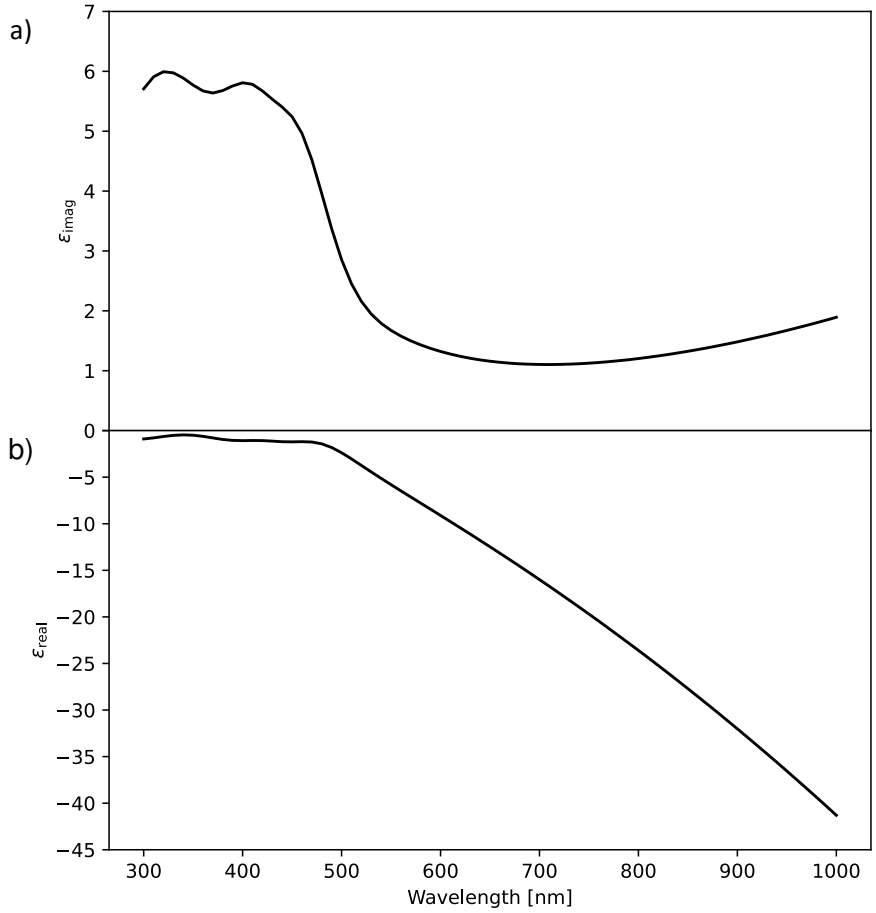

Figure 2.2: Dielectric function of gold in the visible range separated into a) imaginary part $\varepsilon_{\text{imag}}$ and b) real part $\varepsilon_{\text{real}}$. The data is provided by Olmon et al. [78] for single crystal gold.

Since the optical constants n and κ are determined through reflectivity and transmission measurements or ellipsometry [78], they are often used to calculate the dielectric function of materials [30]. Imaginary and real parts of both dielectric function and refractive index are depicted for gold in Figure 2.2 and Figure 2.3, respectively.
Generally, the electronic part of the permittivity for solids can be distinguished into two processes that rely on the electronic band structure of the material. The band structure of gold is illustrated in Figure 2.4. Interband processes result from the excitation of electrons between two bands. In gold, prominent excitations due to the absorption of photons in the visible range occur from occupied states of the $5d$-band into free states of the $6sp$-band. These are shown around the symmetry points X and L in the zoom panels of Figure 2.4. Optical transitions can also occur between different conduction bands at the L-point [85]. On the other hand, in metals, the Fermi level E_F always lies inside an electronic band, which enables intraband processes of free electrons. These also contribute to the dielectric function. For metals, intraband processes are well described

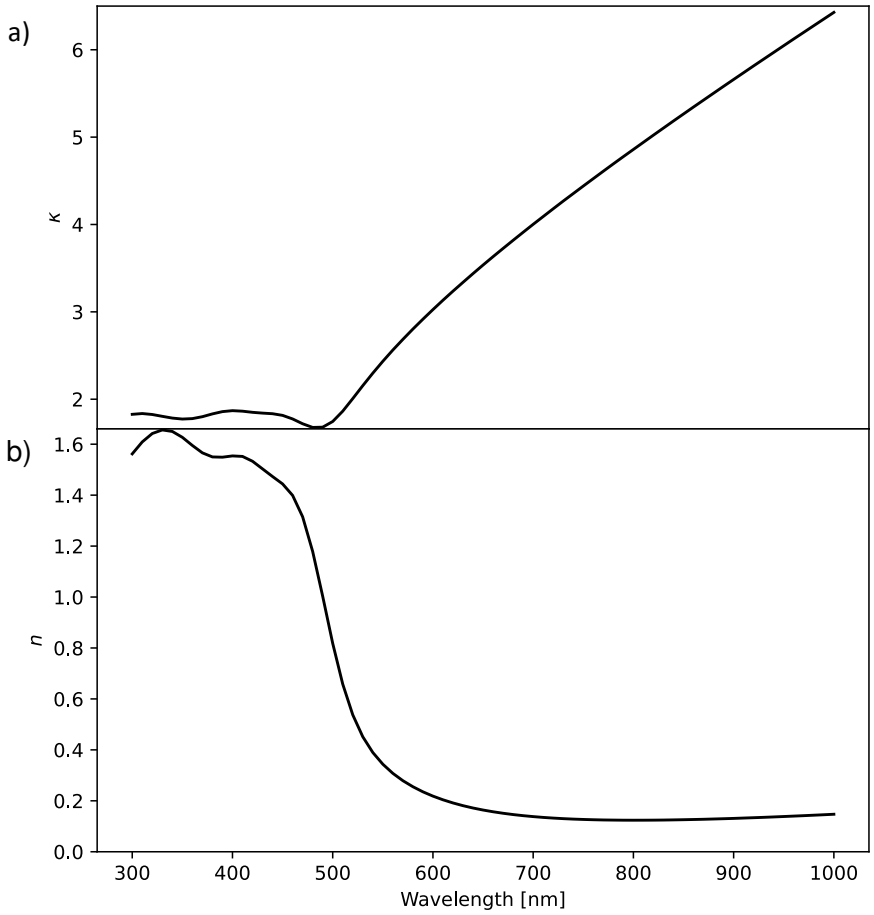

Figure 2.3: Refractive index of gold in the visible range separated into a) imaginary part κ and b) real part n. The data is provided by Olmon et al. [78] for single crystal gold.

with the classical Drude theory of a free electron gas. Therefore, the dielectric function can also be separated into an intraband $\varepsilon_{\text{Drude}}$ and an interband ε_{IB} part [9, 30, 76]:

$$\varepsilon(\omega) = \varepsilon_{\text{Drude}}(\omega) + \varepsilon_{\text{IB}}(\omega) \tag{2.8}$$

$$\varepsilon_{\text{Drude}}(\omega) = 1 - \frac{\omega_p^2}{\omega\,(\omega + \gamma)} \tag{2.9}$$

$\varepsilon_{\text{Drude}}$ is determined by the plasma frequency ω_p, which is the frequency at which $\varepsilon_{\text{real}}$ changes sign [30], and the collision frequency γ of the electron gas. In bulk metals, collisions of electrons can occur with other electrons, phonons, and defects in the material [12]. As the metal shrinks in size, which is the case for nanoparticles, collisions with the surface become more frequent. Thus the contribution of electron-surface scattering to γ can not be neglected [9, 12]. These collisions facilitate the transitions of wavevectors that are essential for electronic intraband excitations forming the foundation for the nanoparticle response in SERS spectra, discussed in the next section.

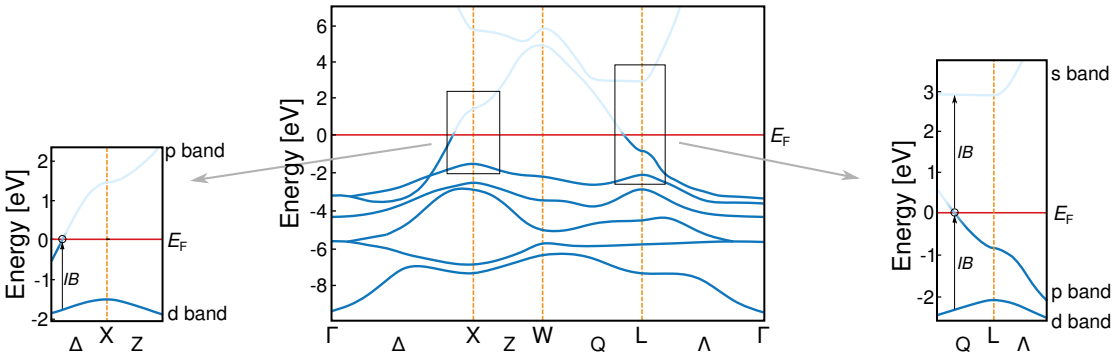

Figure 2.4: Electronic band structure of gold as published by Stete [85]. In the ground state, occupied electronic states (darker blue) are separated from the empty states (lighter blue) by the Fermi level E_F (red line). The panels on the left and right zoom into the regions around the symmetry points X and L, respectively. Interband transitions IB in the visible range exist from the $5d$-band into the $6sp$-band around the X and L-point. At the L-point, they can also occur between different conduction bands marked as p-band and s-band.

2.3 Nanoparticle Response

There are various explanations for the SERS background in the literature. Some researchers link the BGND to photoluminescence (PL) [7, 16, 69, 82], whereas others associate it with electronic Raman scattering (ERS) [1, 26, 28, 49, 51, 75], or propose alternative theories that fall outside the scope of this thesis [6, 36, 73]. Yet, there is a substantial consensus that the background originates from the plasmonic nanoparticles themselves, as it can be observed without any molecules adsorbed [16, 49]. LSPPs are crucial in both, PL and ERS, as they facilitate significant electromagnetic field enhancements and selective absorption and scattering governed by the LSPR [2]. In other words, the LSPR influences the probability distribution of excited electrons dependent on the wavelength of the incident light. On the contrary, the emission is determined by the photonic density of states (PDOS). The PDOS describes the number of photonic states that are available for emission averaged over the whole nanoparticle [17]. As these emission channels are also enhanced by the plasmons, the PDOS is also determined by the LSPR [17, 23]. Regardless of whether PL or ERS is considered, the nanoparticle response signal resembles its LSPR [16, 33, 49]. The LSPR itself relies on the electronic properties of the metal like the band structure and thus the permittivity. Also, the size and shape of the nanoparticle structures, as well as the environment, are crucial for the LSPR's characteristic [88, 92]. The extinction spectrum for a batch of gold nanorods resembling their LSPR is presented in Figure 2.5. The calculated spectrum of a single nanorod, depicted in red, exhibits notable narrowing. The broadening in the ensemble measurement is caused by inhomogeneities between the different nanoparticles due to the production process [104]. This underlines the importance of their physical shape on their optical properties. More complex nanoparticles, e. g. with many facets, can therefore cause even broader LSPR [96]. Moreover, clusters of nanoparticles amplify these effects as the area between the particles can create even stronger enhancements, which

can also change the spectrum [37, 39, 65, 76, 90].
In Figure 2.6, both intraband PL and ERS are shown for gold. As a photon is absorbed

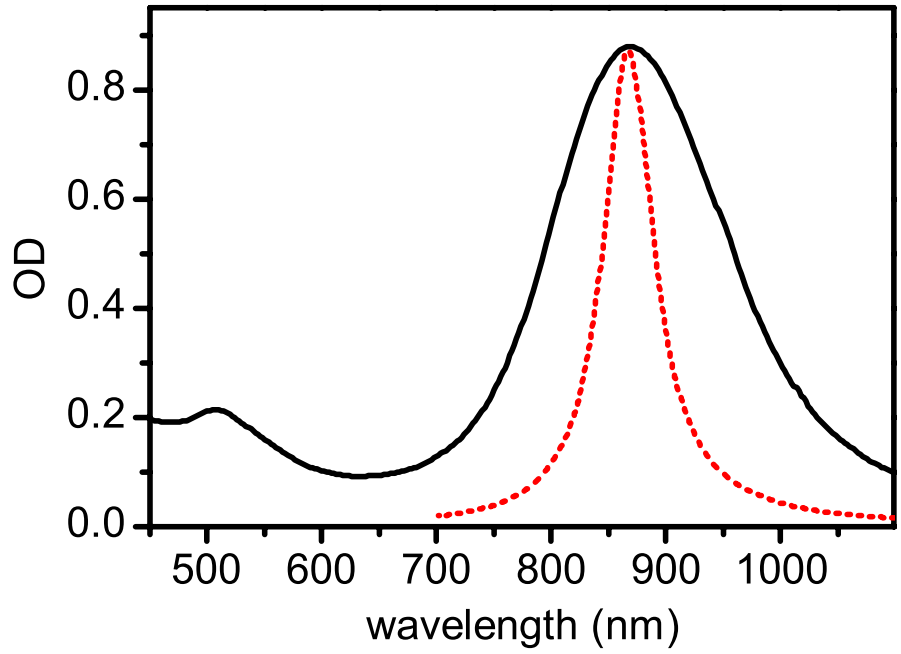

Figure 2.5: Extinction spectrum of Au nanorods in solution (black solid) and calculation of the spectrum of a single spheroid in water (red dotted) as provided by Zijlstra and Orrit [104]. The measurement exhibits a broader spectrum due to inhomogeneities in the production process of the nanoparticles.

by the nanoparticle, an electron from a state below the Fermi level E_F is excited. In the case of photoluminescence, as depicted in Figure 2.6a), the electron requires a wavevector transition to be able to populate a real state above the Fermi level. This transition is most likely provided by the scattering of the electron with the surface of the nanoparticle. Due to the confinement length Δx, wavevector transitions of $\Delta k \approx (\pi/\Delta x)$ are available [49]. On the other hand, in electronic Raman scattering, the energized electron occupies a virtual state, and therefore no additional wavevector is required in the initial process. This is shown in Figure 2.6b). Ultimately, in both theories, the excited electrons recombine under another wavevector transition with an empty state in the band structure. If the final state's energy is above the energetic level of the initial state, as illustrated, a Stokes-shifted photon will be emitted. These nanoparticle emissions are often considered to be intraband processes, as they are also observable with excitation wavelengths above the limit of interband transitions [16, 49]. Nevertheless, interband processes can greatly enhance the efficiency of nanoparticle emissions [16, 97]. Cai et al. [16] explain this with interband excitations followed by Auger-like relaxations driving intraband excitation.
As mentioned, both PL and ERS attribute their broad spectrum to the LSPR of single or multiple nanoparticles. This thesis does not distinguish between the processes. This would require experiments on ultrashort timescales since virtual states recombine much faster than real states [75]. Hence, for the sake of simplification, photoluminescence is

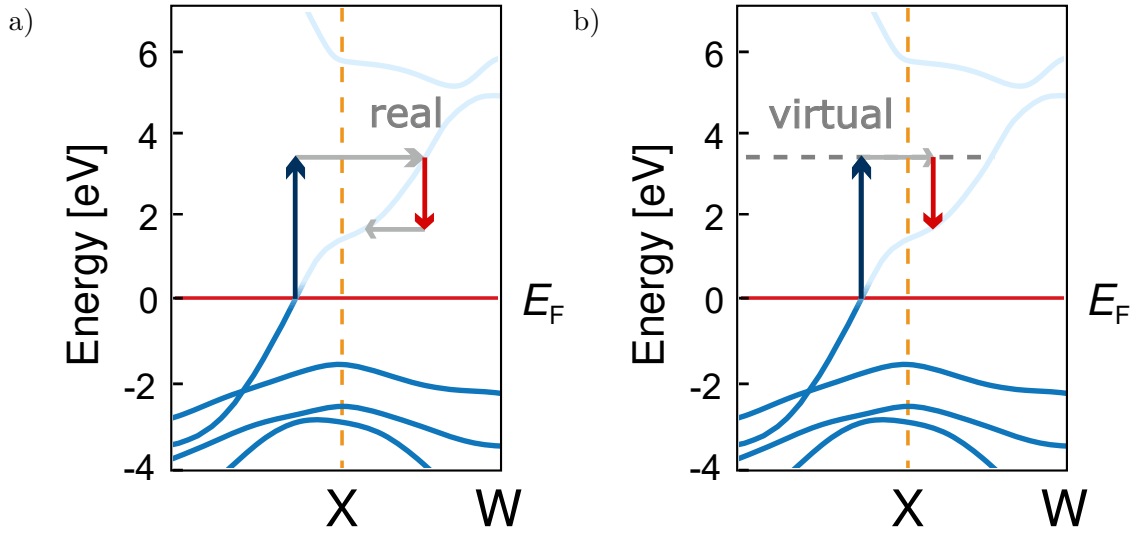

Figure 2.6: Band structure of gold, modified from Stete [85], with schematic illustrations of intraband Stokes a) photoluminescence (PL) and b) electronic Raman scattering (ERS) in nanoparticles. Vertical arrows represent the incident (blue) and emitted (red) photons, respectively. Horizontal arrows represent the wavevector transitions due to the scattering of the electrons with the surface of the nanoparticles. While in PL the electrons populate real states after the absorption process, the intermediate states in ERS are virtual.

considered the source of the nanoparticle response in all subsequent figures and arguments. Thus, real states in the band structure of gold will represent the intermediate states in this thesis. The discussed mechanisms also apply to electronic Raman scattering, if not stated otherwise.

In addition to the so far addressed Stokes shifted background, there is also an anti-Stokes (AS) component. This can be viewed in Figure 1.1 on the left side of the Rayleigh peak. While those emissions also originate from excited electrons in the metal, they are up-converted with respect to the incident photons [15]. The underlying PL mechanism is outlined in Figure 2.7. Only occupied states can be excited. At absolute zero (0 K), each state below the Fermi level E_F is occupied in the ground state. Consequently, after an excitation with a single photon, there is no hole below the initial state to recombine with and no AS emission is possible. At finite temperatures, the occupation probability around the Fermi level changes, dictated by the Fermi-Dirac distribution, as shown in Figure 2.7. Now, there is a small number of higher initial states and lower empty states allowing anti-Stokes processes. Accordingly, the distribution of hot electrons and empty states is far more important in the AS region than the LSPR and PDOS enhancement, respectively. Hence, the shape of the emission is defined by the occupation distribution of the electrons in their bands. The maximum possible energy shift is higher, the higher the temperature is [15]. This explains the exponential decrease of the response signal towards higher AS shifts in comparison to the flatter trend on the Stokes side, as indicated by Figure 1.1.

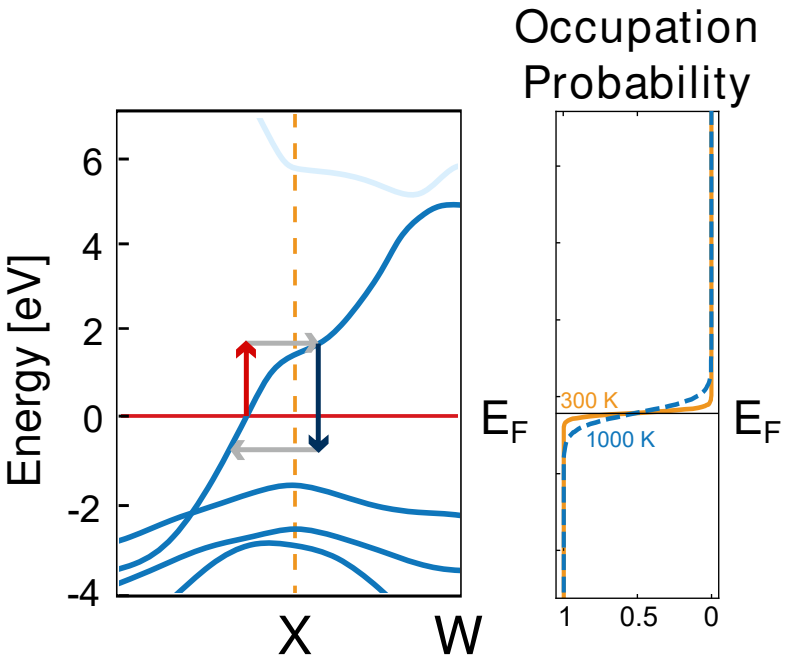

Figure 2.7: left: Band structure of gold, modified from Stete [85], with schematic illustrations of intraband anti-Stokes photoluminescence (PL) in nanoparticles. Vertical arrows represent the incident (red) and emitted (blue) photons, respectively. Horizontal arrows represent the transfer of wavevectors. right: occupation probability of electronic states around the Fermi level E_F for 300 K (solid orange) and 1000 K (dashed blue).

2.4 Anti-Stokes Thermometry on Metal Nanoparticles

Given that the anti-Stokes signal necessitates the presence of free electronic states below the Fermi level (or occupied states above), which is typically enabled by finite temperatures, it is reasonable to consider that the plasmonic nanoparticle's AS response could hold valuable information about the temperature of itself [5, 15, 19, 49, 56, 94, 95]. I.e., changes in temperature shape the AS signals decisively. More precisely, the slope of the anti-Stokes signal is altered with the temperature, which is clearly evident in Figure 2.8. The background displays linearity on a logarithmic scale and its slope decreases with rising temperatures. Notably, the AS temperature is not to be confused with the temperature determined by the ratio of anti-Stokes to Stokes signal of molecular Raman peaks [11, 60]. While the latter describes the temperature of adsorbed molecules due to their active vibrational modes, the AS background describes the temperature of the nanoparticles themselves. This temperature can be determined not only qualitatively but also quantitatively. Multiple approaches using the anti-Stokes spectra of SERS measurements as nanoscale thermometers are presented in the literature [5, 15, 19, 49, 94, 95]. To achieve this, the anti-Stokes signal I_{AS} of surface-enhanced Raman measurements has to be described as a function of Raman shift $\tilde{\nu}_{\mathrm{R}}$ and temperature T [19, 48]:

$$I_{\mathrm{AS}}\left(\tilde{\nu}_{\mathrm{R}}, T\right) = \gamma_{\mathrm{Setup}}\left(\tilde{\nu}_{\mathrm{R}}\right) I_{\mathrm{LSPR}}\left(\tilde{\nu}_{\mathrm{R}}\right) \tilde{n}\left(\tilde{\nu}_{\mathrm{R}}, T\right) \tag{2.10}$$

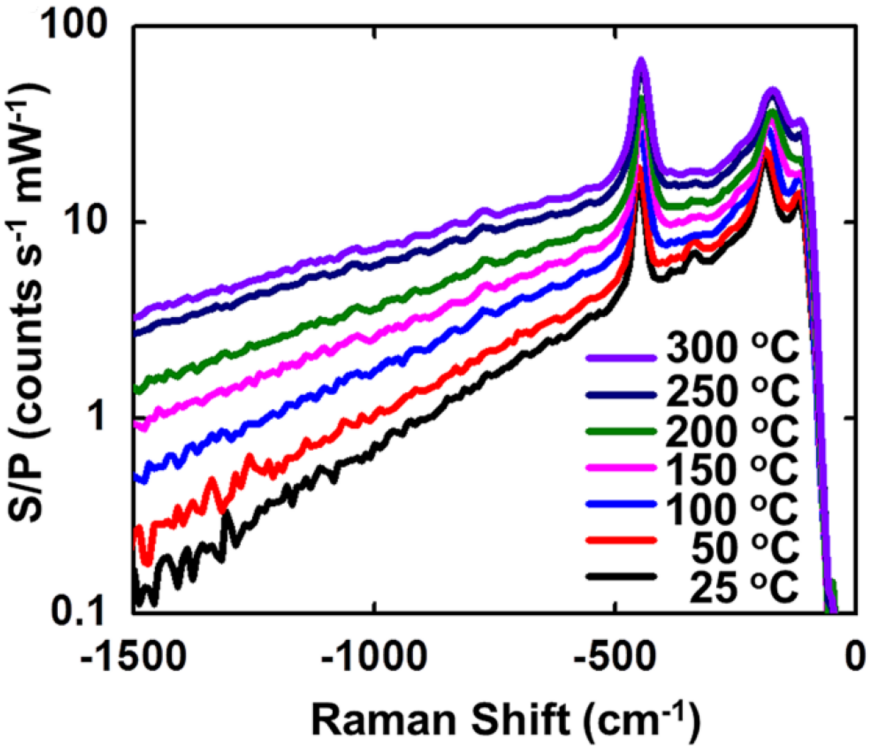

Figure 2.8: Anti-Stokes nanoparticle response collected from arrays of nanodisks as a function of substrate temperature by Xie and Cahill [95]. The logarithmic illustration clarifies the change of the slope of the signal with temperature.

$$\gamma_{\text{Setup}}\left(\tilde{\nu}_{\text{R}}\right) = \alpha\left(\tilde{\nu}_{\text{R}}\right) t_{\text{exposure}} \tag{2.11}$$

$$I_{\text{LSPR}}\left(\tilde{\nu}_{\text{R}}\right) = \sigma_{\text{NP}}\left(\tilde{\nu}_{\text{R}}, T\right) g_e^2\left(\tilde{\nu}_{\text{R}}, T\right) g_i^2\left(\tilde{\nu}_{\text{R}}, T\right) I_i\left(\tilde{\nu}_{\text{R}}\right) \tag{2.12}$$

Here, γ_{Setup} describes the effects of the setup on the measurement given by the exposure time t_{exposure} as well as losses due to the setup and the detector function combined in α. I_{LSPR} is the plasmonic enhanced laser intensity, which consists of the optical cross-section of the nanoparticle σ_{NP}, the plasmonic enhancement factors g_i^2 and g_e^2 of the incident and emitted light, respectively, and the incident laser intensity I_i. The temperature dependence of I_{AS} is based solely on the distribution function $\tilde{n}$, which determines the occupation of the electronic states [19, 95]. There is an ongoing discussion in the literature on which distribution is to be used. Some state that the hot-electron temperature is measured since electrons cause the nanoparticle response and therefore Fermi-Dirac should be used (Equation 2.13) [5, 15, 45]. Others claim it is a measurement of the metal lattice temperature due to dominating electron-phonon scattering, which requires using the Bose-Einstein distribution (Equation 2.14) [19, 48, 95]. Both can be approximated by the Boltzmann distribution (Equation 2.15), as the differences become negligible within the available Raman shift region in most measurements [5, 15, 45, 49, 56, 86]. The equations 2.13-2.15 show all three distributions, utilizing the Boltzmann constant k_B, the Planck constant h, and the vacuum speed of light c. Figure 2.9 depicts

the vanishing deviations for absolute values of Raman shifts above $500\,\mathrm{cm}^{-1}$.

$$\tilde{n}_{\mathrm{FD}} = \left[\exp\left(-\frac{hc\tilde{v}_R}{k_b T}\right) - 1\right]^{-1} \tag{2.13}$$

$$\tilde{n}_{\mathrm{BE}} = \left[\exp\left(-\frac{hc\tilde{v}_R}{k_b T}\right) + 1\right]^{-1} \tag{2.14}$$

$$\tilde{n}_{\mathrm{Boltz}} = \left[\exp\left(-\frac{hc\tilde{v}_R}{k_b T}\right)\right]^{-1} \tag{2.15}$$

Moreover, according to Cai et al. [15], low laser intensities lead to these differences vanishing due to the large photon spacing, giving the excited hot electrons enough time on average to equilibrate their temperature with the metal lattice. However, at high laser intensities, a second exponential component emerges in the signal at high Raman shifts due to the contribution of a subpopulation of extreme hot carriers [86, 94].

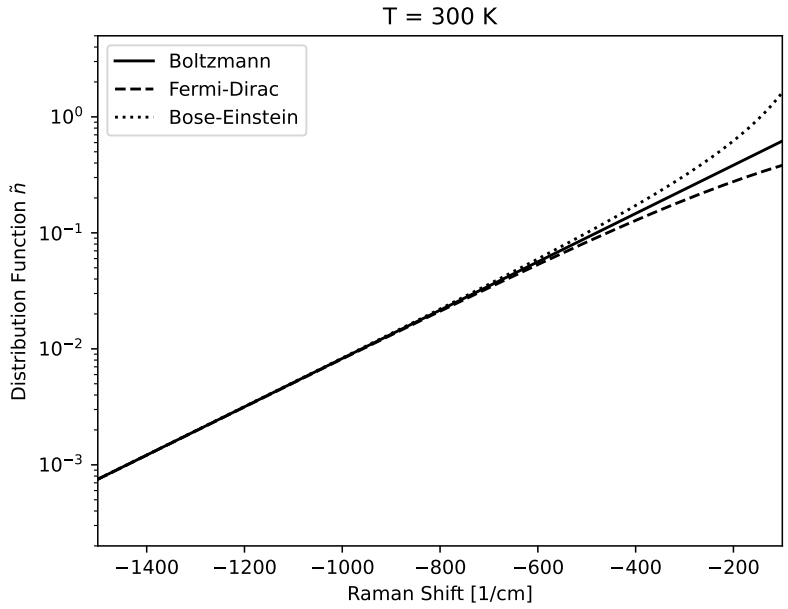

Figure 2.9: Boltzmann, Fermi-Dirac, and Bose-Einstein distributions, as indicated by the legend, for negative Raman shifts at $T = 300\,\mathrm{K}$ following Equation 2.13-2.15.

To determine the absolute temperature from the measured anti-Stokes signal I_{AS}, γ_{Setup} and I_{LSPR} must be known. While γ_{Setup} requires precise knowledge of the setup, for I_{LSPR} the properties of the nanoparticles have to be determined. Carattino, Caldarola, and Orrit [19] assumed the surface plasmon resonance to follow Equation 2.16, a Lorentzian function.

$$I_{\mathrm{LSPR}}(\tilde{v}_R) = \frac{(\Gamma/2)^2}{(\nu_L - c\,\tilde{v}_R - \nu_{\mathrm{LSPR}})^2 + (\Gamma/2)^2} \tag{2.16}$$

Here, ν_L is the laser frequency, ν_{LSPR} is the resonance frequency of the surface plasmon, and Γ is the width of the resonance. This is a valid approach for gold nanorods. For more

complex systems like nanoparticle clusters, the LSPR is not that simple to describe, as hot spots can create strong LSPR [37, 39, 65, 76, 90] with multiple peaks [65].
Fortunately, it is possible to eliminate γ_{Setup} and I_{LSPR} via a calibration process introduced by Xie and Cahill [95]. To remove γ_{Setup} and I_{LSPR}, it is sufficient to run a baseline measurement at a known temperature T_0, measured at the same set of nanoparticles. When dividing both signals by each other, only the temperature-dependent distribution functions $\tilde{n}$ remain.

$$\frac{I_{\mathrm{Signal}}\left(\widetilde{\nu}_{\mathrm{R}}, T_{\mathrm{NP}}\right)}{I_{\mathrm{Signal}}\left(\widetilde{\nu}_{\mathrm{R}}, T_0\right)} = \frac{\tilde{n}\left(\widetilde{\nu}_{\mathrm{R}}, T_{\mathrm{NP}}\right)}{\tilde{n}\left(\widetilde{\nu}_{\mathrm{R}}, T_0\right)} \tag{2.17}$$

In the resulting Equation 2.17, T_{NP} is the only unknown parameter, provided that T_0 is known. Hence, the distribution function $\tilde{n}\left(\widetilde{\nu}_{\mathrm{R}}, T_{\mathrm{NP}}\right)$ can be determined and the absolute temperature of the nanoparticles T_{NP} can be extracted from it. However, measuring the temperature of the close environment of the sample with conventional thermometers will not accurately reflect the temperature at the irradiated spot. Plasmonic heating of the nanoparticles due to absorption of light will always elevate the temperature [53]. Therefore, an iteration process is needed. For this, multiple SERS spectra are acquired at different laser powers. Now the temperature for every single power can be calculated with the lowest power measurement as the baseline. This is done under the assumption that T_0 matches the temperature of the environment, often room temperature. This corresponds to *iteration 0* in Figure 5.2 in section 5.1, where this calibration process is shown for the gold nanoflowers used in this thesis. The measured temperature is proportional to the laser power [53, 95]. Hence, a linear function extrapolates the temperature of the nanoflowers T_{Au} to a power of $P = 0\,\mathrm{W}$. In the next step, T_0 is shifted so that $T_{\mathrm{Au}}\left(P = 0\right)$ is equal to the environmental temperature. Afterward, all temperatures are calculated again with Equation 2.17. This process continues until $T_{\mathrm{Au}}\left(P = 0\right)$ is in a certain margin around the environment. With this calibration process done, the difference in temperature caused by laser heating can be considered for upcoming measurements and it is possible to determine the absolute values of the nanoparticle temperature. With this method, the temperature can be controlled in plasmonic-driven photoreactions observed via surface-enhanced Raman spectroscopy.
In the subsequent thesis, this approach will be employed to assess the capability of clustered gold nanoflowers as absolute nanothermometers. Prior to that, the Stokes response of the same nanoflowers will be examined, depending on the wavelength of the exciting light in the visible range. This investigation will offer insights into the origin of the nanoparticle response spectra and provide information about the role of interband transitions in photoluminescence or electronic Raman scattering, respectively.

Chapter 3

Experimental

3.1 Gold Nanoflowers

For analysis of the origin of the nanoparticle response, the goal is to create samples with high SERS background. As stated earlier, this can be achieved with clustered, high-faceted nanoparticles. Thus, an already available nanoflower sample coated with 4-NTP was used for most measurements. It was prepared following the procedure described by Sarhan et al. [83]. A microscopic image of this sample is illustrated in Figure 3.1, showing the strong clustering. Moreover, a transmission electron microscopy (TEM) image of

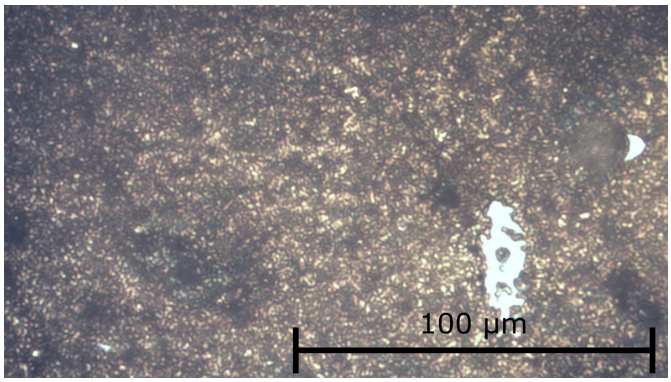

Figure 3.1: Optical image of the Au nanoflowers on silicon that were used for SERS and photoluminescence

typical gold nanoflowers is represented in Figure 3.2 with an extinction spectrum in the inset as published by Sarhan et al. [83]. This extinction spectrum shows the LSPR peak around 550 nm and the increase of the extinction to lower wavelength due to interband transmissions. Since the nanoflowers of the sample used in the here presented experiments are applied to a silicon substrate, no absorption and scattering spectroscopy in the visible range is possible. Therefore, another sample with equal nanoflowers was created on glass that was not coated with any additional molecules.

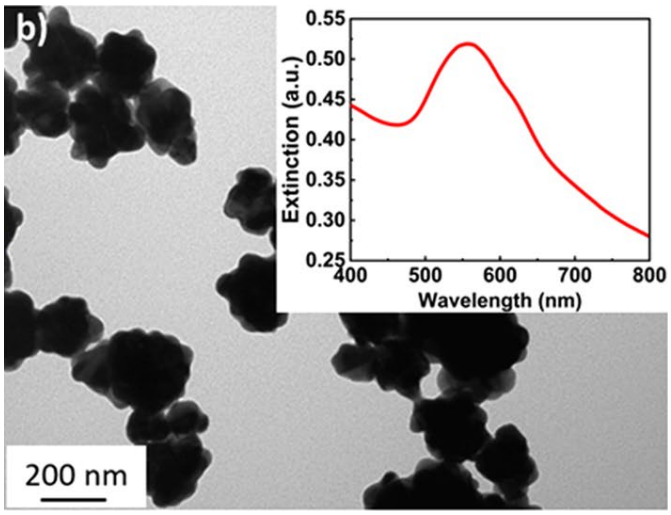

Figure 3.2: TEM image of gold nanoflowers as published by Sarhan et al. [83]. They are similar to those used in the experiments conducted here. The inset shows an extinction spectrum of the gold nanoflowers.

3.2 SERS & Photoluminescence Setup

To accomplish SERS and nanoparticle response measurements, a custom-built Raman microscope was enhanced with a supercontinuum white light source. The experimental setup is illustrated in Figure 3.3. For SERS measurements, the sample is exposed to $\lambda_{\text{exc}} = 633\,\text{nm}$ light from an *Ondax* diode laser system. This laser light is coupled into the setup using the reflection of volume Bragg grating 1 and focused onto the sample using an objective lens. Due to the clustered structures on the nanoflower samples, multiple nanoflowers are still illuminated simultaneously. Subsequently, the Rayleigh portion is filtered out from the scattered light using all three Bragg gratings 1-3, before the SERS signal is gathered in an *Andor Kymera 328i* spectrometer, paired with an *Andor Newton DU970P* vis-optimized CCD. This configuration allows simultaneous recording of Stokes and Anti-Stokes regions, as for example shown in Figure 1.1
The nanoparticle response spectra were measured in the same microscope. This technique is most often called photoluminescence (PL) measurement in the following, despite the fact that electronic Raman scattering can not be excluded. Therefore, an *NKT SuperK FIU-15* supercontinuum light source was integrated into the setup together with a *NKT SuperK VARIA* tunable filter. The combination of both can achieve coherent light from 400 nm to 840 nm with a minimum bandwidth of 10 nm. The still present infrared part of this incident light was filtered with a 750 nm shortpass filter *SP*. Due to the wide range of wavelengths, this light is introduced into the setup with the aid of a broadband pellicle beamsplitter (*Thorlabs BP-108*) to minimize the shift of the beam. Unfortunately, this beamsplitter modifies the spectral characteristics of both transmitted and reflected light. To eliminate the modulation from the photoluminescence signals, they were corrected using transmission spectra of the beamsplitter. One example of such reference spectra is depicted in Figure 3.4.

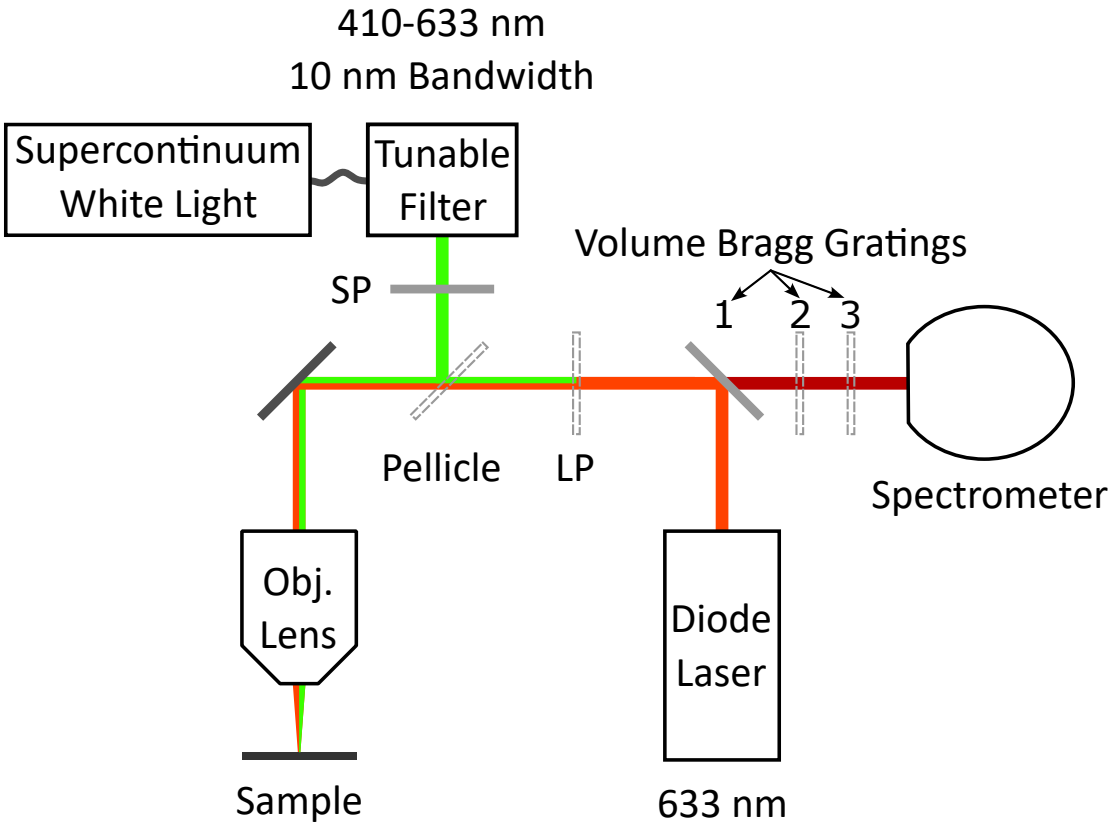

Figure 3.3: Microscope setup used for SERS and photoluminescence imaging. The objective lens focuses light onto the sample. Stokes and anti-Stokes SERS spectra of the sample are recorded with a diode laser (λexc = 633 nm) and the spectrometer. Volume Bragg grating 1 couples the laser into the optical path of the microscope, while all gratings 1-3 remove the Rayleigh peak from the signal. PL spectra are measured with 10 nm broad, visible light spanning from 410 nm to 633 nm, created by a combination of supercontinuum white light source and tunable filter. A pellicle beamsplitter introduces the beam into the microscope path. The 750 nm shortpass filter SP removes the IR part of the incident light, while different longpass filters LP (425 nm, 540 nm, 650 nm) are used to eliminate the laser from the PL signal. The pellicle beamsplitter, LP filters, and Bragg gratings 2 and 3 are easily removable to reduce their influence on the measurements when not needed.

To erase the elastic peak of the supercontinuum laser from the PL signal, different longpass filters LP with edges at 425 nm, 540 nm, and 650 nm were used, respectively. PL spectra for comparison of the filters are depicted in the next chapter in Figure 4.1. Also, this figure shows PL measurements, where the supercontinuum laser was replaced by a $\lambda_{\text{exc}} = 355$ nm UV-laser. The filtered light of the supercontinuum decreases in power at high photon energies. Consequently, a range spanning between 410 nm and 633 nm was selected for analysis. The pellicle beamsplitter and LP filters, as well as the volume Bragg gratings 2 and 3, are removable to reduce the influence of both measurement methods on each other. Bragg grating 1 is fixed in place, causing a dip at 633 nm observable in all photoluminescence spectra.

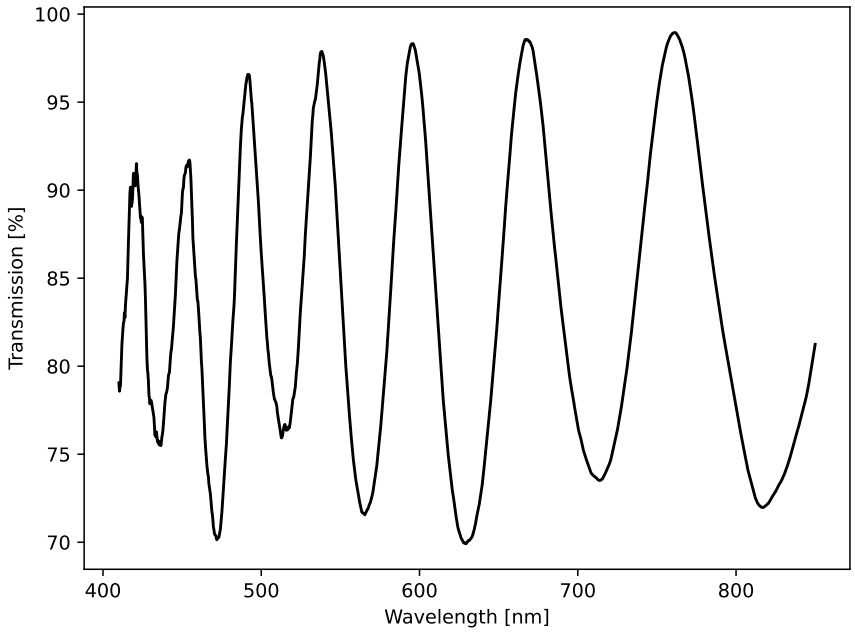

Figure 3.4: Transmission spectrum of the pellicle beamsplitter (*Thorlabs BP-108*).

3.3 Absorption & Scattering Spectroscopy

Absorption and Scattering measurements of the Nanoflower sample on glass were conducted using a *Agilent Cary 5000* UV-Vis-NIR Spectrophotometer and an integrating sphere following the method provided by Stete [85]. They consist of two measurements each, as depicted in Figure 3.5. The integrating sphere enables the detection of all light that is reflected by its wall. Hence, all forward scattered light I_{FS} (upper left) and all backwards scattered light I_{BS} (lower left) can be collected and summed up to the scattering spectrum I_{Scatt} after correction with the incident light I_0.

$$I_{\mathrm{Scatt}} = \frac{I_{\mathrm{FS}} + I_{\mathrm{BS}}}{I_0} \tag{3.1}$$

For the absorption measurement, on the other hand, the scattered light is recorded in addition to the transmission I_{T} (upper right) of the sample and its specular reflection I_{R} (lower right), respectively. The absorption I_{Abs} can be calculated afterward via Equation 3.2.

$$I_{\mathrm{Abs}} = 1 - \frac{I_{\mathrm{T}} + I_{\mathrm{FS}} + I_{\mathrm{R}} + I_{\mathrm{BS}}}{I_0} \tag{3.2}$$

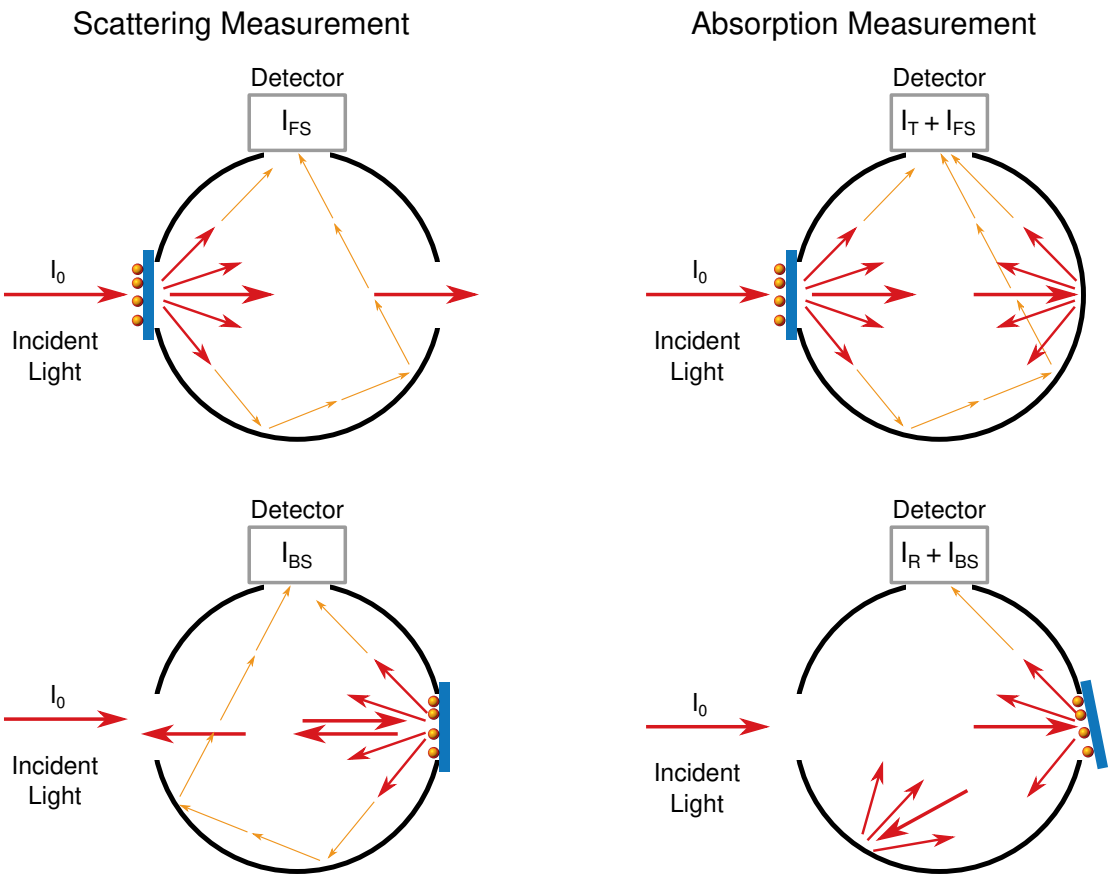

Figure 3.5: Schematic scattering (left) and absorption (right) spectroscopy of nanoparticles on glass substrates provided by Stete [85]. Both measurements use an integrating sphere to detect all forward scattered I_{FS}, backward scattered I_{BS}, transmitted I_{T}, and reflected I_{R} light. The different arrangements of the sphere and the sample accomplish the calculation of absorption and scattering spectrum with the aid of Equation 3.1 and 3.2

Chapter 4

Origin of the SERS Background

The SERS background (BGND) originates from electronic transitions inside of the Nanoparticles as described in section 2.3. Thus, investigating the processes contributing to the background is crucial for all interactions of light and nanoparticles, making it a fundamental aspect for the progress of applications like biochemical sensing, photovoltaics, or photocatalysis. For example, nanoparticles with strong SERS background signals, like gold nanoflowers, show strong photocatalytic activity as well [14, 68, 96]. Hence, a connection between both is likely.
An essential part of the characterization of the nanoparticle response is the contribution of interband and intraband transitions to the signal. Therefore, the dependence of the gold nanoflower BGND on different wavelengths of the incident laser light was investigated. In Figure 4.1, response spectra of the same hot-spot with all used longpass filters are shown for 355 nm (purple) and 410 nm (blue) excitation, respectively. They are in good agreement with each other. Thus, it is concluded that data from all filters can be compared. The nanoflower response shows a main peak around 560 nm with additional peak-like structures on both sides. Comparing the signal to the extinction spectrum in Figure 3.2 reveals similarities for wavelength above 500 nm. The nanoparticle response does not show the interband portion below 500 nm. This difference can be explained by the fact that the extinction spectrum is a loss spectrum, whereas photoluminescence (or ERS) provides an emission spectrum. Also, this difference aligns with the literature stating that the PL signal resembles the LSPR of the investigated nanoparticles [16, 33, 49]. The additional peaks in the response signal of the nanoflower sample are likely caused by its inhomogeneous, clustered nature, as multiple nanoflowers are irradiated simultaneously. A comparison between the SERS spectrum of the sample excited at 633 nm and its response to light with center wavelengths of 520 nm and 633 nm, respectively, is shown in Figure 4.2. In contrast to the small bandwidth Raman-laser, the filtered supercontinuum light has a bandwidth of 10 nm. Consequently, the molecule vibration peaks are blurred into the nanoparticle response in the PL recordings. All graphs are normalized to their respective mean value in the range from 730 nm to 850 nm. All spectra exhibit similar backgrounds above 750 nm, particularly both spectra excited at 633 nm. In the range from 633 nm to 700 nm, the SERS background and nanoflower response deviate, as the SERS signal decreases with decreasing wavelength. The SERS spectrum exhibits a noticeable red shift in the maximum of the Stokes BGND relative to

the Rayleigh peak, a phenomenon observed in multiple experiments documented in the literature [79, 86, 94]. This can be explained by the fact that the Joint density of states (JDOS) of the electron-hole pairs involved in the emission has a maximum at higher wavelengths than the Rayleigh peak [79, 94]. The high bandwidth of the supercontinuum light as well as the proximity to the filter for $\lambda_{exc} = 633\,nm$ and the large distance to the laser peak for $\lambda_{exc} = 520\,nm$ prevent this observation in the photoluminescence signal. Together with Figure 4.1, this confirms that the overall shape of the nanoparticle response strongly depends on the LSPR. Additionally, Figure 4.3 depicts the response

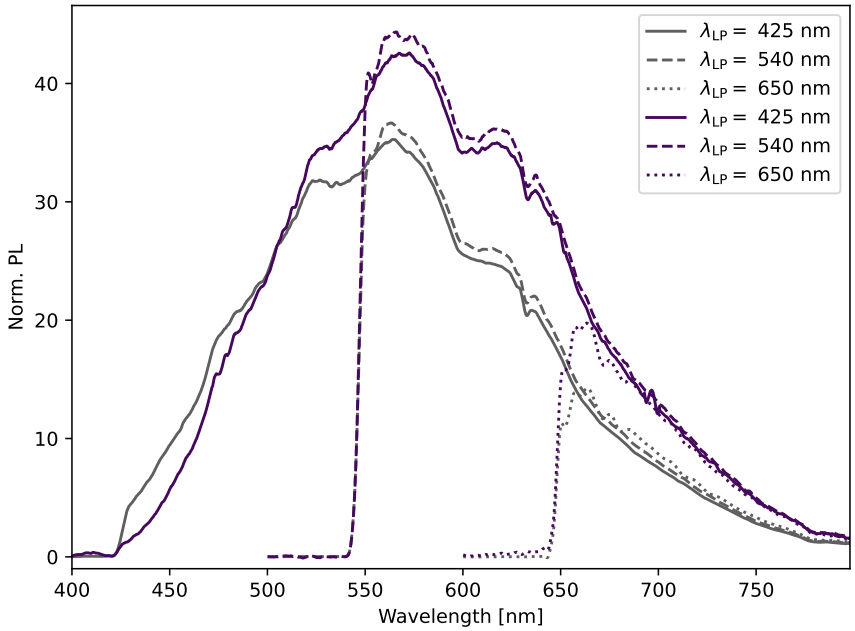

Figure 4.1: Response spectra of Au nanoflowers excited at 355 nm (grey) and 410 nm (purple). Different longpass filters with edges at 425 nm, 540 nm, and 650 nm, as indicated by the legend, were used to block the Rayleigh scattered and reflected light in front of the spectrometer. The signals are normalized with a fixed factor for each excitation wavelength to clearly demonstrate the blue and purple graphs. The data collected from all filters for the same excitation wavelength share the same normalization factor and are therefore comparable. The nanoflower response signal recorded with all filters is in good agreement with each other. Hence, the data from measurements with different filters can be compared.

spectra of the gold nanoflowers at different excitation wavelengths λ_{exc}, normed to their average values in the wavelength range from 760 nm to 770 nm. The signals were measured with longpass filters with cutoffs at Figure 4.3a) 540 nm and Figure 4.3b) 650 nm. Just above the filter at 540 nm, the signal strength greatly decreases with increasing excitation wavelength. The signal above 620 nm, on the other hand, only reveals minor changes for λ_{exc} until at least 530 nm. This further indicates the dependence on LSPR. As a result, it is implausible for this response signal to be caused by Raman scattering at the attached molecules, which would introduce significant shifts of the whole signal with the excitation wavelength. Consequently, it has to be generated by the nanopar-

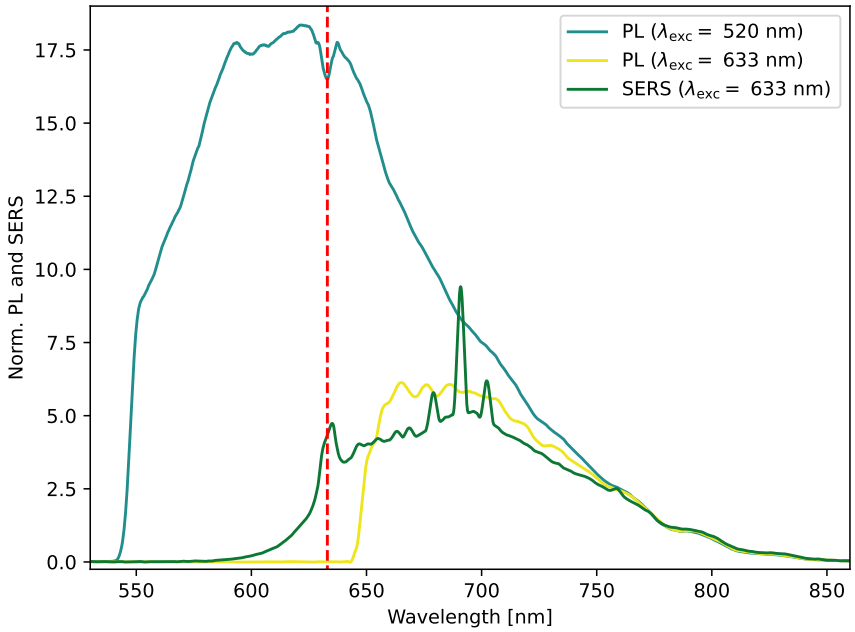

Figure 4.2: Comparison of photoluminescence (PL) signals of the Au nanoflower sample with 4-NTP of the same hot-spot excited at 520 nm (cyan) and 633 nm (yellow), with 540 nm and 650 nm longpass filters, respectively, and the Raman spectrum, also excited at 633 nm (green). They are normalized to their respective average in the range from 730 nm to 850 nm. The position of the Rayleigh peak of the SERS measurement is indicated by a red dashed line. The dip around 633 nm in the 520 nm response is due to light passing through a volume Bragg grating essential for the SERS measurements. While both response spectra show no vibrational Raman peaks of 4-NTP due to the large bandwidth of 10 nm of the incident light, all three spectra show similar monotonous decreases above 700 nm.

ticles themselves, aligning with previous research [1, 7, 16, 26, 28, 49, 51, 69, 75, 82]. As shown in Figure 4.3b) for higher λ_{exc}, the signal continues to change, such that a decrease in the signal can also be detected at higher emission wavelength ranges. Apart from the LSPR enhancement, there has to be another wavelength-dependent property. This behavior is assigned to interband excitations of the 5*d*-band, as explained later in section 4.2 and 4.3. On a side note, The shifting peak between 700 nm and 750 nm is a feature of the supercontinuum laser. It is not present at higher excitation wavelengths, since the light passed through a 750 nm short-pass filter before hitting the sample.

While the differentiation between photoluminescence (PL) and electronic Raman scattering (ERS) is beyond the scope of this thesis, the focus instead lies on different aspects of the nanoflower response spectra and, consequently, the SERS background. To facilitate a clear distinction between the two analysis methods, Raman measurements with the narrow bandwidth laser 633 nm are referred to as SERS, and the nanoparticle response spectra acquired using the supercontinuum laser as photoluminescence (PL) or response spectra. In the upcoming sections, the dependence of the nanoparticle response on the excitation wavelength is explored.

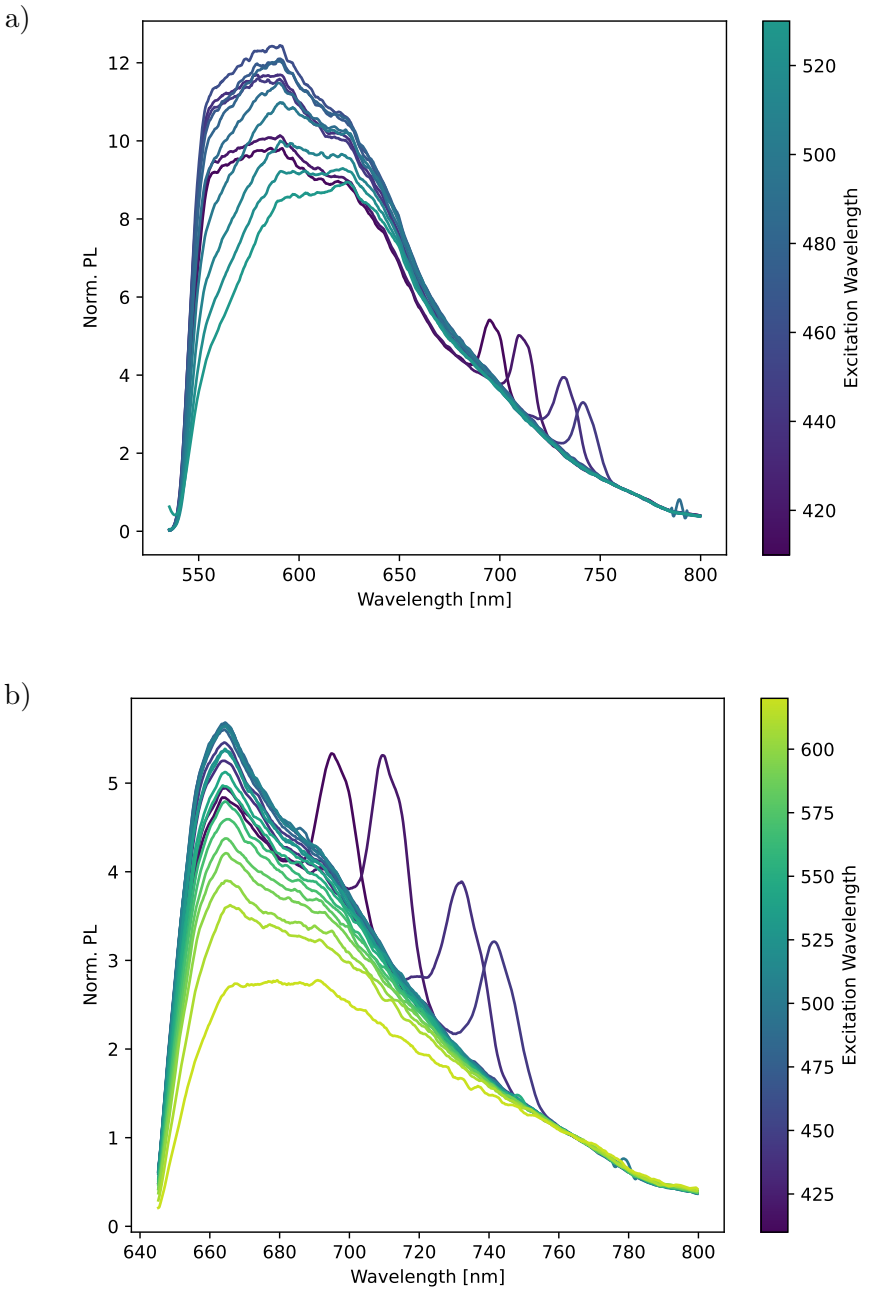

Figure 4.3: Au nanoflower photoluminescence (PL) spectra above a) 540 nm and b) 650 nm. The nanoflowers were excited by different wavelengths ranging from 410 nm to 520 nm or 620 nm, respectively, as shown in the color bar. All spectra are normalized to their average in the range from 760 nm to 770 nm. a) reveals great differences in the emission below 620 nm supposed to originate from interband transitions. While in a) the nanoflower spectra above 630 nm are similar, b) demonstrates further changes at higher emission and excitation wavelengths. Between 700 nm and 750 nm there are peaks originating from the light source. They shift with the excitation wavelength and vanish above 750 nm since the light passes through a 750 nm short-pass filter before hitting the sample.

4.1 Photoluminescence Excitation Spectra

Changing the excitation wavelength influences the strength of the nanoflower emission. Response spectra at the same spot and laser power, but different excitation wavelengths λ_{exc} are shown in Figure 4.4 for above a) 540 nm and b) 650 nm, respectively. They are not scaled to each other. Indeed, it is noticeable that the intensity of the nanoparticle emission diminishes as the excitation wavelength increases. This observation suggests higher photon energies are more likely to trigger the underlying processes.

As mentioned earlier, the photoluminescence resembles the LSPR. Cai et al. [16] show that the shape of the photoluminescence does not change for λ_{exc} as high as 785 nm and therefore attribute it to intraband emission. In contrast, the signal changes with λ_{exc} in the experiment conducted here, as depicted in Figure 4.3. Additionally, the overall PL intensity is still increasing for excitations below 550 nm, which is below the LSPR maximum, as presented in Figure 4.4. Thus, the PL signal can not be solely explained by wavelength-independent, LSPR-enhanced, intraband processes. Hence, the overall strength of the PL signal is further investigated for different excitation wavelengths in this section.

The highest excitation wavelength used in this experiment is 633 nm, which is equal to 1.96 eV. This is still enough energy to excite some interband transitions in gold with a minimum band-to-band distance of around 1.8 eV to 1.94 eV [20, 41, 62]. Nevertheless, interband emissions always require previous interband absorption, because the $5d$-band is fully occupied in the ground state. The emission process itself thus can not cause the amplification of the signal. Generally, the rise of the overall signal strength indicates an increase in absorption with decreasing λ_{exc}.

Figure 4.4 reveals, that the signal intensity is not monotonous increasing with decreasing excitation wavelength. For a clearer view, the photoluminescence intensity was averaged over the spectrum and depicted versus the excitation wavelengths, creating photoluminescence excitation (PLE) spectra, which express the absorption of the nanoflowers. In Figure 4.5, different PLE spectra are shown for the same series of measurements as depicted in Figure 4.4. Hereby, not the whole spectrum was taken into account, which would only result in one PLE spectrum. Instead, the different lines show PLE spectra averaged over distinct emission wavelength ranges. The region compromised by the laser feature was avoided. Besides, for all ranges below 666 nm, the spectra measured with the 540 nm longpass filter were used. Therefore, they end at $\lambda_{exc} = 540\,\text{nm}$. In Figure 4.5a), the data is shown in the measured unit $\frac{counts}{\mu W \cdot s}$, while in Figure 4.5b), the excitation spectra are normalized to their averaged values in the range $\lambda_{\text{exc}} = 448\,\text{nm}$ to 495 nm.

Since the PLE spectra contain information about the PL signal strength, they are correlated to absorption processes in the nanoparticle and reveal different features. At first, all spectra peak around 440 nm. Thus, the absorption decreases most likely for even higher excitation energies. Also, the signal changes for the various emission regions. The non-normalized spectra in Figure 4.5a) indicate an overall decrease of the PLE with increasing emission wavelengths. This is due to PL signals decreasing for wavelengths above 560 nm. Moreover, the slope of the PLE spectra varies. Hence, the differences in the signal strength between the excitation wavelengths diminish for higher emission wavelengths. At last, at λ_{exc} around 560 nm, an additional peak is visible. To further investigate this, absorption and scattering spectra of the nanoflower films are

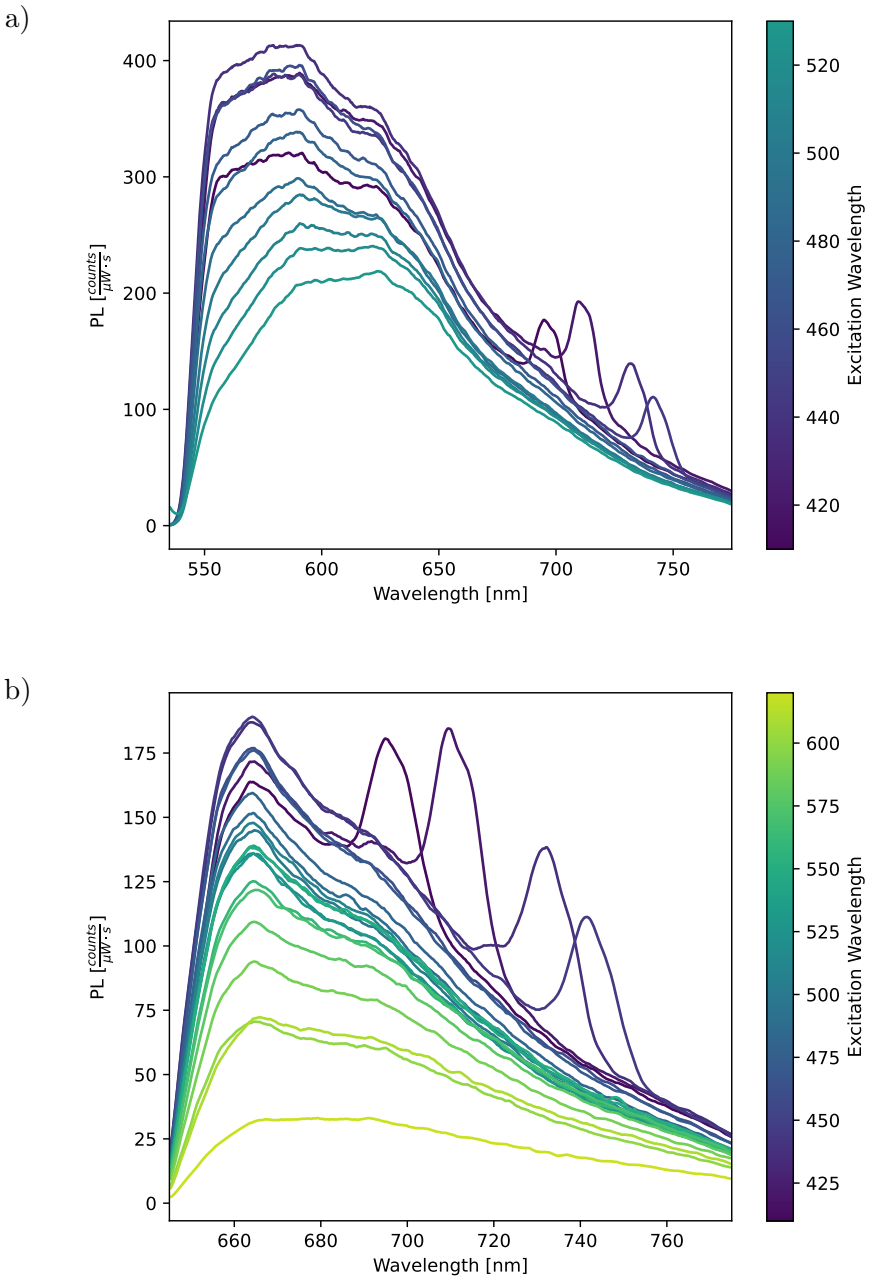

Figure 4.4: Stokes gold nanoflower photoluminescence (PL) spectra for several excitation wavelengths between 410 nm and 633 nm, as indicated by the color bar, with incident light blocked by a) 540 nm and b) 650 nm long-pass filters in front of the spectrometer, respectively. All spectra were measured at the same laser power at the sample and are shown normalized only to the laser power and exposure time of the spectrometer. Peaks shifting with the excitation wavelength between 700 nm and 750 nm originate from the light source. They vanish above 750 nm since the light passes through a 750 nm short-pass filter before hitting the sample. The overall signal strength shrinks with increasing excitation wavelengths.

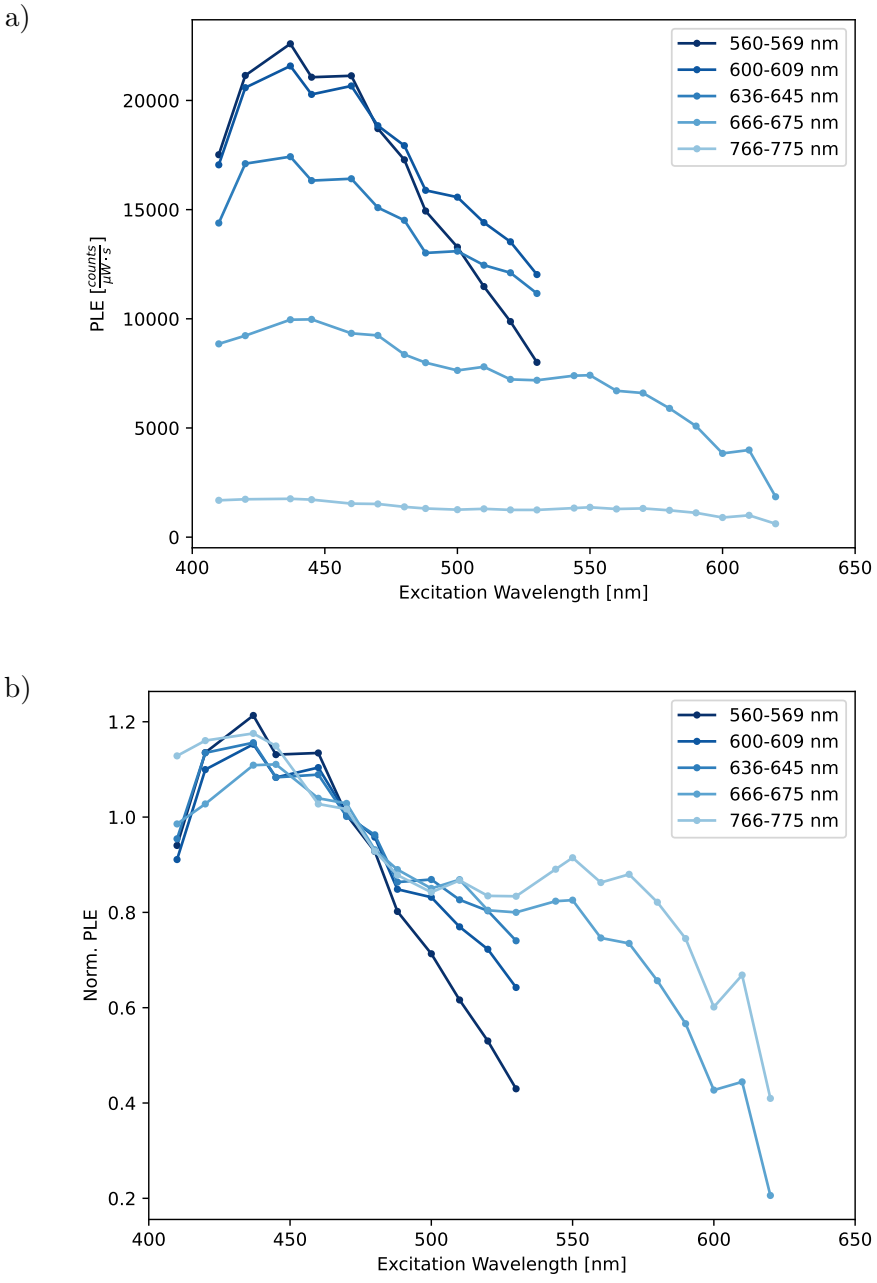

Figure 4.5: Photoluminescence excitation (PLE) spectra of the Au nanoflowers on Si. To achieve this representation, the photoluminescence spectra were averaged over different ranges, as indicated by the legend, for each excitation wavelength. The region compromised by the laser feature (700 nm to 750 nm) was avoided. The PLE is shown in a) counts per laser power and exposure time and b) normalized to the average of the PLE in the excitation range from 445 nm to 495 nm.

shown and discussed in the next section.

4.2 PLE vs. Absorption

Because the substrate of the so far inspected nanoflower sample is silicon, no transmission measurements in the optical region are possible. Therefore, another gold nanoflower sample was created on glass. This sample's respective PL and PLE spectra are depicted in Figure A.1 and Figure A.2 and discussed throughout this section. In Figure 4.6, the absorption (grey dash-dotted) and scattering (grey dotted) spectra from the glass substrate sample are shown. They are compared in a) to a representative PL spectrum ($\lambda_{exc} = 480\,\text{nm}$) (dark blue) and a PL spectrum of the sample on Si (purple dashed), and b) to the PLE spectrum of the nanoflowers on glass, measured in the emission range from 766 nm to 775 nm. The new nanoflowers reveal photoluminescence similar to the other sample on Si, but the absorption and scattering indicate no correlation to the nanoflower response and thus the LSPR. This is unexpected, since in general, the LSPR peak should be evident in nanoparticle loss spectra, as demonstrated in the extinction spectrum in Figure 3.2. Furthermore, the only similarity between absorption and PLE is that both decrease in the range from 445 nm to 480 nm. On the other hand, the absolute values of the absorption spectrum can differ from the PLE since the sample is inhomogeneous and the PLE is only measured on a small spot while the absorption is measured in a large area. On the other hand, the shapes of the signals should resemble each other in some way, but this is not the case for most parts. The scattering spectrum also provides no clues on the shape of PL and PLE, contrary to several reports in the literature [16, 33].

The absorption and particularly the scattering spectra are more related to the extinction coefficient κ of single crystal gold measured by Olmon et al. [78], as depicted in Figure 4.7. All three curves are normalized to their minimum at 480 nm. I. e., the elastic UV-vis spectra of the strongly clustered nanoflowers seem to behave more like bulk gold, but apparently the PL and PLE do not. Instead, the interband-only part of the extinction coefficient κ_{IB} shown in Figure 4.8 matches the different PLE spectra quite well in the region above 440 nm. To show this, the dielectric function ε, taken from Olmon et al. [78], was corrected by its Drude part. For this, the Drude part was calculated with Equation 2.9 and the values for ω_p and γ as presented by Blaber, Arnold, and Ford [9]. Afterward, the interband permittivity ε_{IB} was converted into the refractive index and ultimately its imaginary part κ_{IB}.

The shape of κ drastically alters without the Drude part, especially above 500 nm. The PLE closely resembles pure interband absorption, thus indicating the PLE depends strongly on interband transitions. Particularly, the PLE of the nanoflowers on glass is dominated by interband transitions. This is in contrast to the earlier introduced mechanisms of photoluminescence and electronic Raman scattering (section 2.3), which only covered intraband transitions but aligns well with the results of previous research showing enhancement of the PL (or ERS) due to interband absorption [16, 97]. Considering the PLE of the nanoflowers with a silicon substrate, only emissions measured in low wavelength regions (Figure 4.8, dark blue dashed line) seem to follow the trend of κ_{IB}. For higher emission and excitation wavelengths, there is a distinction between the photoluminescence excitation spectra of both samples. The sample on Si deviates from κ_{IB}, which indicates additional absorption. As a rough guess, the difference between the PLE spectra of both samples in the emission range from 766 nm to 775 nm,

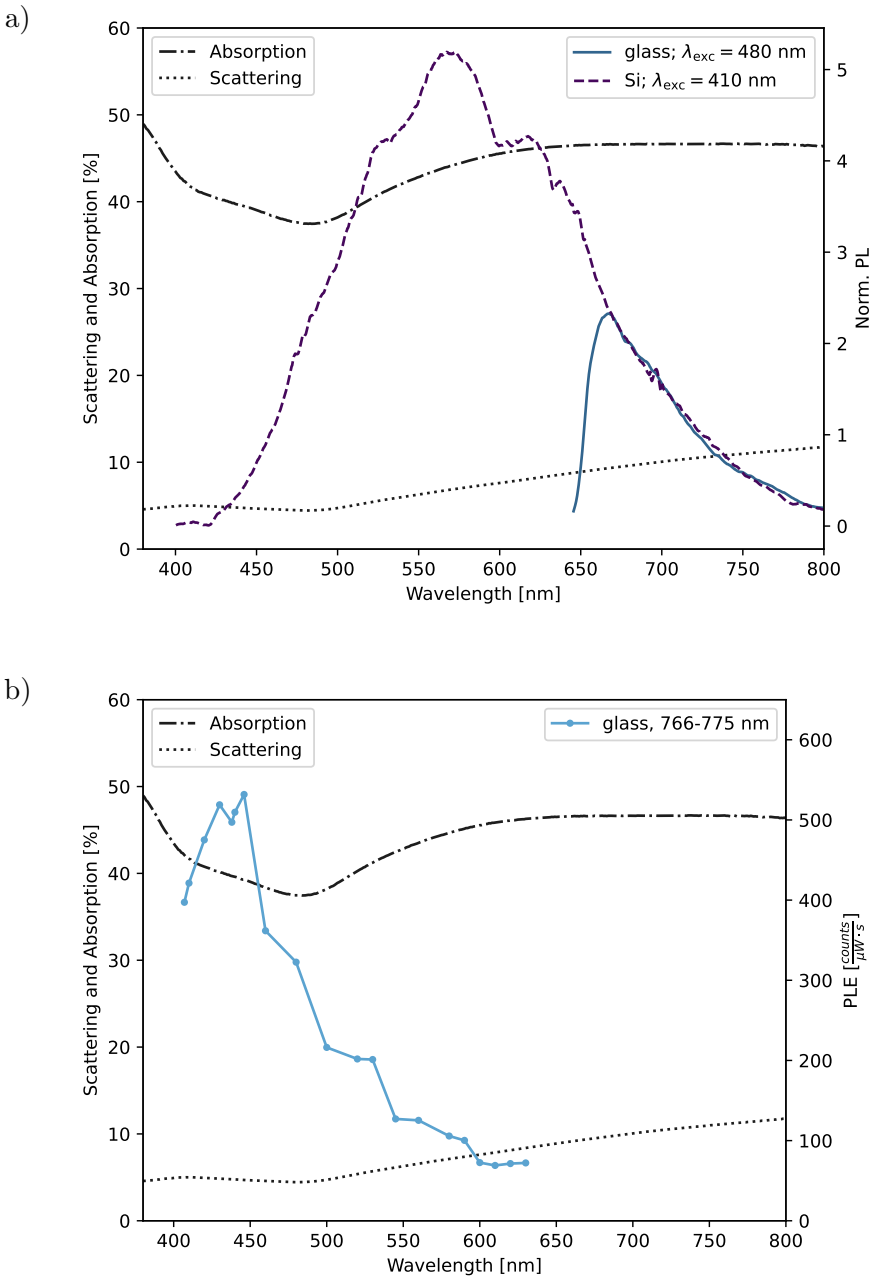

Figure 4.6: Different spectra of gold nanoflowers. left axis: a) and b) absorption (grey dash-dotted) and scattering (grey dotted) spectra as a percentage of the incident light of nanoflowers on glass. right axis: a) photoluminescence (PL) measured at 480 nm excitation on a glass substrate (dark blue) and at 410 nm on a Si substrate (purple dashed) averaged to their signal above 666 nm, respectively. b) PLE spectrum of gold nanoflowers on glass measured in the emission range from 766 nm to 775 nm. While the shape of the PL (and thus the LSPR) signal is independent of the substrate, the absorption and scattering spectra have no similarity to the PL. The only connection between absorption and PLE is that both decrease in the range from 445 nm to 480 nm.

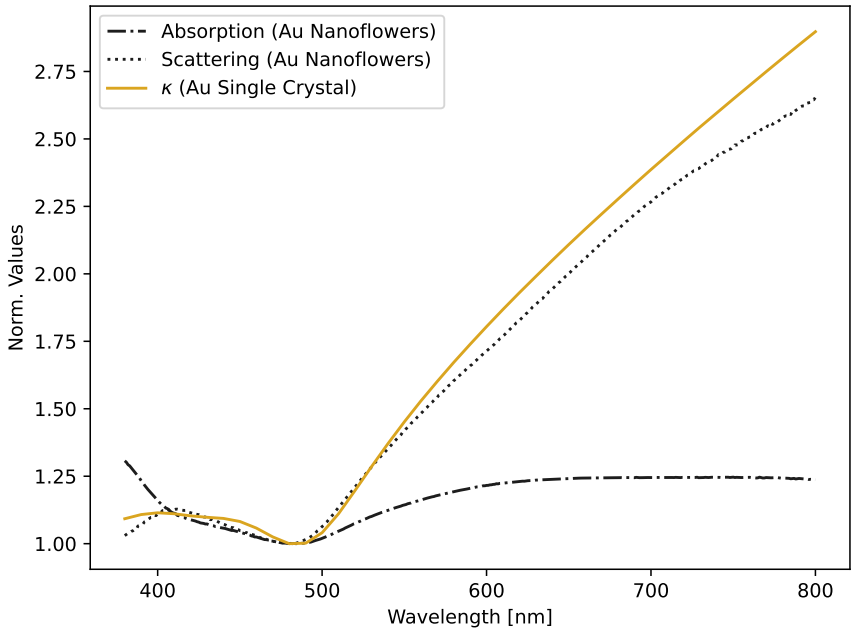

Figure 4.7: Absorption (black dashdotted) and scattering (black dotted) of the Au nanoflowers on glass and extinction coefficient κ of single crystal Au by Olmon et al. [78] (golden). All curves are normalized to their minimum value, respectively. While all three graphs have their minimum around 485 nm, especially the scattering spectrum and κ of bulk gold resemble each other.

as they are shown Figure 4.8, was calculated and depicted in Figure 4.9. This difference (black) is compared to a photoluminescence spectrum of the Si sample (purple dashed). Both curves are averaged over the range of the difference spectrum and they show similarities. As stated before, the PL resembles the plasmonic resonance (LSPR) of the nanoparticles [16, 33]. Hence, the deviation of the Si sample may be explained with a stronger dependence on the plasmonic enhancement. Since a single PLE spectrum still contains information about the absorption process and not the emission, this shows the role of the LSPR enhancement in the absorption process. It is important to note, that both intraband and interband absorption can be enhanced by plasmons [74]. Therefore, the presence of the LSPR peak does not necessarily confirm the existence of intraband transitions. However, the deviation between low- and high-energy emissions indicates different absorption processes, despite being excited by the same wavelength. Thus, the additional plasmonic enhanced absorption may be attributed to a higher relevance of intraband processes. In contrast, the emission of high-energy photons is dominated by pure interband absorption, as revealed by the different slopes in the PLE of Figure 4.5b). In this regime, LSPR enhancement seems to play no significant role in the absorption process. The cause of the difference in the PLE between both samples in the low-energy region remains uncertain. It is possible that different hot spots on the same sample exhibit diverse contributions of pure interband and plasmonic effects in the response signal. This could be attributed to the fact that on clustered nanoflower samples, not

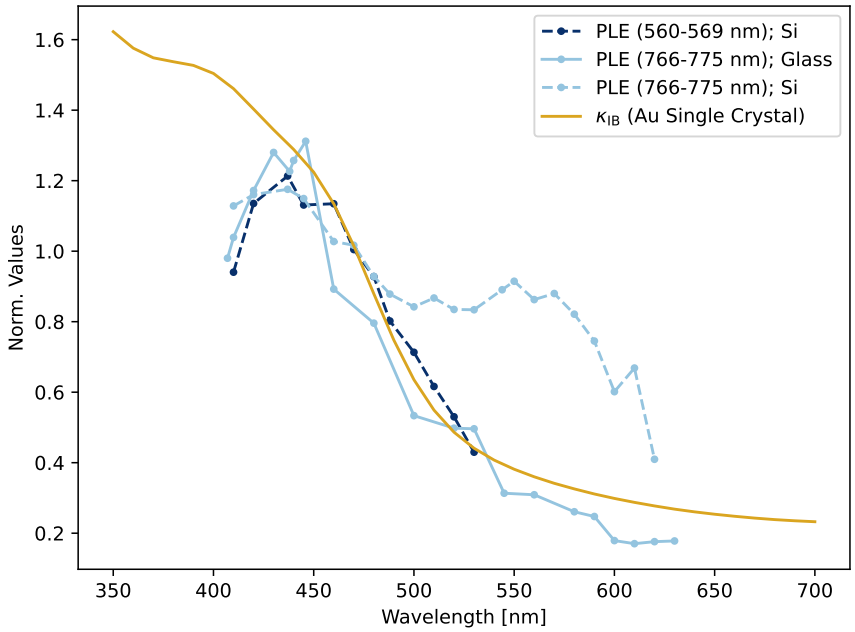

Figure 4.8: Different photoluminescence excitation (PLE) spectra (blue) of Au nanoflowers on glass (solid) and Si (dashed), respectively, with their averaged ranges indicated by the legend. Additionally, the interband-only part of the extinction coefficient κ_{IB} of bulk Au is shown (golden). κ_{IB} was calculated with data from Olmon et al. [78] and Blaber et al. [9]. All spectra are normalized over their average values in the range from 445 nm to 495 nm, respectively.

only the shape of the particles plays a role. Also, their positions relative to each other are crucial since extreme field enhancements can occur in the gaps between nanoparticles [37, 39, 65, 90]. Hence, the plasmonic enhancement can strongly deviate between different hot spots. Also, the absence of plasmonic enhancement in the PLE spectra of the glass sample may be associated with the fact that scattering and absorption spectra are similar to bulk gold, as shown before in Figure 4.7. To confirm this, multiple hot spots need to be measured on both samples. Moreover, other nanoparticle clusters with well-known LSPR, like spheres or rods, should be examined to compare if their PLEs follow the same interband and LSPR properties. Also, the decrease of the PLE below 440 nm is not fully covered. Since the plasmonic enhancement decreases below 560 nm, as indicated by the response spectra in Figure 4.1, this perhaps outweighs the increase due to stronger interband absorption below 440 nm. Hence, in this region, the excitation process would be dominated by pure interband transitions without any LSPR enhancement. This also has to be discussed further in future projects.

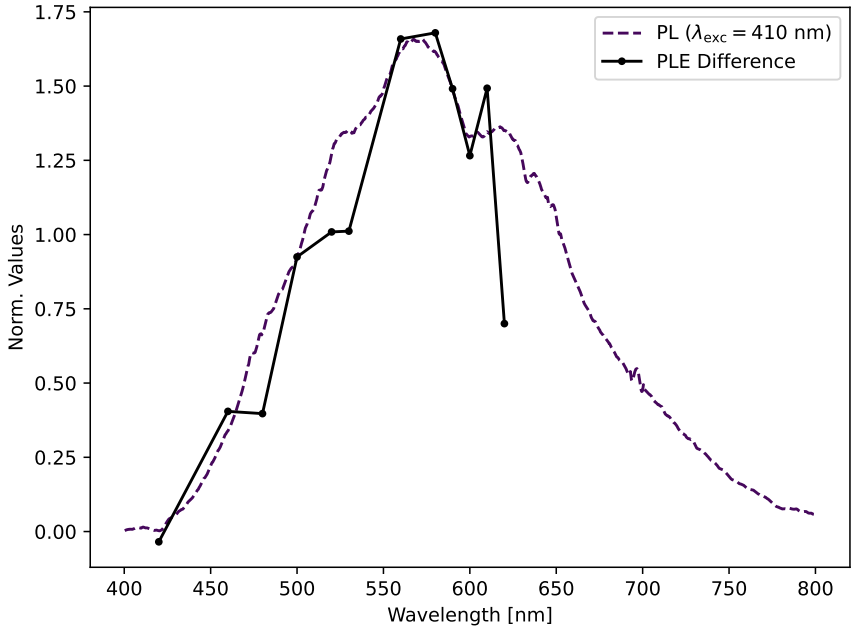

Figure 4.9: Difference of the PLE spectra from the gold nanoflower samples on glass and silicon emitted at 766 nm-775 nm, as depicted in Figure 4.8 (black solid), compared to the photoluminescence spectrum of the sample on Si excited at 410 nm (purple dashed). Both curves are normalized to their maximum, respectively, and show similar characteristics.

4.3 5d-Band Excitation

Given that interband absorption appears to enhance the response strength of the gold nanoflowers, the question arises as to which mechanism is responsible for this effect. The differences in the photoluminescence in Figure 4.3 below 620 nm in particular can be explained with interband transitions. Two options for interband absorption can occur, direct and indirect interband transitions. Both types and the related emission paths are demonstrated in Figure 4.10 1)-4). Before each radiative decay, the excited electrons and holes can interact with the crystal lattice via phonons to some degree. For simplification, only the radiative parts of the decay paths are discussed. The direct excitations 1)-3) populate empty states above the Fermi level. These transitions require no additional momentum and excite real states. There is no reason to consider ERS here.
At first, the excited electrons could decay via 1) intraband transitions. For this, they recombine with an empty state around the Fermi level E_F under additional momentum transition. Only in a small range below the E_F, empty states are available due to the finite temperature of the system. Interband transitions excited by up to 3 eV, as used in this experiment, can only elevate electrons less than 1.5 eV above E_F. This can be approximated from the presented gold band structure (Figure 2.4) or by calculating the hot-carrier generation rates for gold nanospheres [55]. Hence, the maximum energy for intraband emitted photons is still in the IR range below 825 nm for the excitation wavelengths used in this experiment. I. e., this process does not enhance the optical region of

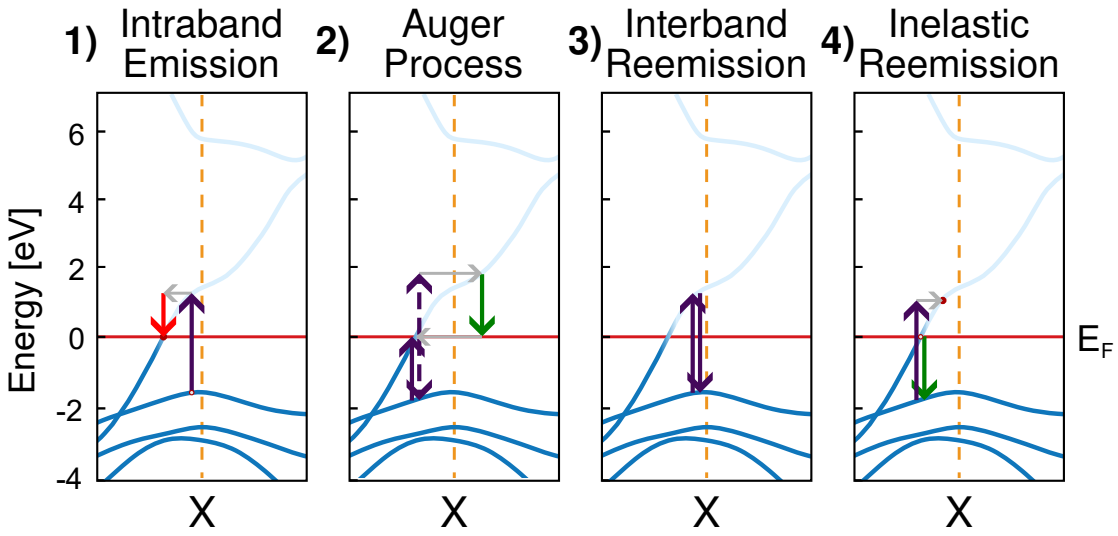

Figure 4.10: Possible origins of the nanoparticle response with interband excitation of electrons: 1) intraband emission, 2) Auger process as suggested by Cai et al. [16], 3) elastic interband reemission, and 4) inelastic interband reemission. The band structure of gold is adopted from Stete [85].

the nanoparticle response observed here. Besides, in this process, a hole remains in the 5*d*-band that possibly can recombine with another electron after additional excitation or traveling along the band due to scattering processes. For excitation energies close to the minimum interband energy at the position, where Fermi level and 6*sp*-band cross, the hole can recombine without further lattice interactions. This leads to emissions around the excitation energy and is comparable to the effect of 3) elastic interband reemissions, described later. Furthermore, the probability of intraband emissions after interband excitations should be low for two main reasons. Firstly, in the infrared region, the PDOS remains low, resulting from the great distance to the LSPR enhancement. Secondly, the lifetime of such an intraband PL relaxation ($\approx 1\,\mathrm{ps}$) is expected to be much higher than the lifetime of the *d*-band hole ($\leq 50\,\mathrm{fs}$) [16, 103]. Consequently, interband reemissions should be favored.

To create visible inelastic emissions, Cai et al. [16] propose 2) an Auger process that further raises the energy of the excited electron while another electron recombines with the available *d*-band hole. This enables intraband emissions in the optical range but requires either interaction with electrons around and below the Fermi level or multiple excited electrons simultaneously. The former enables emissions with an energy maximum roughly equal to the interband transition since the electron can only be elevated by this amount above the Fermi level. This leads to emissions in the visible spectrum that account for the increase in the PLE due to interband absorption. Multiple excited electrons at the same time, on the other hand, necessitate high intensities due to the short lifetimes of *d*-band holes [16, 103].

Otherwise, 3) direct interband reemission would occur. Here, the excited electrons can recombine with the hole state they were excited from. This interband reemission is mostly elastic and therefore near the excitation wavelength [16]. This cannot explain,

why the signal strength below 620 nm decreases, while the excitation wavelengths are getting closer to the filter edge, as observed in Figure 4.3.
At last, this thesis suggests that absorption may also occur with the aid of wavevector transfer to accomplish 4) inelastic interband reemission (IIR). Here, an excitation occurs in positions of the band structure where the interband distance is less than the incident photon energy. Consequently, additional momentum is transferred to reach an available, empty state. This should be possible since otherwise momentum-forbidden intraband processes, as presented before as PL, also occur in metal nanoparticles. If, instead, electronic Raman scattering is the underlying process, a virtual state above the 6*sp*-band is excited. The excited electron can then relax on several paths involving IR intraband emission and non-radiative decay. Additionally, the remaining hole state in the *d*-band can recombine with another electron below the Fermi level.
For this inelastic interband reemission, two conditions have to be met. Firstly, the excitation of a *d*-band electron must occur in a location in the k-space, where the *sp*-band above is occupied. Secondly, the incident photon has to provide enough energy to excite the electron above E_F to access an empty state. The emission induced by the relaxation of a ground state electron from the *sp*-band into the *d*-band hole has the energy of the associated direct interband transition. In contrast to the almost elastic reemission process described in 3), this emission can have significant energy differences from the incident photons. The maximum energy of an emitted photon enabled by this process corresponds to the minimum energy of direct interband absorption in this region of the band structure. Around the *X*-point, this energy maximum is at about 1.8 eV to 1.94 eV ($\approx$ 690 nm to 640 nm) [41, 62]. This does not explain the changes in emissions below 620 nm for different λ_{exc}. Also, the Fermi level can be reached by all excitation wavelengths used in this experiment. Hence, no differences should be observed in the emission spectra. At the *L*-point, however, the emission wavelength can be $\approx$ 510 nm [41, 62] or higher. This includes the spectral region below 620 nm, where the strongest changes between the gold response spectra are observed (compare Figure 4.3). Hence, IIR forms an alternative to Auger-like excitation. To determine which emission process is more likely, the minimum excitation energies required to emit photons at different energies around the *L*-point were calculated from gold band structures of different references [25, 41, 81]. These calculations are approximated for $T = 0\,\mathrm{K}$. $\Delta E_{\mathrm{abs,min}}$ is the minimum energy needed for a specific emission energy ΔE_{emi}. For the Auger excitation, ΔE_{emi} is the difference of the excited state in the 6*sp*-band E_{sp} and E_F and two times $\Delta E_{\mathrm{abs,min}}$ is the energy needed to reach the excited state from the *d*-band E_{d}. This is shown in Figure 4.11a) for an exemplary photoluminescence process at the *L*-point. Thus, both values can be calculated by the following equations:

$$\Delta E_{\mathrm{emi}}(k) = E_{\mathrm{d}}(k) + 2\Delta E_{\mathrm{abs,min}}(k) - E_F(k) \tag{4.1}$$

$$\Delta E_{\mathrm{abs,min}}(k) = E_{\mathrm{sp}}(k) - E_{\mathrm{d}}(k) \tag{4.2}$$

For IIR, as illustrated in Figure 4.11b), ΔE_{emi} at a certain point in the band structure is the difference between 6*sp*-band E_{sp} and 5*d*-band E_{d}, while the difference between

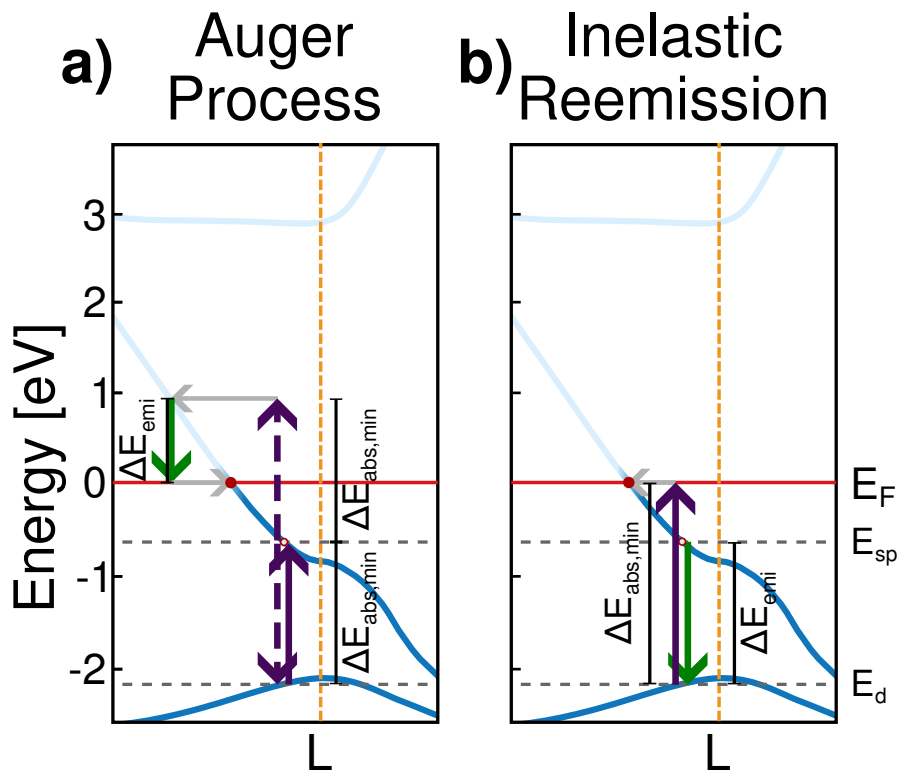

Figure 4.11: a) Auger process and b) inelastic interband reemission at the L-point. Both processes show emissions in the visible spectrum. The required minimum absorption energy $\Delta E_{abs,min}$ and the corresponding emission energy ΔE_{emi} for the processes at a specific point in the bandstructure can be calculated with the energies of the $5d$-band E_d and $6sp$-band E_sp and the Fermi energy E_F via Equation 4.1-4.4.

E_F and E_d is equal to $\Delta E_\mathrm{abs,min}$. Both values are presented as follows:

$$\begin{aligned} \Delta E_\mathrm{emi}(k) &= \Delta E_\mathrm{abs,min}(k) + E_\mathrm{sp}(k) - E_F(k) \\ &= E_\mathrm{sp}(k) - E_\mathrm{d}(k) \end{aligned} \tag{4.3}$$

$$\Delta E_\mathrm{abs,min}(k) = E_F(k) - E_\mathrm{d}(k) \tag{4.4}$$

Both $\Delta E_\mathrm{abs,min}$ and ΔE_emi are illustrated against each other for the two processes and for four analyzed gold band structures in Figure 4.12 with their corresponding wavelengths $\Delta\lambda_\mathrm{abs,max}$ and $\Delta\lambda_\mathrm{emi}$. Since all band structures are simulated somehow and only bulk gold was considered, they all differ from the real situation in the studied nanoparticle system. Consequently, the calculated values are only rough estimates. $\Delta\lambda_\mathrm{abs,max}$ in the band structure indicates the initiation point of the emission process for specific $\Delta\lambda_\mathrm{emi}$. Hence, all absorption energies depicted above the lines can enable the respective emission process. However, Figure 4.12 does not provide any information about the efficiency or the shape of the emission for specific excitations. With inelastic interband reemission considered in Figure 4.12a), the differences between the band structures are larger. On the other hand, the slope in Figure 4.12b) with the Auger excitation is steeper. Both emission processes can be relevant for emissions from 550 nm to 620 nm. In

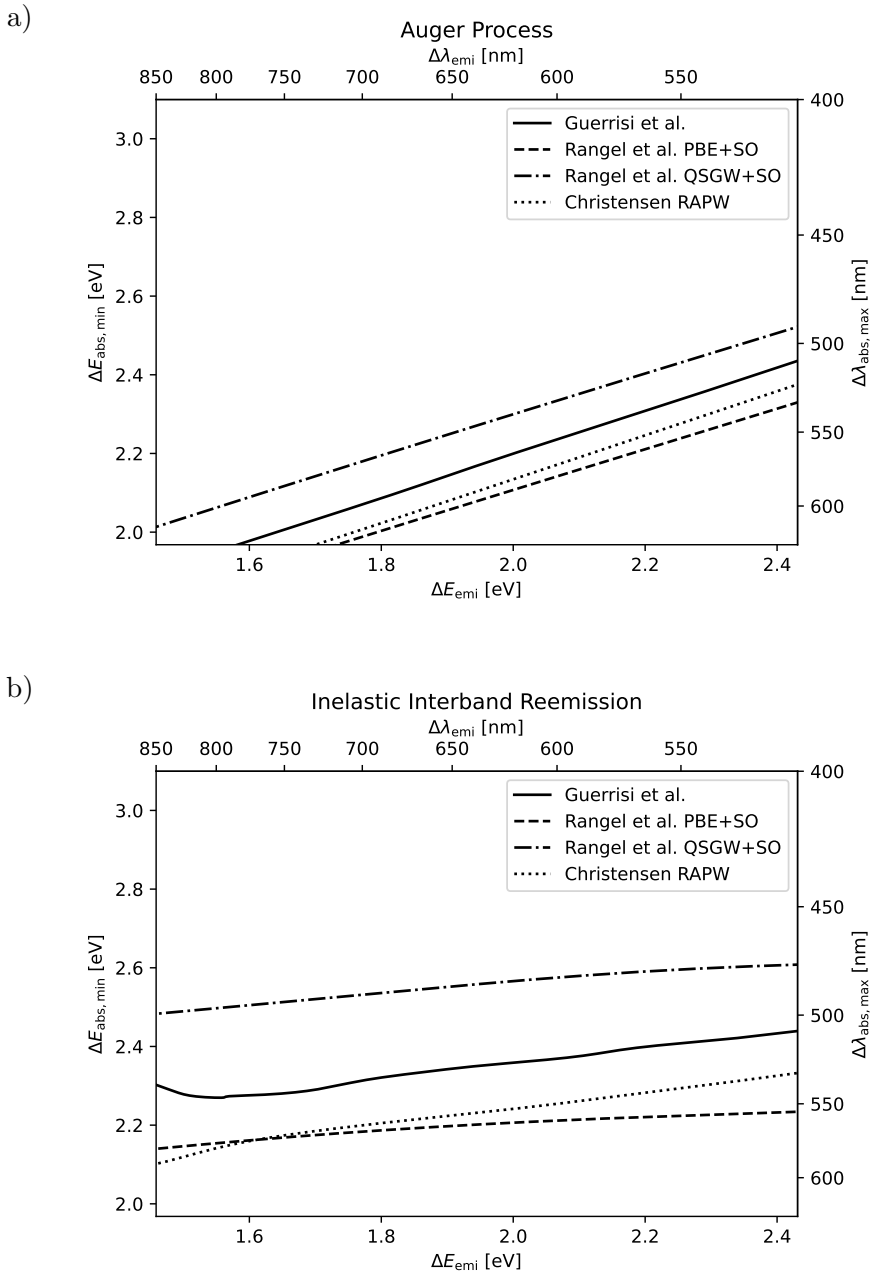

Figure 4.12: Minimum required photon energy $\Delta E_{\mathrm{abs,min}}$ for emissions at energy ΔE_{emi} around the L-point with corresponding wavelengths $\Delta\lambda_{\mathrm{abs,max}}$ and $\Delta\lambda_{\mathrm{emi}}$ for a) Auger processes and b) inelastic interband reemission. The values are calculated via a) Equation 4.1 and 4.2 and b) Equation 4.3 and 4.4 from different band structures published by Guerrisi, Rosei, and Winsemius [41], Rangel et al. [81], and Christensen [25], as noted in the legend. Both can roughly explain changes in the PL signal below 620 nm, but Auger-like processes better fit the observations for higher emission wavelengths.

this emission range, changes in the PL signal were observed at λ_{exc} from approximately 445 nm to 530 nm in Figure 4.3a), which overlaps with the $\Delta\lambda_{abs,max}$ of both processes in this emission range. For higher emission wavelengths, as shown in Figure 4.3b), Auger excitation seems to be more likely. All emissions until at least 850 nm should be forbidden for excitations at 600 nm and above with inelastic reemission. Hence, the observations in Figure 4.3b) can not be described by inelastic interband emissions alone. The Auger process gradually shifts the required wavelength and matches the observations better.
The same calculations evaluated at the X-point are shown in Figure A.3. Both processes at the X-point do not explain any changes observed in the PL signal, as only light above ≈ 640 nm is emitted and these emissions are enabled by every λ_{exc} used in this experiment. However, these emissions may explain the additional absorption observed at high emission wavelengths, as depicted in Figure 4.8. Why only the X-point emissions would show LSPR enhancement, remains unclear. Thus, intraband-only emissions are still a valid option.
Non-radiative scattering of excited electrons and holes as well as LSPR enhancement have to be taken into account to explain the whole picture of the changes between the λ_{exc} in Figure 4.3 without the rather sharp cutoffs calculated in Figure 4.12 for Auger excitation and IIR. Furthermore, the region of the nanoparticle response closer to the Rayleigh peak has to be examined. This could provide information about the minimum PL emission wavelength possible with both processes for specific excitations, as this minimum likely differs from the direct interband reemission wavelength. Additionally, using smaller bandwidth light sources and investigating single nanoparticles or more defined structures such as Dimers and Trimers [65] could offer a greater resolution of the response signal and its starting edge. Moreover, a more precise determination of the band structure, considering the properties of nanoparticles, could help to narrow down the range of $\Delta\lambda_{abs,max}$.

While the presented experiments can not distinguish between photoluminescence and electronic Raman scattering, it is evident that the response originates from the gold nanoflowers themselves and strongly depends on LSPR enhancement and the intrinsic properties of gold. The dominance of interband processes at the L-point in the nanoparticle response was shown with photoluminescence excitation spectra. Additional absorption was observed at high emission wavelengths. This may be caused by intraband processes or interband absorption at the X-point. This dependence of the response signal on the excitation wavelength is in agreement with the work of different researchers showing that the yield of the response signal relies on the overlap of the excitation with both LSPR [23, 87] and interband transitions [16, 97] to enhance absorption or emission.
The nanoparticle response is ubiquitous in SERS spectra and denoted as a continuous background since most measurements aim for the Raman peaks of the attached molecules. Therefore, many approaches are known trying to eliminate the SERS background via shaping of the nanoparticles or data processing [4, 6, 50, 100]. While this is meaningful for data analysis, the existence of the nanoparticle background is desirable since its dependence on the hot carrier distribution is crucial for example for the activation of photocatalysis [14, 68, 96].

4.4 Anti-Stokes SERS

Besides the Stokes shifted background, there is also an anti-Stokes (AS) signal. As stated in section 2.3, this is emitted light of ERS or PL processes inside the nanoparticles, too. However, the distribution of hot electrons and empty states dominates in the AS region over the LSPR enhancement. For this upconverted light, on average more than one photoabsorption is required [15]. To prove this, the power law exponents $k(\lambda)$ for the nanoflower responses were determined with the model in Equation 4.5, where I_{Signal} is the measured signal at laser power P. a and k are the fit parameters.

$$I_{\text{Signal}}(P, \lambda) = a(\lambda) \cdot P^{k(\lambda)} \tag{4.5}$$

The power law indicates the dependence on the intensity of the incident light and hence on the number of absorbed photons per emitted photon [15]. PL and SERS spectra of the gold nanoflower sample on glass were measured and analyzed for different laser powers. The power law exponents k are shown in Figure 4.13. In fact, the power laws for the Stokes parts at 520 nm excitation in Figure 4.13a) and the SERS spectrum in Figure 4.13b) both have values of k around one. Instead, in the anti-Stokes region, the power law exponent increases with distance to the Rayleigh peak. The higher the energy of the AS emission, the more photons are required on average before thermalization with the crystal lattice occurs [15, 82]. Since the anti-Stokes signal is closely related to the hot-carrier distribution of the nanoparticles, it also holds information about their electron temperature. Hence, Jollans et al. [56] state that the non-linear power law on the anti-Stokes side is caused by a combination of the rising photon count and the increasing electron temperature with higher powers, which strongly influences the anti-Stokes signal. The dependence of the anti-Stokes signal of the clustered gold nanoflowers on the temperature is discussed in the next chapter.

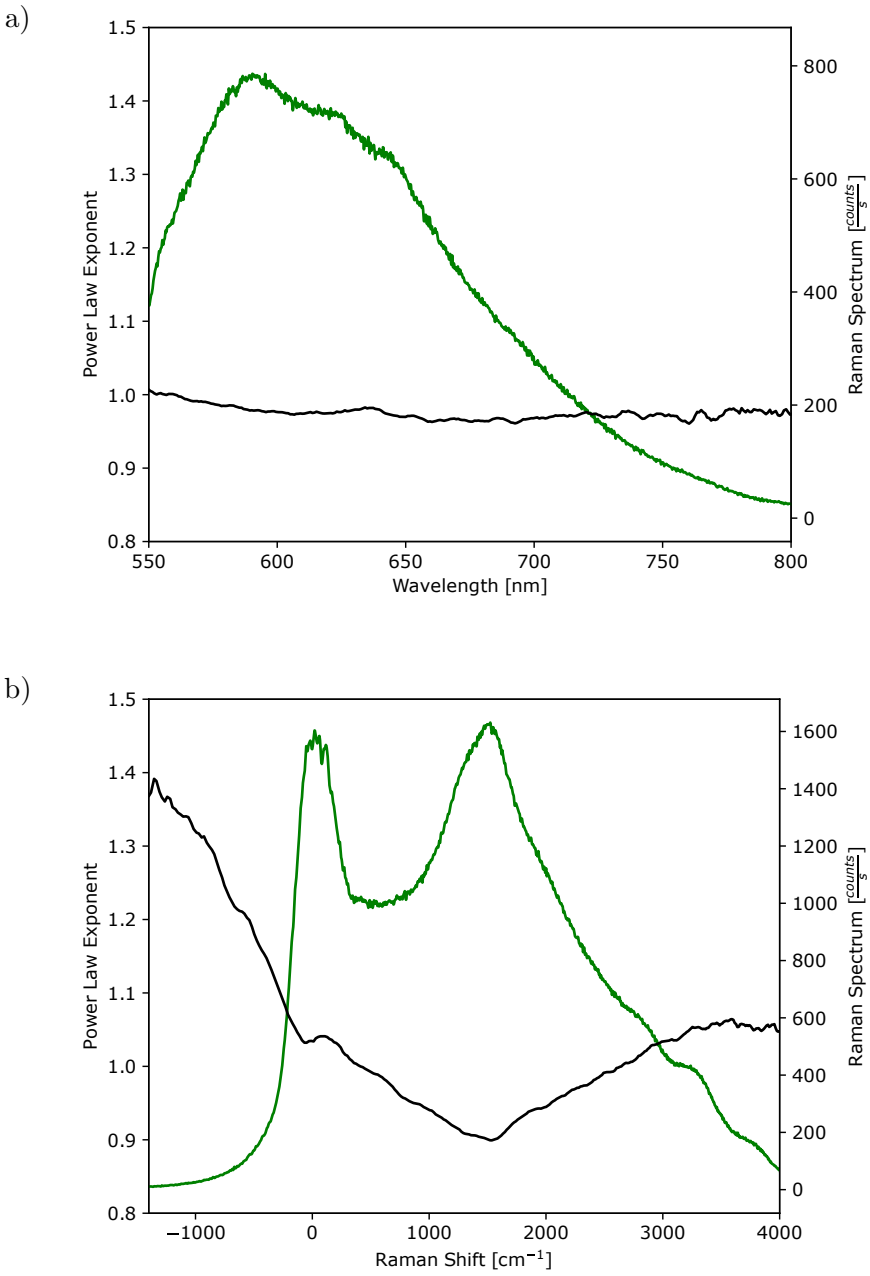

Figure 4.13: Spectrally resolved power law exponents k (black) for a) 520 nm excited PL and b) 633 nm excited SERS of Au nanoflowers on glass. A representative PL and SERS spectrum (green) are depicted, respectively .

Chapter 5

Gold Nanoflowers as Thermometers

Since the anti-Stokes nanoparticle response is also determined by the properties of the illuminated nanoparticles dependence on their temperature is observable [15, 19, 49, 56, 94, 95]. As described in section 2.4, the slope of the AS signal changes with the temperature. This is demonstrated in Figure 5.1 for gold nanoflowers. For this measurement, the sample holder was heated to different temperatures T_{env}. Unfortunately, the sample holder expanded thermally, which is why the measured spot could not be held constant. Thus, the signal strength changed in the Stokes region. Hence, the spectra are normalized to their respective integrated signal strength to emphasize the expected, decreasing slope with rising T_{env} in the anti-Stokes region. The Stokes regions instead remained largely unchanged apart from a factor due to the different plasmonic enhancements. This is especially useful for kinetic SERS measurements. While observing a molecule reaction by a change of Raman peaks, the temperature of the system can be recorded simultaneously with the same measurement. In this chapter, anti-Stokes thermometry, as introduced in section 2.4, is implemented for kinetic SERS measurements of gold nanoflowers. The measurements of different hot spots on the clustered sample are taken into account and the evolution of the temperature over time is discussed.
For temperature calculations, a range of Raman shifts from $-1040\,\mathrm{cm}^{-1}$ to $-460\,\mathrm{cm}^{-1}$ was chosen. At greater distances to the Rayleigh peak, the signal is strongly influenced by noise, particularly for low laser power measurements, while the Rayleigh peak itself dominates the signal above $-460\,\mathrm{cm}^{-1}$. The shape of the AS signals in this range on a logarithmic scale, as visible in Figure 5.1, can be described as linear. No relevant deviations in the calculated temperatures were determined while testing the Boltzmann, Fermi-Dirac, and Bose-Einstein distribution functions. Following these observations and previous studies [5, 15, 45, 49, 56, 86], a Boltzmann distribution was chosen for all temperature measurements.

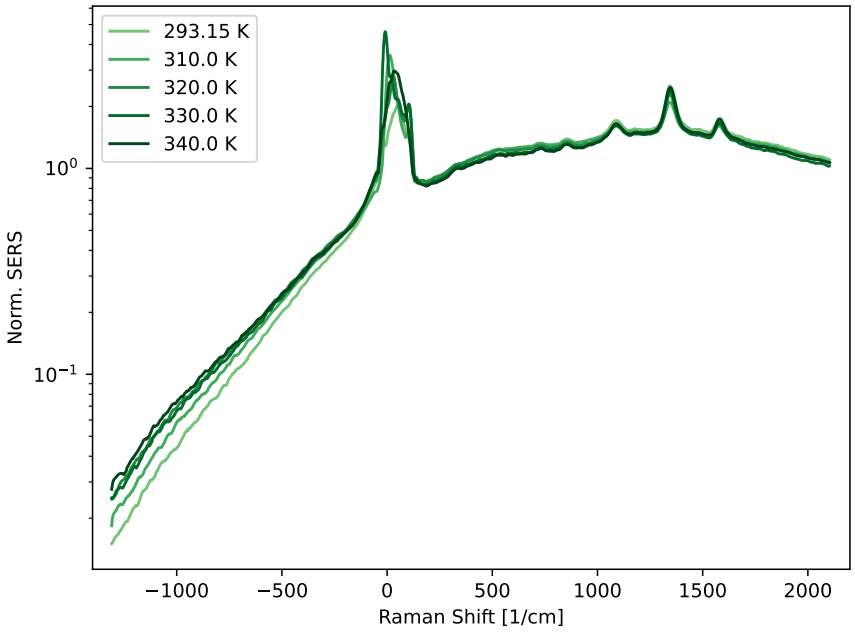

Figure 5.1: SERS spectra of the Au Nanoflowers and 4-NTP at different environment temperatures T_{env}, as noted in the legend. All graphs are averaged to their integrated signal strength. While the Stokes region remains nearly unchanged the slope of the anti-Stokes region decreases with rising temperature. The logarithmic illustration reveals the exponential decay of the anti-Stokes region to higher energy shifts.

5.1 Xie and Cahill Calibration

Following an approach by Xie and Cahill [95], an iterative calibration process was performed to enable absolute temperature measurements, as described in section 2.4. It determines the temperature rise due to laser heating as a function of laser power. This is illustrated in Figure 5.2, where the measured nanoparticle temperatures for various laser powers on a single spot of the nanoflower sample are shown. In the final iteration, the extrapolated temperature at zero laser power $T_{\mathrm{Au}}(P = 0)$ deviates by merely $\Delta T_{\mathrm{Au}} = -2.2\,\mathrm{mK}$ from the temperature of the environment $T_{\mathrm{env}} = 320\,\mathrm{K}$. Thus, ΔT_{Au} represents the temperature increase caused by laser heating of the hot spot.
To confirm the accuracy of this measurement, the sample holder was heated to specific, distinct temperatures. For optimal heat transfer between the sample and holder, they were connected by conductive silver paint. As the baseline $I_{\mathrm{Signal}}\left(\tilde{\nu}_{\mathrm{R}}, T_0\right)$ for all temperature measurements, the calibration spectrum with the lowest laser power $P = 0.37\,\mathrm{mW}$ was used. Its temperature $T_0 = T_{\mathrm{env}} + \Delta T_{\mathrm{Au}}$ was calculated to be 328.81 K. During the heating process, the sample holder expanded thermally. Thus, the sample moved transversely and out-of-focus with respect to the laser spot. Consequently, a new spot had to be used for every single external temperature, leading to challenges in the fitting process of the data. The plasmonic enhancement factor differs for each measurement and hence also between the reference measurement at T_0 and the measurements at other

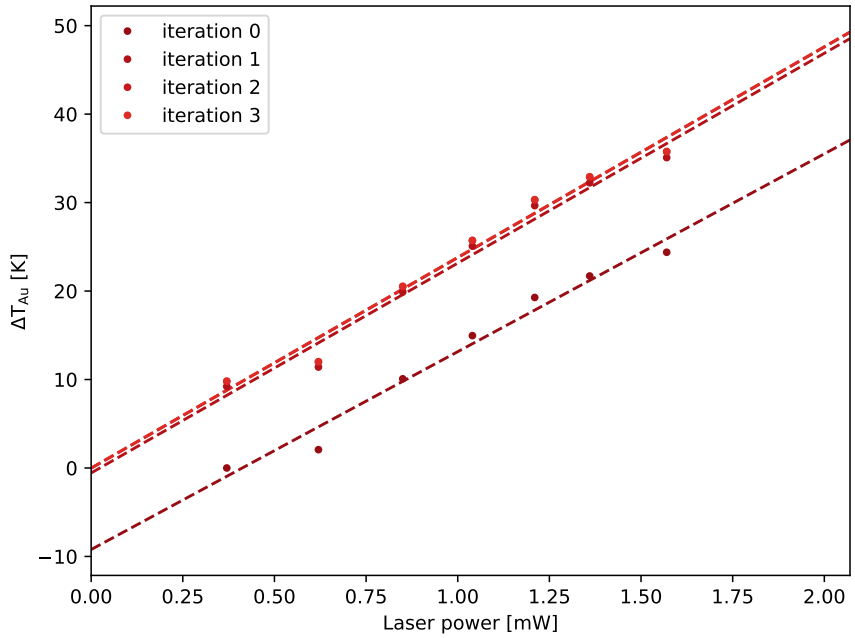

Figure 5.2: Temperature calibration process following Xie and Cahill [95] as described in section 2.4. Deviations ΔT_{Au} (dots) between the measured Temperature of the gold nanoflowers T_{Au} (calculated with Equation 2.17) and the temperature of the environment shown against the used laser power P. In iteration 0, T_0 is assumed to equal the environment. The temperatures are extrapolated linearly to zero laser power (dashed lines). Afterward, T_0 is shifted by the difference between $T_{\mathrm{Au}}(P = 0)$ and the external temperature and the next iteration starts until $T_{\mathrm{Au}}(P = 0)$ falls into $\pm 10\,\mathrm{mK}$ around the temperature of the environment in iteration 3.

temperatures. Therefore, another fitting parameter is introduced in Equation 5.2 that covers this difference in total intensity.

$$\frac{I_{\mathrm{Signal}}\left(\widetilde{\nu}_{\mathrm{R}}, T_{\mathrm{Au}}\right)}{I_{\mathrm{Signal}}\left(\widetilde{\nu}_{\mathrm{R}}, T_0\right)} = R_{\mathrm{SPR}} \frac{\mathrm{n}\left(\widetilde{\nu}_{\mathrm{R}}, T_{\mathrm{Au}}\right)}{\mathrm{n}\left(\widetilde{\nu}_{\mathrm{R}}, T_0\right)} \tag{5.1}$$

$$R_{\mathrm{SPR}} = \frac{I_{\mathrm{SPR}}\left(\mathrm{Spot}_{T_{\mathrm{Au}}}\right)}{I_{\mathrm{SPR}}\left(\mathrm{Spot}_{T_0}\right)} \tag{5.2}$$

This parameter R_{SPR} reflects the ratio of the signal strength I_{SPR} of both spots based on the different plasmonic enhancement at distinct hot spots. The plasmonic enhancement was approximated to be constant in the Raman shift for the conducted experiment. The incident light was at 633 nm for all measurements and the analyzed emission ranges between $\approx 594\,\mathrm{nm}$ and 615 nm. Within this small region, the LSPR exhibits relatively flat behavior for high excitation wavelengths, as shown in Figure 4.4a). Future research may take the detailed LSPR shape into account.
The logarithmized model employing the Boltzmann distributions for both temperatures T_{Au} and T_0 is linear in Raman shift $\widetilde{\nu}_R$ with the temperatures as slope and R_{SPR} as an

offset:

$$\ln\left(\frac{I_{\text{Signal}}\left(\widetilde{\nu}_{\text{R}}, T_{\text{Au}}\right)}{I_{\text{Signal}}\left(\widetilde{\nu}_{\text{R}}, T_{0}\right)}\right) = \ln\left(R_{\text{SPR}}\right) + \frac{hc}{k_B}\widetilde{\nu}_{\text{R}}\left(\frac{1}{T_{\text{Au}}} - \frac{1}{T_0}\right) \tag{5.3}$$

The necessity to introduce the plasmonic enhancement ratio R_{SPR} is demonstrated in Figure 5.3. In Figure 5.3a), SERS spectra are shown without any post-processing apart from normalization to their respective laser power and exposure time. An offset between each SERS spectrum is recognizable even in the Stokes part. The Stokes shifted response is barely influenced by the temperature [94] and therefore should look the same for equal plasmonic enhancements. The spectra are normalized to the fitted R_{SPR} as illustrated in Figure 5.3b). This normalization eliminates the offset in the Stokes region and clearly shows the different slopes of the anti-Stokes data. This is consistent with Figure 5.1. Wei et al. [91] use a similar approach to compare different hot spots. They exhibit equal molecule SERS peak strengths on different batches of nanoparticles and different substrates after normalizing the peaks to the strength of the elastic SERS peak. Hence, they claim that the elastic peak can be used as a measure of the plasmonic enhancement [91]. Since R_{SPR} is the offset in Equation 5.3, it also contains information about the SERS signal at $\widetilde{\nu}_{\text{R}} = 0$ and thus the elastic Rayleigh peak. With this normalization of the SERS data, different spots on the clustered gold nanoflower sample can be compared.

Finally, the results of the temperature measurements are shown in Figure 5.4. Kinetic SERS spectra were measured for a total of 15 distinct spots with three spots for each of the five temperatures T_{env}. The spectra used for this were measured in the first seconds of irradiation and are the ones shown in Figure 5.3 and Figure 5.1. Laser heating of small nanostructures reaches an equilibrium after tens of nanoseconds [53]. Afterward, another effect raised the temperature as further described in section 5.2. Therefore, only the first second was taken into account for the comparison of the heated environment. The mean temperatures T_{Au} are illustrated as red dots in Figure 5.4a) against the temperature of the external heater T_{env}. The error bars are the associated standard errors of the mean. Additionally, the plasmonic enhancement ratio R_{SPR} is shown in Figure 5.4b) for every distinct measured spot on the sample. They seem to form bunches for each temperature indicating a correlation with T_{env}. This may be derived from the temperature dependence of the LSPR. The LSPR absorption peak of metal nanoparticles shifts and broadens and the near-field enhancement shrinks with rising temperature [29, 44]. Also, the necessity of adjusting the focus settings for every T_{env}, may have to be taken into account. Hence, in this series of measurements R_{SPR} might contain more information than just the plasmonic enhancement. A linear fit is depicted as a red dashed line with a fixed slope of one as T_{Au} should match T_{env} apart from an offset due to laser heating. Thus, the second parameter $T_{\text{Au}}(T_{env} = 0) = 10.96\,\text{K}$ represents the average deviation of T_{Au} from the environment. The calibration function, measured at another spot, predicts a temperature increase of 11.43 K at the used laser power 0.48 mW. With a deviation of only 4.1% the raised temperature can be attributed to plasmonic heating. Consequently, the measured temperatures align well with the sum of the environmental temperature and laser-induced heating, validating the anti-Stokes signal of SERS spectra as a reliable measure of the temperature of the irradiated nanoparticles. As a result, the gold nanoflowers are excellent absolute thermometers of the environment at the nanoscale.

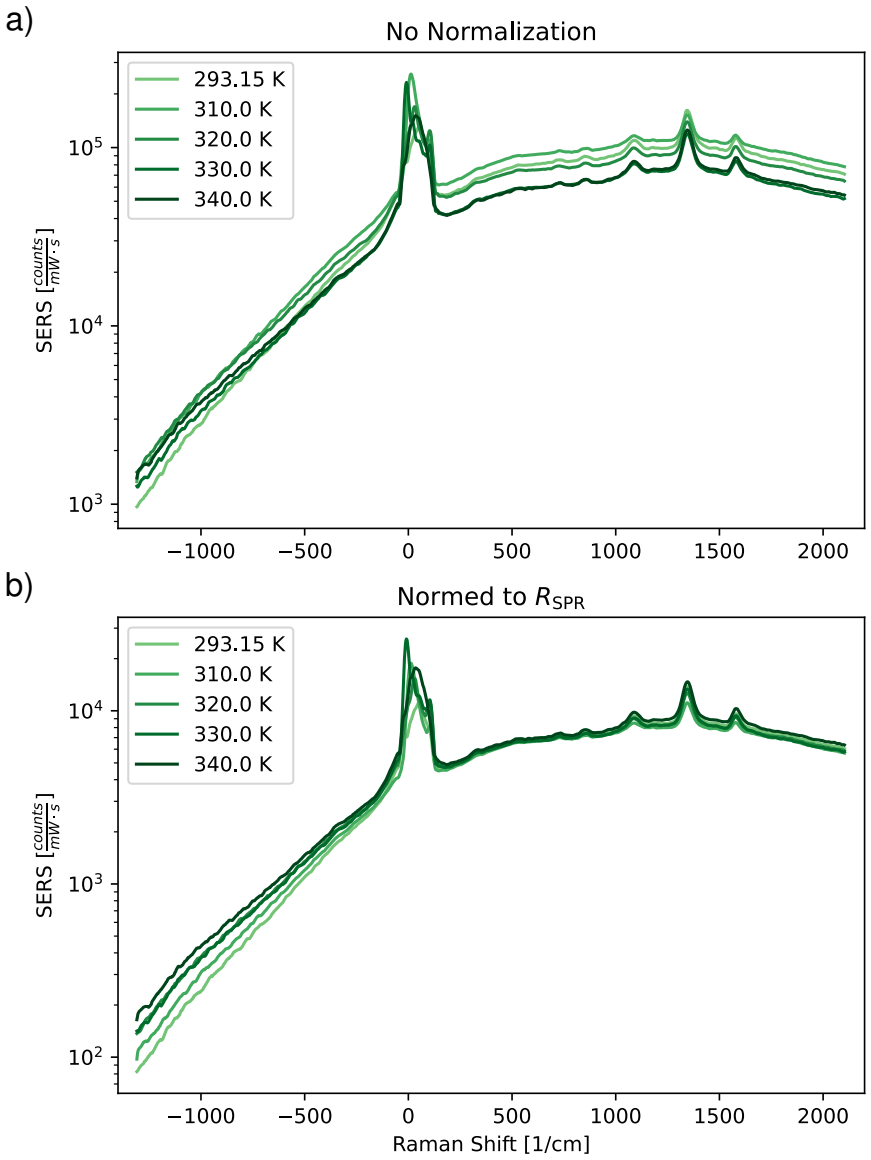

Figure 5.3: SERS spectra of the Au Nanoflowers and 4-NTP at different environment temperatures. The graphs in a) are normalized only to their respective laser power and exposure time. In b), they are additionally scaled to their corresponding R_{SPR}, determined in the fitting process.

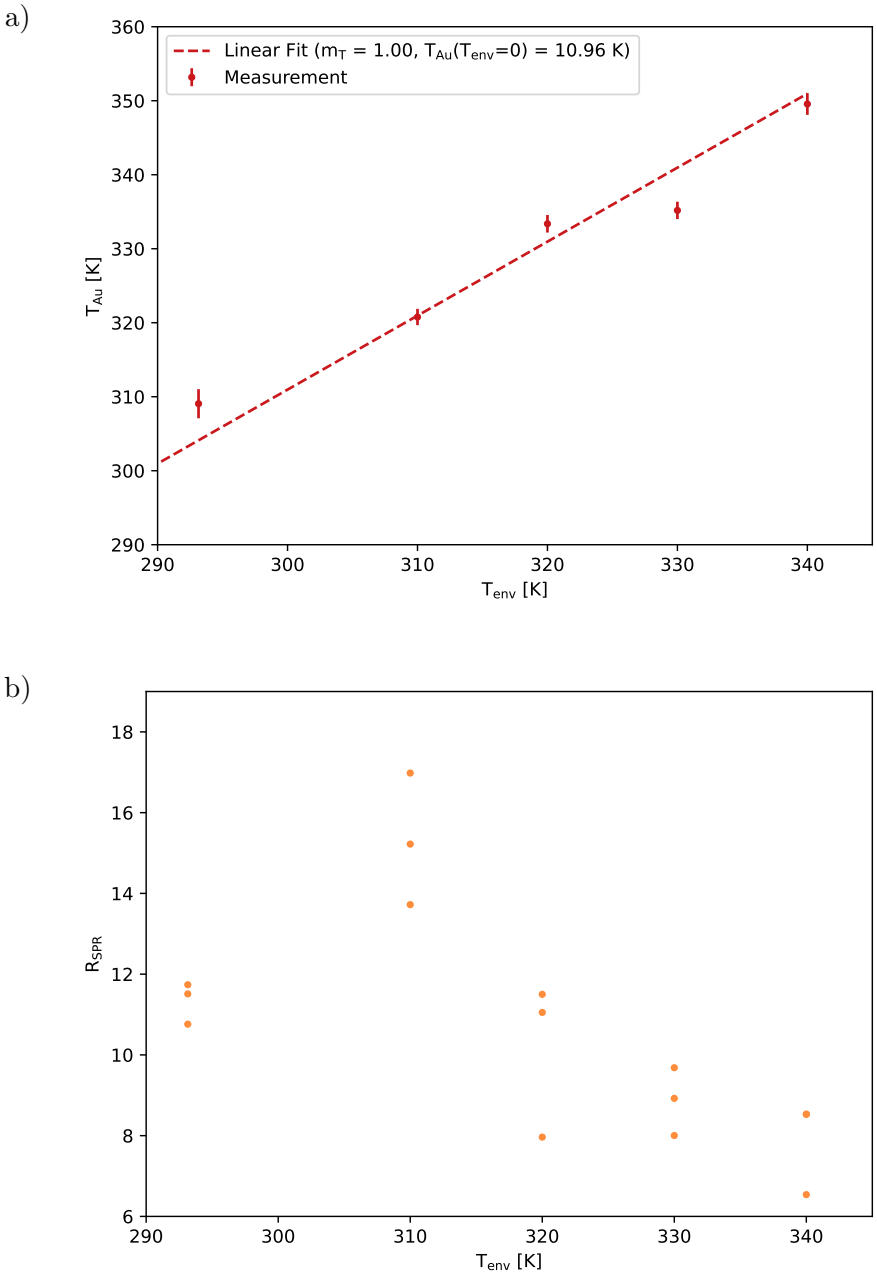

Figure 5.4: a) Anti-Stokes temperature measurement of the Au nanoflowers T_{Au} dependent on the environmental temperature T_{env} with the standard error of the mean as the error bar. The corresponding linear fit (dashed line) has a fixed slope of $m_{\mathrm{T}} = 1$. Hence, $T_{\mathrm{Au}}(T_{env} = 0) = 10.96\,\mathrm{K}$ represents the average deviation of T_{Au} from the environment. b) Plasmonic enhancement ratio R_{SPR} is shown for every distinct measured spot on the sample (three at each temperature). R_{SPR} seems to correlate with T_{env}, as the measured values form bunches.

5.2 Temperature Modulation With Time

Knowledge about temperature changes in SERS is crucial for understanding the influence of nanoparticle excitation on reaction mechanisms. Therefore, the temporal evolution of the nanoparticle temperature was measured in a second timescale. While the anti-Stokes temperatures at the start of the measurement equal the environment of the nanoparticles plus laser heating, as demonstrated in the preceding section 5.1, the temperature subsequently increased further during the next hundred seconds.

This behavior is shown in Figure 5.5. The nanoparticle temperature is increasing an-

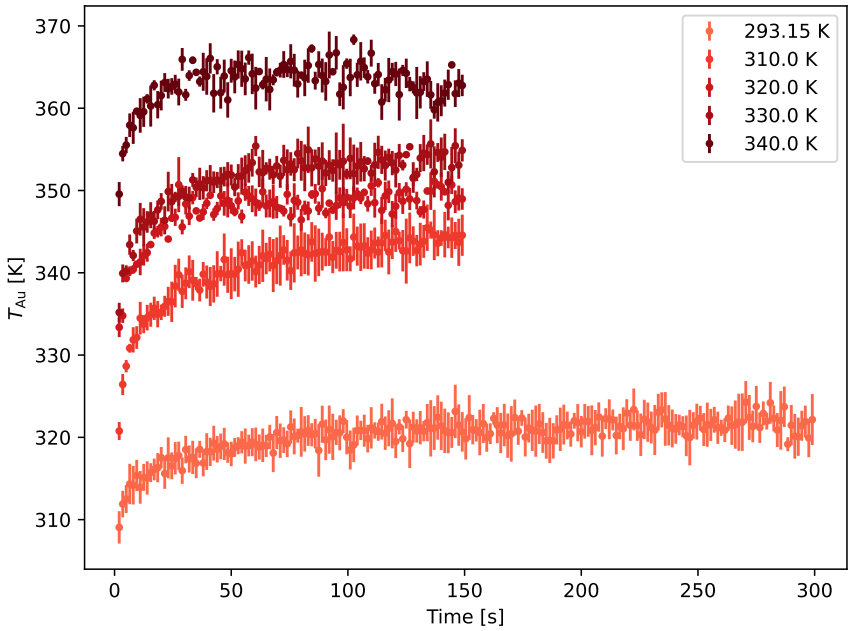

Figure 5.5: Anti-Stokes temperatures of the Au nanoflowers T_{Au} over time for different environment temperatures as indicated by the legend. Error bars show the standard error of the mean of all three spots measured at each T_{env}. While T_{Au} matches T_{env} in the first second of irradiation, it raises subsequently.

other $\approx 20\,\mathrm{K}$ and saturates after around 100 s to 150 s. Keblinski et al. [58] assign such heating over several hundreds of seconds to collective heating of an ensemble of nanoparticles. This assumes that the volume the temperature is conducted from is smaller than the laser-heated volume. The here conducted measurements rely on the anti-Stokes emitted light from the sample reaching the spectrometer. A significant portion of the light may be lost in the microscope path. Not the loss of intensity due to filters is relevant, but rather the loss of spatial information, for example, due to pin holes and slits, as one is installed in the spectrometer. If collective heating causes this elevation of temperature, future nanoscale temperature measurements either have to employ a redesigned beam path enabling an optimized spatial light acquisition or longer equilibration times have to be considered.

Additionally, the enhancement ratio R_{SPR} is decreasing with time as depicted in Fig-

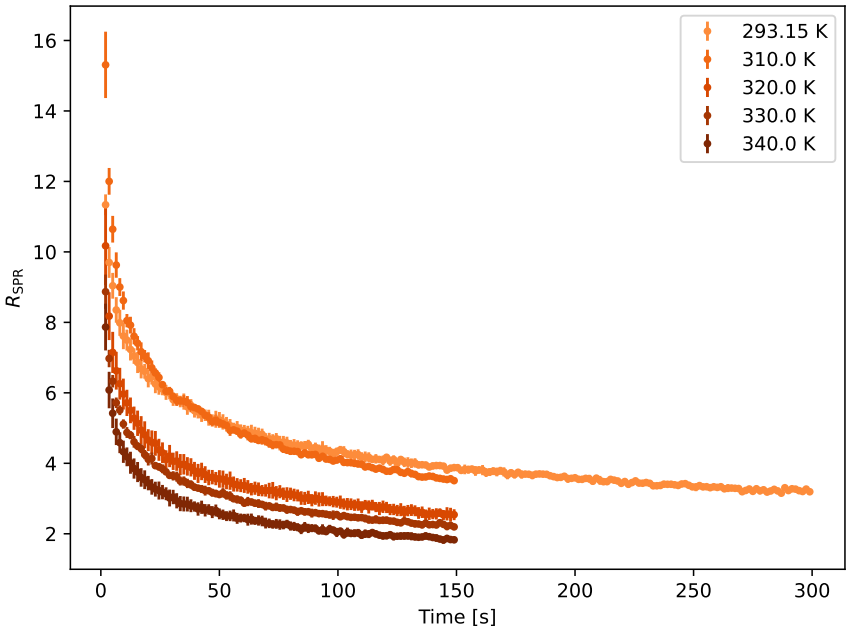

Figure 5.6: Plasmonic enhancement ratio R_{SPR} over time for different environment temperatures as indicated by the legend. Error bars show the standard error of the mean of all three spots measured at each T_{env}. R_{SPR} shrinks over time, indicating an overall decay of the SERS background.

ure 5.6. A change in R_{SPR} equals a change in the overall SERS signal strength, as discussed in the previous section in Figure 5.3. In Figure 5.7, R_{SPR} and the integrated SERS signal are correlated to each other. They demonstrate a strong positive correlation for all temperatures and hot spots. The average Pearson correlation coefficient over all measurements is (0.990 ± 0.008). I. e., The surface-enhanced Raman background of the gold nanoflowers decayed to a certain level while irradiated and R_{SPR} is a great quantity for the overall signal strength. The correlation of T_{Au} and R_{SPR} is shown in Figure 5.8. These quantities have a negative correlation with a Pearson coefficient of (-0.794 ± 0.037), but especially at later times or low values of R_{SPR} the temperature has strong noise. It can not be excluded that other properties are involved in this process. Nevertheless, there has to be a process during the irradiation of the nanoflowers that changes both the nanoparticle temperature and the overall background of the SERS signal. In particular, the decay of the SERS background was observed on separate nanoflower samples and is discussed from the aspects of different properties in the next chapter.

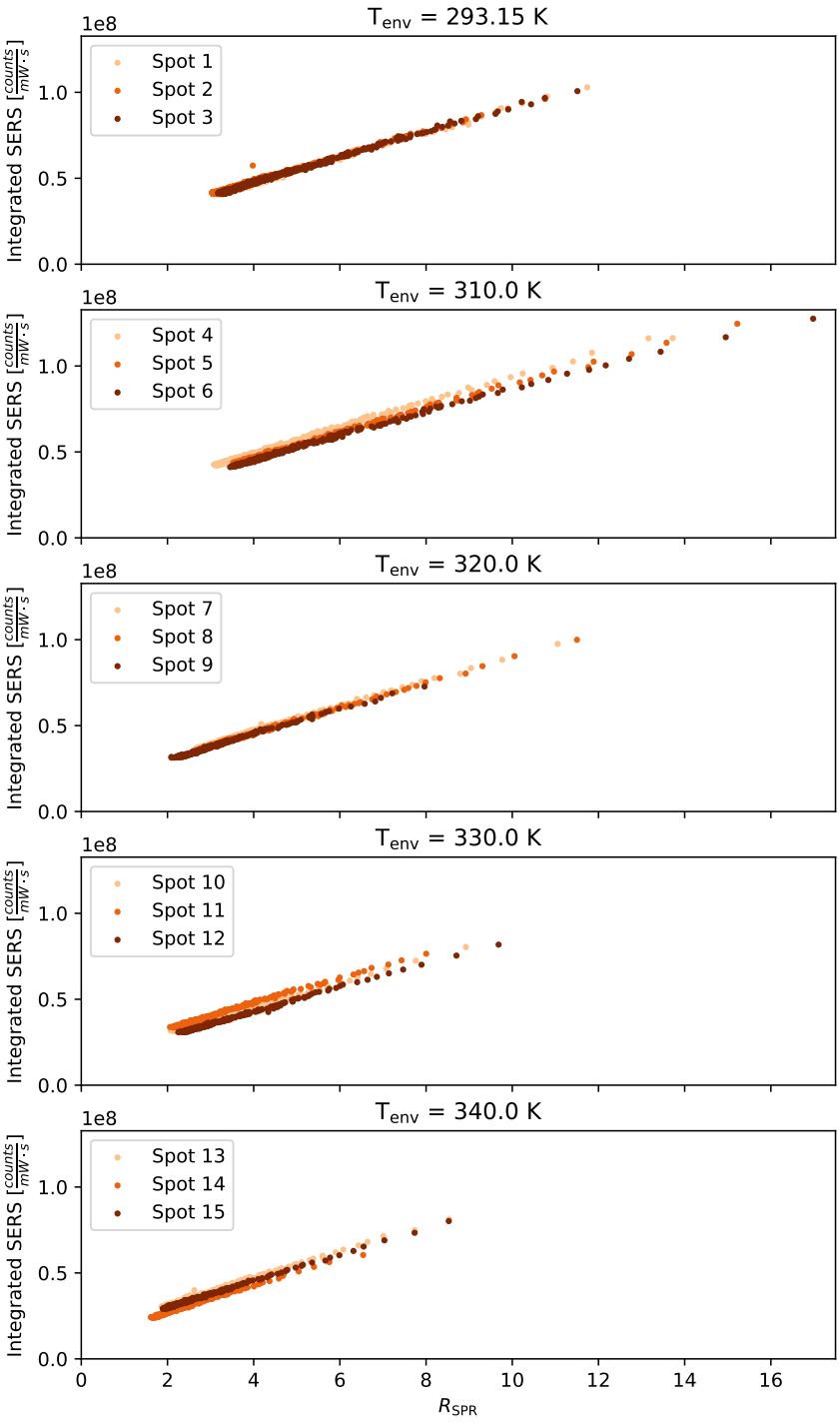

Figure 5.7: Correlation of the integrated SERS signal and the enhancement ratio R_{SPR} for all hot spots assigned to the respective temperature of their environment. The different hot spots for each temperature are marked by different colors, as displayed by the legend.

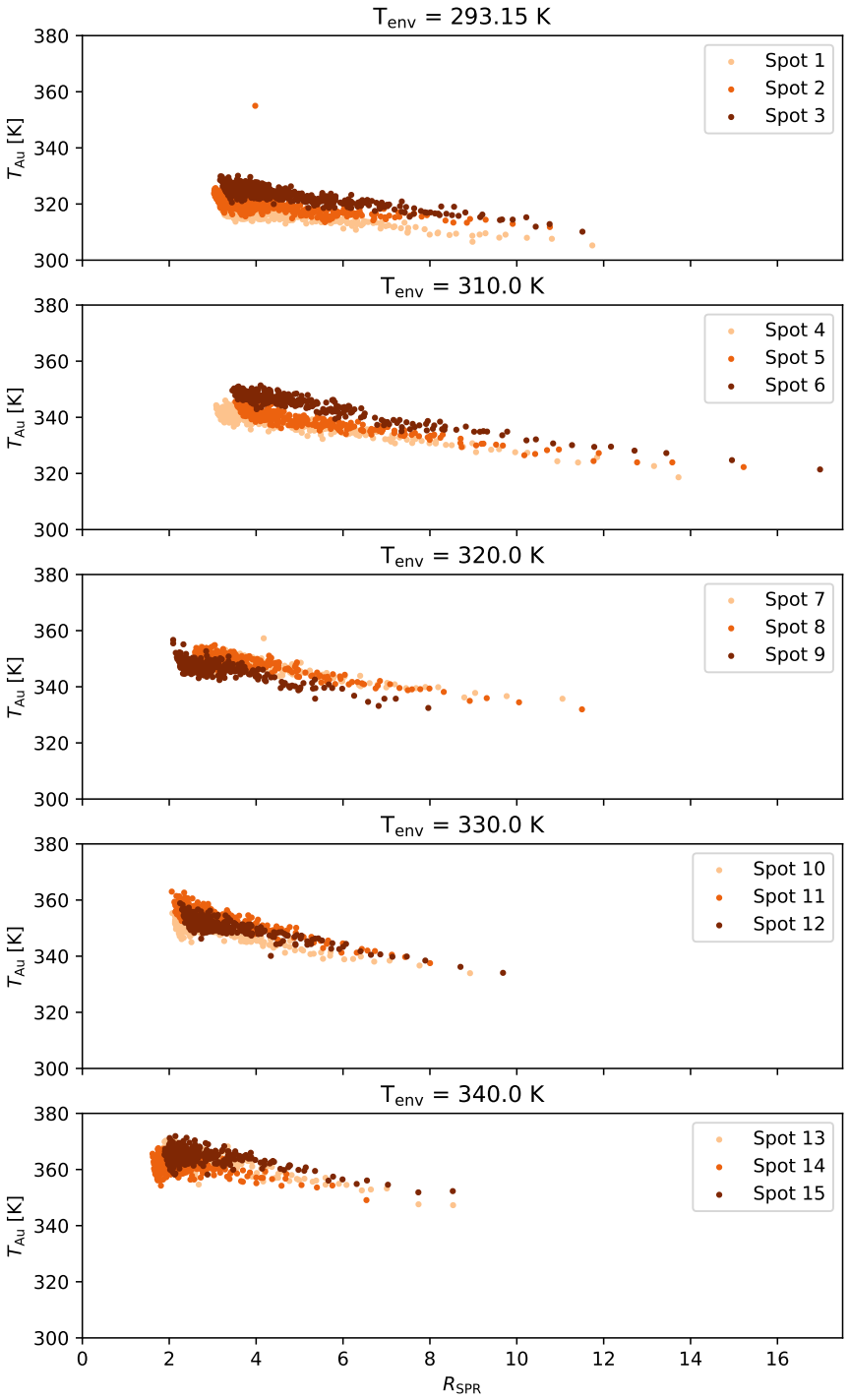

Figure 5.8: Correlation of the nanoparticle temperature T_{Au} and the ratio parameter of the plasmonic enhancement R_{SPR} for all hot spots assigned to their respective temperature of the environment. The different hot spots for each temperature are marked by different colors, as displayed by the legend.

Chapter 6

Decay of Metal Nanoparticle Response

In several kinetic SERS experiments, a decay of the background signal (BGND) on the timescale of a few minutes was observed. Multiple SERS spectra are depicted over the time of irradiation in Figure 6.1 showing this decay.

In SERS measurements with a high background, for example, measurements on clus-

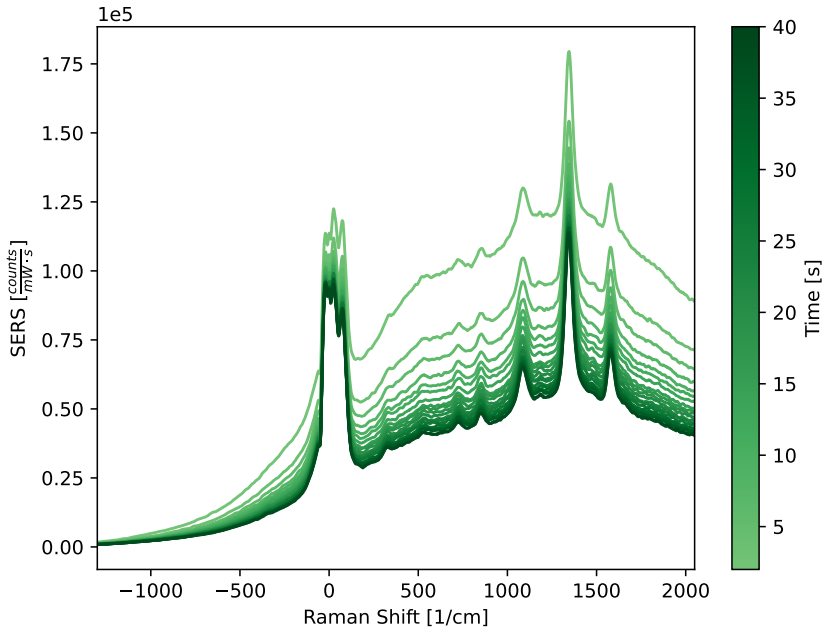

Figure 6.1: SERS spectra of Au nanoflowers coated with 4-NTP after different times of irradiation as indicated by the color bar.

tered, high-faceted nanoflowers, this decrease of the BGND signal can strongly outweigh changes in the Raman peaks of the adsorbed molecules. Hence, it must be taken into account for the analysis of photocatalytic reactions, and the determination of the source of the BGND decay is most relevant. Since the SERS BGND is attributed to light-matter interactions in the nanoparticles, various explanations are possible. Photoluminescence

(or ERS) originates from the recombination of excited electrons and holes in the metal band structure. If these electrons relax non-radiatively or are transferred into another object this would hinder light emission and decrease the PL signal. Electron-phonon scattering equilibrates on a picosecond timescale [16, 46] and thus does not explain such a slow decay. On the other hand, electron transfer channels from the nanoparticles in this experiment can involve the substrate, the air, or attached molecules. In general, the number of electrons in the nanoparticle influences the plasmonic enhancement of scattering and apsorption [98]. Also, changes in the structure of the nanoparticles could modify the background. Heat is reported to change the structure of gold nanoparticles for temperatures above at least 400 K due to melting or shaping of the surface [21, 52, 71, 80]. In the experiments presented in this thesis, the temperature of the nanoflowers due to external and laser heating does not exceed 370 K as demonstrated in chapter 5 and therefore is not likely to alter the shape of the nanoparticles, but there is also another reason to rule out this explanation outlined in the next section.

6.1 Recovery of the Background

In measurements using the same hot spots, it was discovered that the background regenerates between irradiations. The BGND decays of two different hot spots are depicted in Figure 6.2. Vibrational peaks were excluded from the data processing. The average

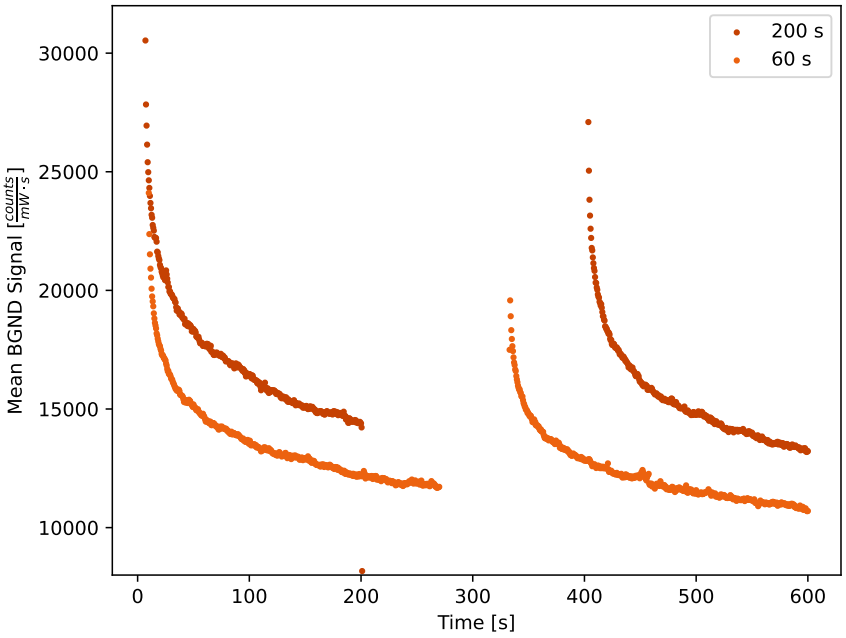

Figure 6.2: Background (BGND) decay of gold nanoflowers on Si measured nine months before Figure 6.3. Two different hot spots were recorded and marked with different colors. During the measurement, the laser was shut down for 200 s and 60 s, respectively, as indicated by the legend. After the time in the dark the signal recovered for a significant portion of the original strength and started to decay again.

of the remaining BGND spectrum was determined dependent on the time. During the recording, the laser was shut down for 200 s and 60 s, respectively. Afterward, the signal recovered in the dark and started to decay again. It reaches signal strengths close to the original value of the Raman background. This behavior excludes the melting of nanoparticles from the list of possible explanations since such restructuring of the surface would be irreversible.
It has to be mentioned, that the ability to recover the background in the dark diminished with the age of the nanoflower sample. After nine months, while still regenerating, the background needs much longer time in the dark as shown in Figure 6.3. After a first measurement of a hot spot, marked by *Start* in the legend, 37 min in the dark were not enough to recover the nanoparticle response significantly. However, after an additional 18.83 h regeneration is visible. Nevertheless, an offset between the initial and final measurement persists. Due to technical issues, the last measurement was conducted with less laser power (0.13 mW) than the first measurement (0.22 mW), explaining this offset.

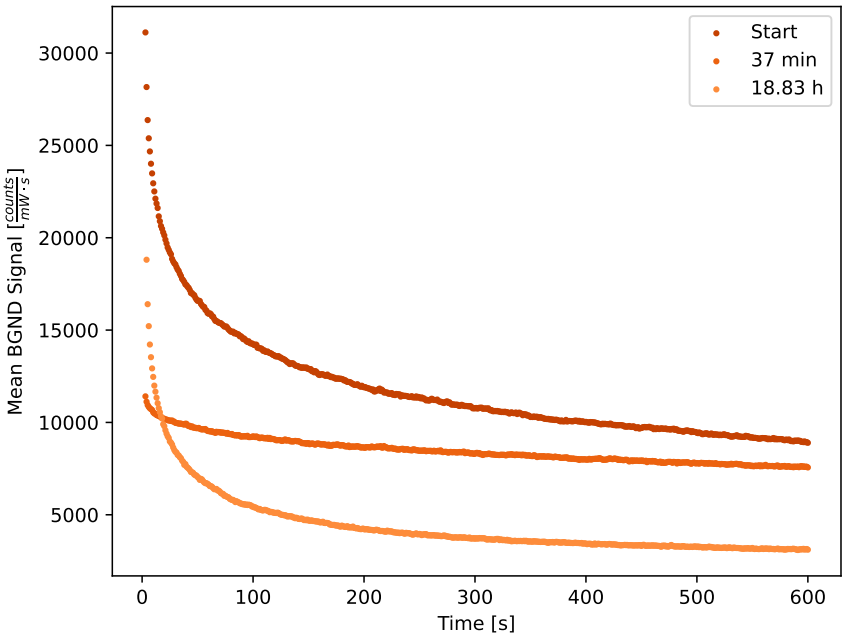

Figure 6.3: Background (BGND) decay of gold nanoflowers on Si measured nine months after Figure 6.2. Right after the first irradiation (Start), the laser was shut down for 37 min and then again for 18.83 h. After the first pause, almost no recovery was determined despite Figure 6.2 showing fast regeneration. Only the long time in the dark accomplishes good recovery.

6.2 Decay Rates and Spectral Behavior

For the following investigations, it is required to quantify the background decay. Therefore, different fitting models were tested. While an exponential function does not de-

scribe the decay data sufficiently, as shown in Figure 6.4, bi-exponential and stretched exponential models fit much better. At the time being, there are marginal reasons to justify a bi-exponential decay model. It would assume exactly two decay channels with two separate decay rates. Of course, there may be multiple channels if, for example, the decay is due to charge transfers to the substrate, adsorbed molecules, etc. Right now there are no indications of the number of decay channels. Also, the response of different nanoparticles in the illuminated cluster may decay at slightly different rates. The stretched exponential model or Kohlrausch-William-Watts (KWW) function provides a form where the sum of several exponential decay modes is described by a distribution exponent β [57, 64]. Therefore, the mean decay rate $\langle k_{\mathrm{BGND}} \rangle$ can be determined without the need to handle multiple decay processes. Hence, the KWW model is used to quantify the decay for now. The mean decay rate $\langle k_{\mathrm{BGND}} \rangle$ of the background signal $I_{\mathrm{BGND}}(t)$ is given by the mean relaxation time $\langle \tau \rangle$ using the relaxation time τ, the stretching exponent β and the Gamma-function Γ [57].

$$I_{\mathrm{BGND}}(t) = I_0 \exp\left[-\frac{t - t_0}{\tau}\right]^{\beta} + I_{\infty} \tag{6.1}$$

$$\langle \tau \rangle = \frac{\tau}{\beta} \Gamma\left(\frac{1}{\beta}\right) \tag{6.2}$$

$$\langle k_{\mathrm{BGND}} \rangle = \frac{1}{\langle \tau \rangle} \tag{6.3}$$

Here, t_0 is the starting time. I_0 and I_{∞} are the respective start and end values of the BGND.

Each measurement presented in this chapter is either a time-dependent record of SERS spectra or photoluminescence spectra. The calculation of the decay rates can therefore be determined spectrally resolved. Especially, the difference between Stokes and anti-Stokes regions is of interest due to their different origins. This is done in Figure 6.5 for the decay processes also depicted in Figure 6.3. As expected, the decay rates after 37 min without illumination are minimal since almost no regeneration was possible in this short time span. Interestingly, the decay rates after 18.83 h are generally higher than at the start despite the fact, that the sample is irradiated with less laser power in the final measurement. How the laser intensity affects the decay rate is discussed in section 6.3. For now, we look at the spectral differences of the decay rates. The calculations are restricted to regions without vibrational Raman peaks determined by the attached molecules. Their behavior might be influenced by molecular effects such as photoreactions or the detachment of molecules rather than by the intensity of the background signal. In all three measurements, a maximum of the decay rates around the Rayleigh wavelength is apparent, decreasing on both sides. In the anti-Stokes region, $\langle k_{\mathrm{BGND}} \rangle$ shrinks faster than on the Stokes side with increasing distance to the Rayleigh peak.

If the number of available electrons drives the background decay and the decay channels transfer electrons regardless of the emission frequency, the mean decay rates represent a distribution of the electrons involved in the emission processes. As mentioned earlier, the nanoparticle response relies on the distribution of electrons. Hence, at high energy shifts lower decay rates correlate with lower response signals. The AS signal is far more

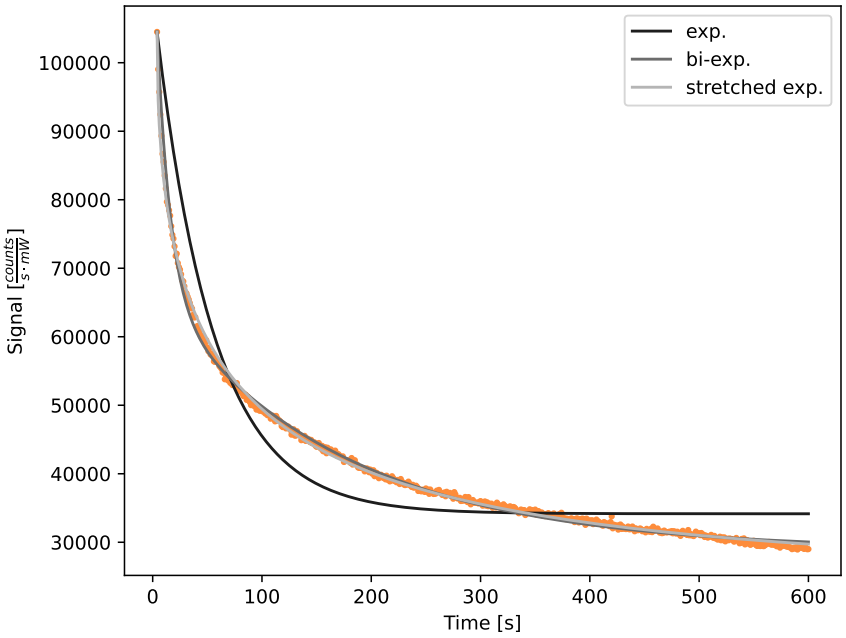

Figure 6.4: Exponential, bi-exponential, and stretched exponential fits, as indicated by the legend, for an underlying SERS BGND decay process (orange). While the exponential function is far off, the rest provides good results.

dependent on the distribution of electrons and holes than the Stokes region. Thus, the slope of the decay rates is steeper on the anti-Stokes side. On the other hand, at low Raman shifts up to $1400\,\mathrm{cm}^{-1}$ on the Stokes side, the SERS signal is increasing with rising Raman shift while the decay rates already drop. The SERS background depends on the joint density of states of the excited electron and available hole states [79, 94]. In contrast, the hole states are irrelevant to the decay rates as the electron transfer occurred before emission. This can explain the deviation of both signals.

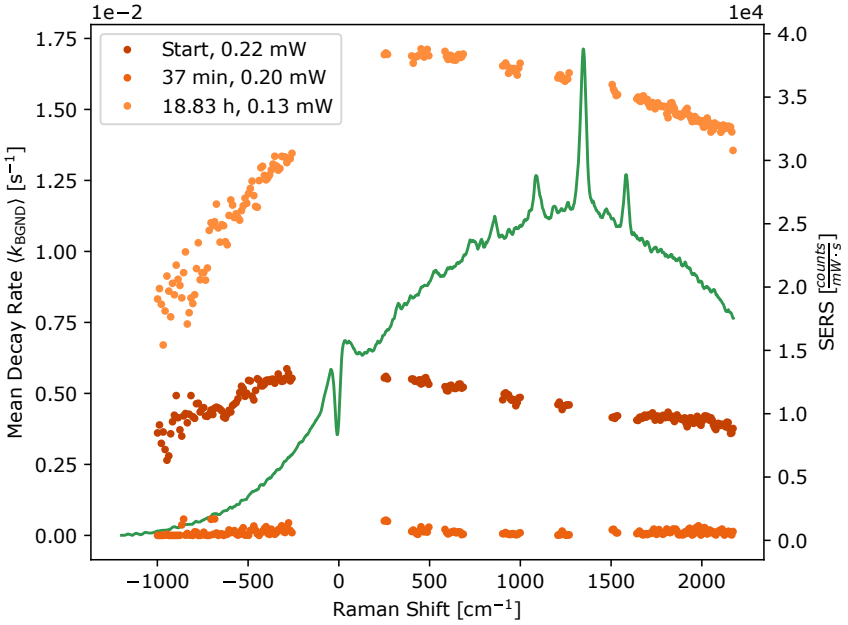

Figure 6.5: Spectrally resolved $\langle k_{\mathrm{BGND}} \rangle$ of the SERS BGND decay depicted in Figure 6.3. Decay rates of the final measurement are higher than in the initial process despite using less laser power, as indicated by the legend. $\langle k_{\mathrm{BGND}} \rangle$ peaks at the Rayleigh wavelength and decreases towards both sides.

6.3 Incident Light

A series of measurements with different laser intensities confirms the minor decrease of the mean decay rates to higher Raman shifts, as presented in Figure 6.6a). Only the data received at the highest laser power 4.16 mW deviates from this trend and rises in a fluctuating manner above 1000 cm^{-1}. If this outlier presents a feature due to high intensities with maybe high electron temperatures, remains to be determined.

Overall, the mean of $\langle k_{\mathrm{BGND}} \rangle$ increases with laser power. Figure 6.6b) depicts, that the decay rate increases nonlinear, especially for low power. In the previous section, the decay rates after signal recovery were higher than at the start (compare Figure 6.5), despite the lower laser power. This is contrary to the observations of this section. Hence, the regeneration of the nanoparticle background should be reviewed again.
In addition, the BGND decay is observed in the photoluminescence experiments. Kinetic measurements were recorded for different excitation wavelengths. The results are presented in Figure 6.7. Even for the spectra taken with equal laser power at 171 µW, there is no clear trend of the decay rates recognizable with the different excitation wavelengths. However, most excitations follow the drop to wavelengths further away from the laser peak as in the SERS spectra. Only the lowest excitation wavelength seems to increase $\langle k_{\mathrm{BGND}} \rangle$. Following the charge carrier theory from above, this indicates more electrons are involved in high wavelength emissions. Since this phenomenon only appears at the lowest excitation wavelength, maybe the domination of interband transitions plays a

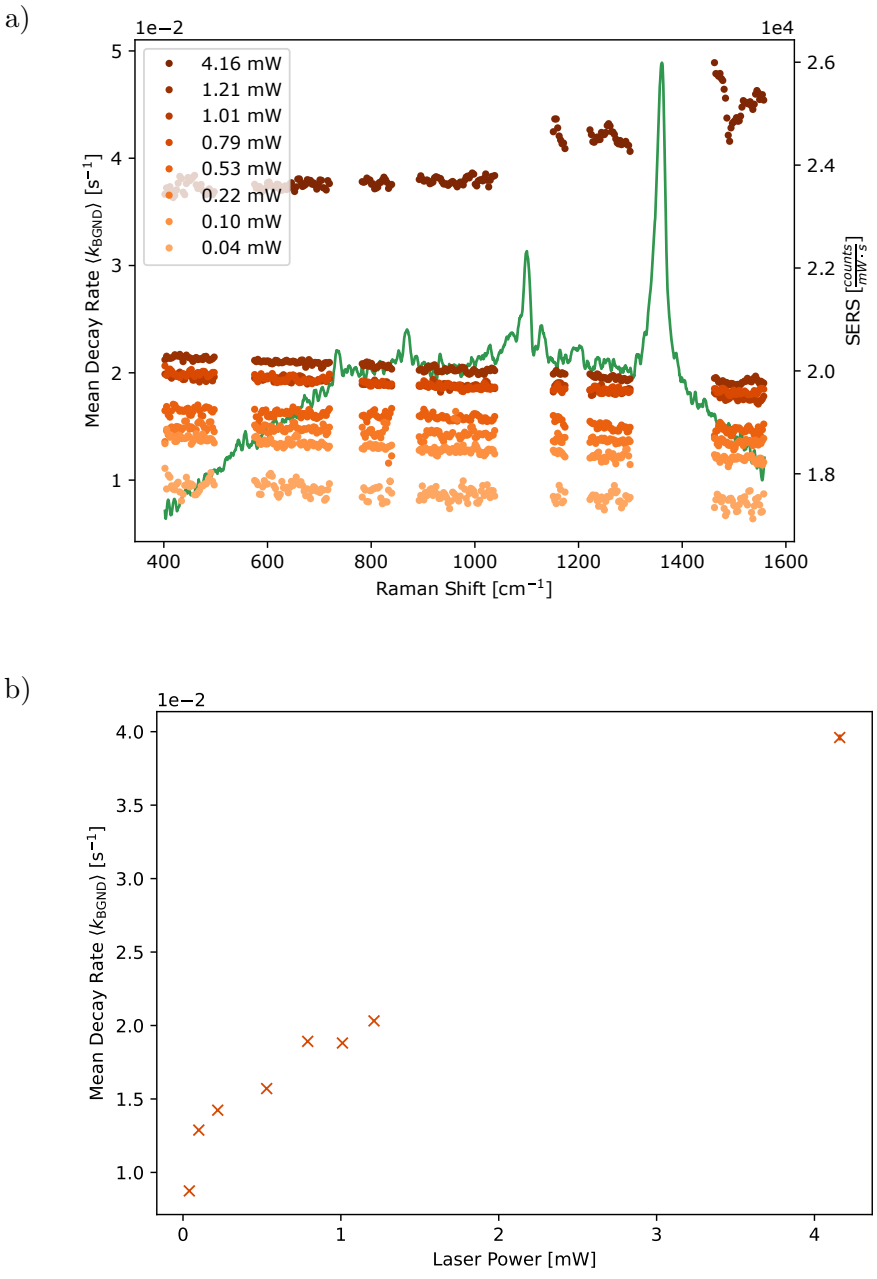

Figure 6.6: Mean decay rates $\langle k_{\mathrm{BGND}} \rangle$ of SERS spectra at different laser powers. a) Spectral resolved decay rates (orange) at their respective laser powers with a representative SERS spectrum (green). b) Average $\langle k_{\mathrm{BGND}} \rangle$ with their standard error of the mean as error bars. The error bars are barely visible due to their average value of $4.6 \times 10^{-5}\,\mathrm{s}^{-1}$. While the spectral dependence of the mean decay rates at the highest laser power deviates from the other measurements, the average $\langle k_{\mathrm{BGND}} \rangle$ monotonously increases with laser power.

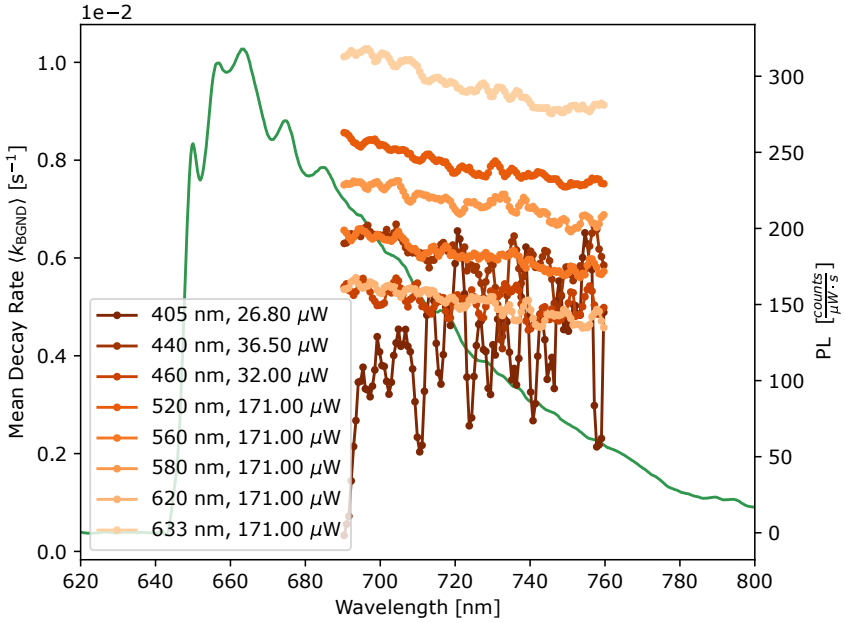

Figure 6.7: Mean decay rates $\langle k_{\mathrm{BGND}} \rangle$ of the photoluminescence (PL) of Au nanoflowers on Si at different excitation wavelengths (orange) and laser powers, as noted in the legend. A representative PL spectrum is shown in green. The measurement with the lowest excitation wavelength (405 nm) deviates from the monotonous decrease with rising emission wavelength. Also, there is no clear trend of the integrated $\langle k_{\mathrm{BGND}} \rangle$ with excitation wavelength even at the same laser power.

role in this observation. Thus, interband excited electrons would be mostly involved in a mechanism causing high wavelength emissions. A connection to the anomalous behavior of the PLE below 440 nm(compare Figure 4.5) can only be suspected at the moment. Nevertheless, a measurement of the Au nanoflowers on glass at $\lambda_{\mathrm{exc}} = 410\,\mathrm{nm}$ confirms the increase of $\langle k_{\mathrm{BGND}} \rangle$ with emission wavelength at high energy excitations, as shown in Figure 6.8. Hence, the range between 405 nm and 440 nm should be reviewed again with decay rate measurements under controlled conditions.

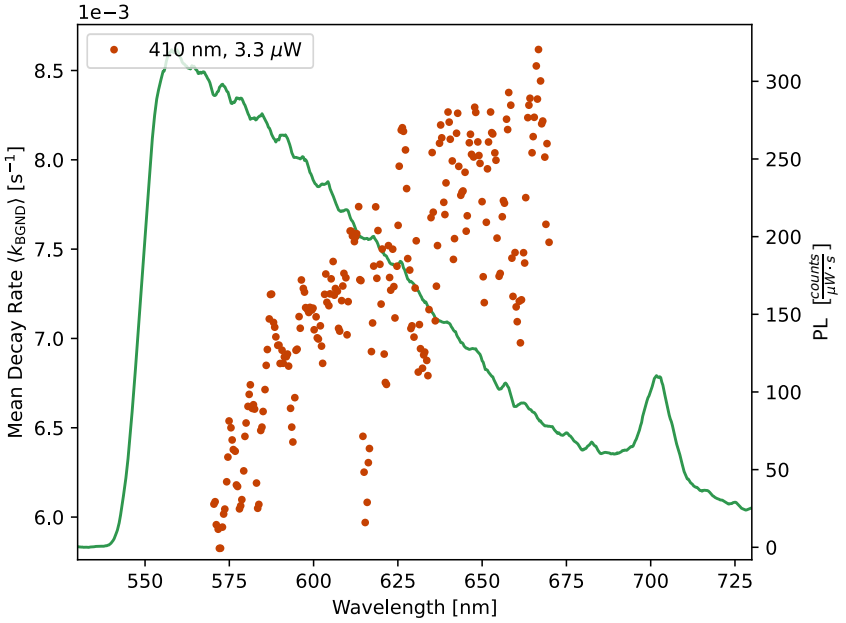

Figure 6.8: Mean decay rates $\langle k_{\mathrm{BGND}} \rangle$ of the photoluminescence (PL) of Au nanoflowers on glass excited at 410 nm (orange). A representative PL spectrum is shown in green. The increasing decay rates with longer wavelengths support the observations at low-wavelength excitation in Figure 6.7.

6.4 Environment

Since possible charge transfers are dependent on substances and their properties in close proximity to the nanoparticles, changes in the environment must be taken into account. This section contains first pieces of evidence of the influence of temperature, the chemical composition of the atmosphere, the substrate, and the adsorbed molecules. While further investigations are required for each of these topics ideas for future experiments are provided.

At first, the kinetic data introduced in section 5.2 is used to determine the temperature dependence of the BGND decay. Figure 6.9 shows the mean decay rates for all fifteen hot spots. In Figure 6.9a), the rates are averaged over the three spots for each temperature and presented against the Raman shift, while in Figure 6.9b) $\langle k_{\mathrm{BGND}} \rangle$ is averaged over the Stokes region and plotted against the externally controlled temperature for each spot. Generally, the decay is faster with higher temperatures. Since the temperature of the nanoflowers is increasing while irradiated, as demonstrated in Figure 5.5, it is of interest if both temperature and BGND changes occur on the same timescale. Therefore, the calculated anti-Stokes temperatures T_{Au} and plasmonic enhancement ratios R_{SPR} were modeled the same way as the background. The mean decay rates $\langle k_{T_{\mathrm{Au}}} \rangle$ and $\langle k_{R_{\mathrm{SPR}}} \rangle$ in Figure 6.10a) and b) correspond to the fits depicted in Figure A.4a) and b), respectively, that contain the data from Figure 5.5 and Figure 5.6. The decay of R_{SPR} matches the decay of the SERS background as already discussed in section 5.2.

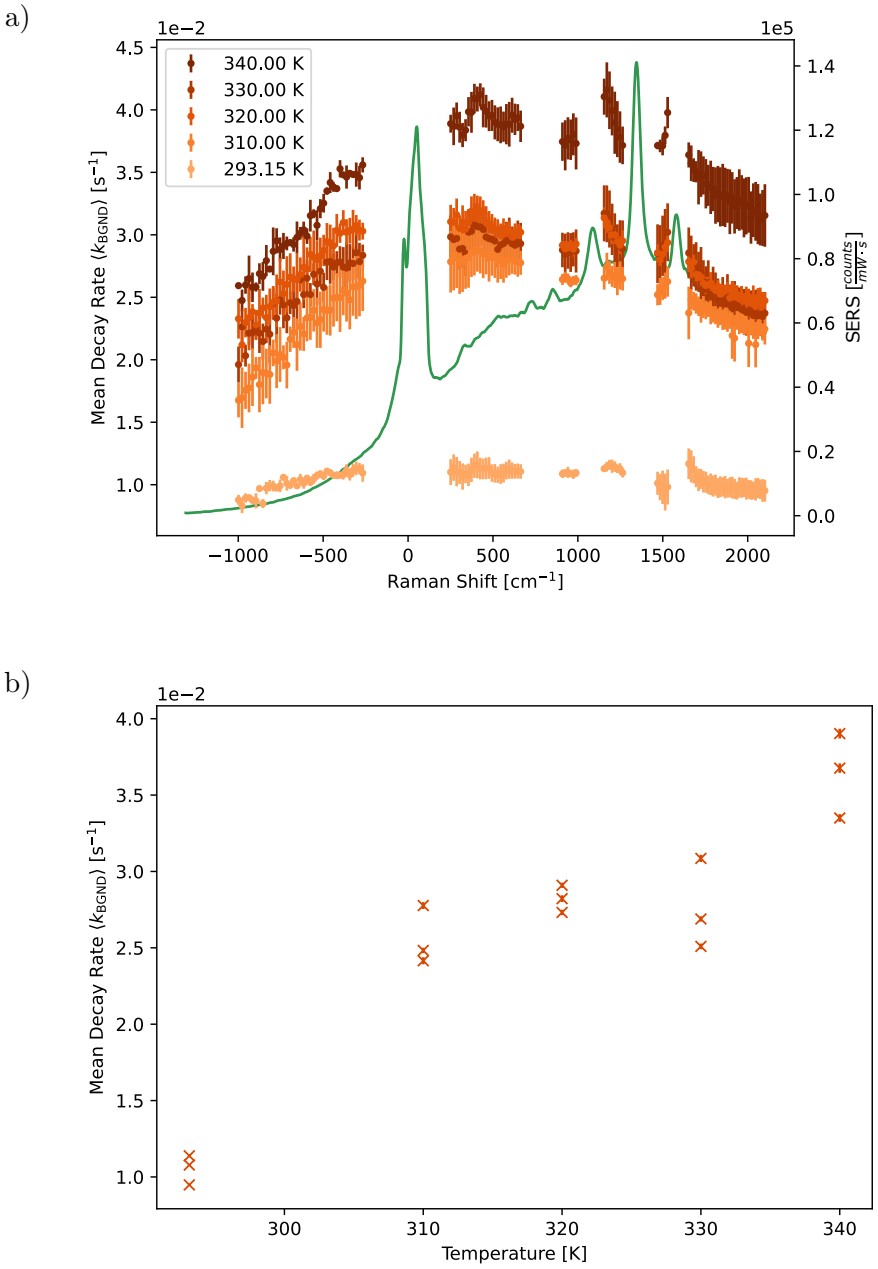

Figure 6.9: Mean decay rates $\langle k_{\mathrm{BGND}} \rangle$ of SERS spectra presented in section 5.2 at different environmental temperatures. a) Spectral resolved mean decay rates (orange) averaged for all measured hot spots at their respective temperatures, as the legend indicates. The error bars are the standard error of the mean between the different spots. A representative SERS spectrum is depicted in green. b) Average $\langle k_{\mathrm{BGND}} \rangle$ for each single hot spot vs. their temperature. These values only account for the Stokes region to compensate for the decrease on the AS side. Error bars indicate the standard error of the mean from the different Raman-shifted emissions.

The temperatures, on the other hand, not only increase faster than the BGND decays ($\langle k_{\mathrm{BGND}} \rangle \approx 0.01\,\mathrm{s}^{-1}$ to $0.04\,\mathrm{s}^{-1}$; $\langle k_{T_{\mathrm{Au}}} \rangle \approx 0.02\,\mathrm{s}^{-1}$ to $0.15\,\mathrm{s}^{-1}$), the dependence on the external temperature does not appear to saturate for higher temperatures. Consequently, the background decay is at least not entirely determined by the temperature changes, consistent with their correlation in Figure 5.8.

All experiments so far were performed in air. It is suspected that more reactive components like oxygen or water molecules interact with the nanoflowers to exchange electrons and holes with the nanoparticles. To minimize the influence of surrounding molecules, the sample was placed in a continuously flowing nitrogen atmosphere at 60 °C. As illustrated in Figure 6.11, the decay is following the same observations as before. The decay rate $\langle k_{\mathrm{BGND}} \rangle$ is about half as much as in air with similar laser power in Figure 6.6 despite the heightened temperature. However, the role of different plasmonic enhancements can not be ignored. Hence, for now, it is suspected that components in the air around the nanoparticles do not dominate the decay. To determine the influence of the air SERS measurements have to be conducted at the same hot spots in different atmospheres. Also, Raman Spectra could be measured with e. g. a drop of Ethanol on top of the sample. Ethanol is a known hole scavenger and could stop the decrease of the total electron number in the nanoflowers. If this leads to a vanishing decay or even an increase in the Raman background, this could prove the connection between the nanoparticle response and the number of electrons.

The same theory was also tested for different adsorbed molecules and substrates. A sample with 4-ATP (4-Aminothiophenol) exchanging 4-NTP (4-Nitrothiophenol) was measured and its decay rates are depicted in Figure 6.12. The strength of the SERS background is also dependent on the molecules adsorbed to the nanoparticles due to the difference in electrochemical potential [73]. The amino group of 4-ATP is more electron donating in comparison to the nitro group of 4-NTP [93]. Consequently, the background decay rates should decrease or invert. Similar to the nitrogen atmosphere, $\langle k_{\mathrm{BGND}} \rangle$ shrinks for this sample. However, due to the fabrication process, the density of nanoflowers on the sample is low, resulting in a comparatively weaker overall background signal than that of the 4-NTP sample. This introduces strong noise in the decay rates. Hence, this measurement should be redone with higher nanoparticle density to validate the differences in $\langle k_{\mathrm{BGND}} \rangle$.

On the other hand, the sample with gold nanoflowers on glass also used in section 4.2 consists of big gold clusters. It is not coated with additional molecules and glass is an insulator, contrary to Si, making it a good candidate for additional investigations. The measurement presented in Figure 6.8 is the only kinetic measurement of the sample so far. The extremely low laser power does not allow comparison of the decay rates to the other samples. Hence, additional kinetic SERS and PL measurements should be conducted. Also, after checking the decay rates without attached molecules, the sample could be coated with either 4-NTP or 4-ATP giving more insights into the role of the molecules and substrate.

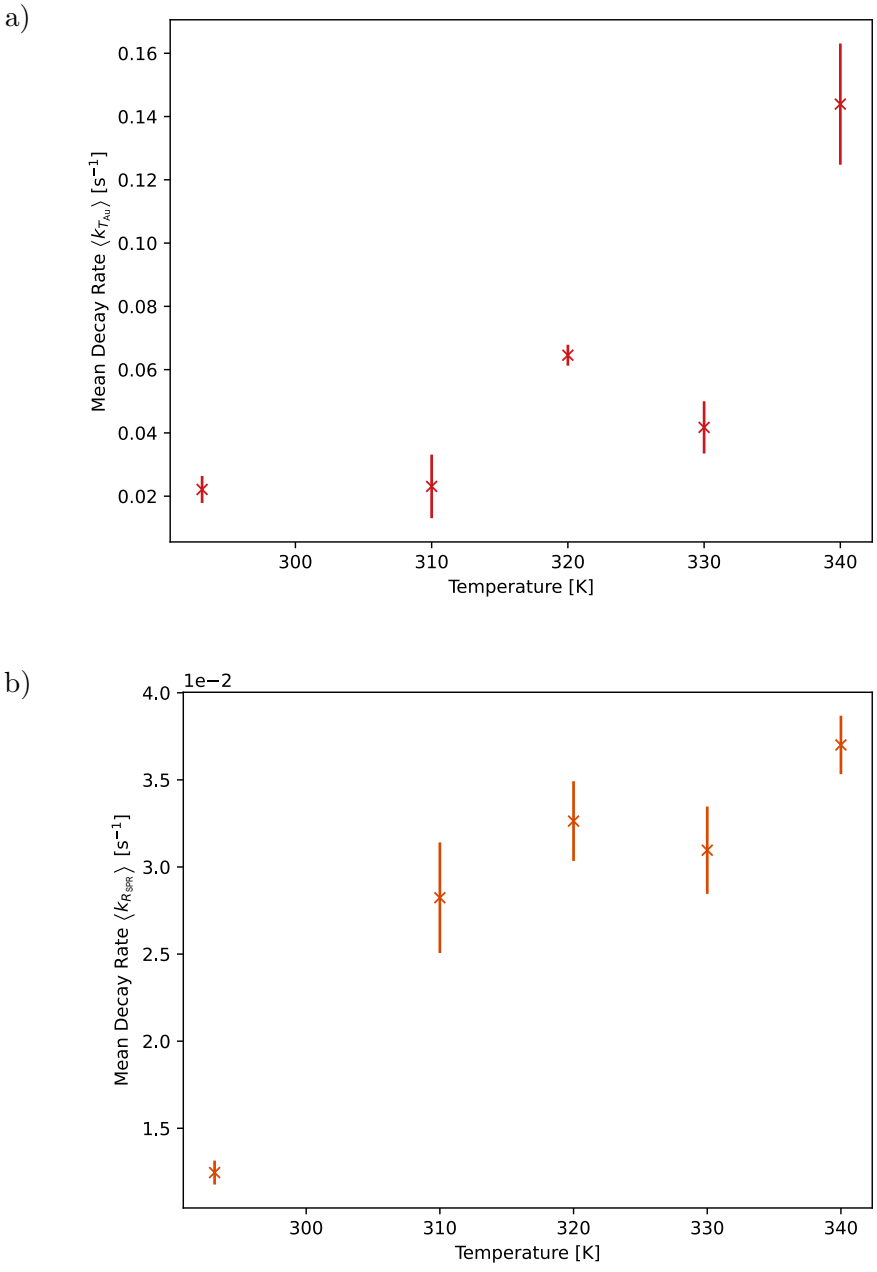

Figure 6.10: Mean decay rates of a) the nanoflower temperature $\langle k_{T_{\mathrm{Au}}} \rangle$ and b) the plasmonic enhancement ratios $\langle k_{R_{\mathrm{SPR}}} \rangle$ deduced from SERS spectra at different environmental temperatures, as presented in section 5.2. The error bars show the standard error of the mean between the different hot spots. The decay rates correspond to the fits shown in Figure A.4.

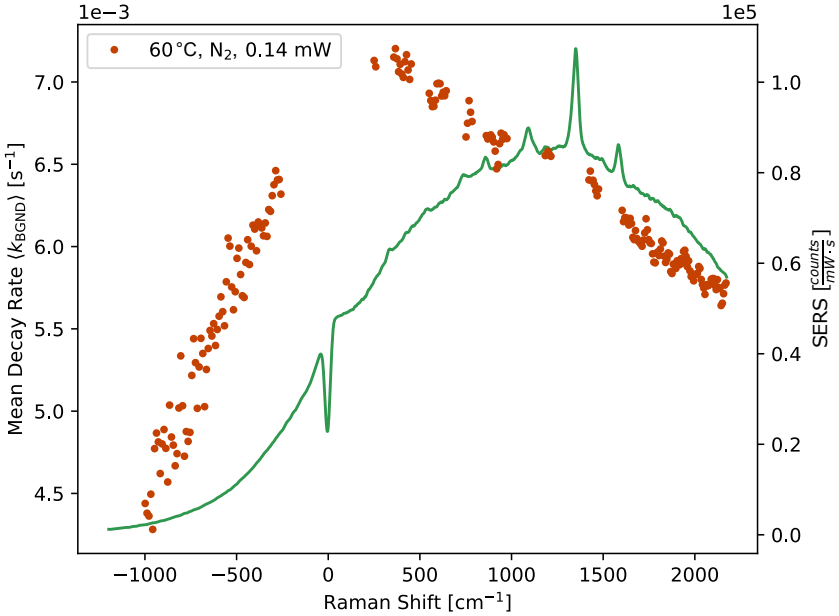

Figure 6.11: Spectral resolved mean decay rate $\langle k_{\mathrm{BGND}} \rangle$ for a kinetic SERS measurement of Au Nanoflowers in N_2-atmosphere at $T_{\mathrm{env}} = 60\,^{\circ}\mathrm{C}$ (333.15 K).

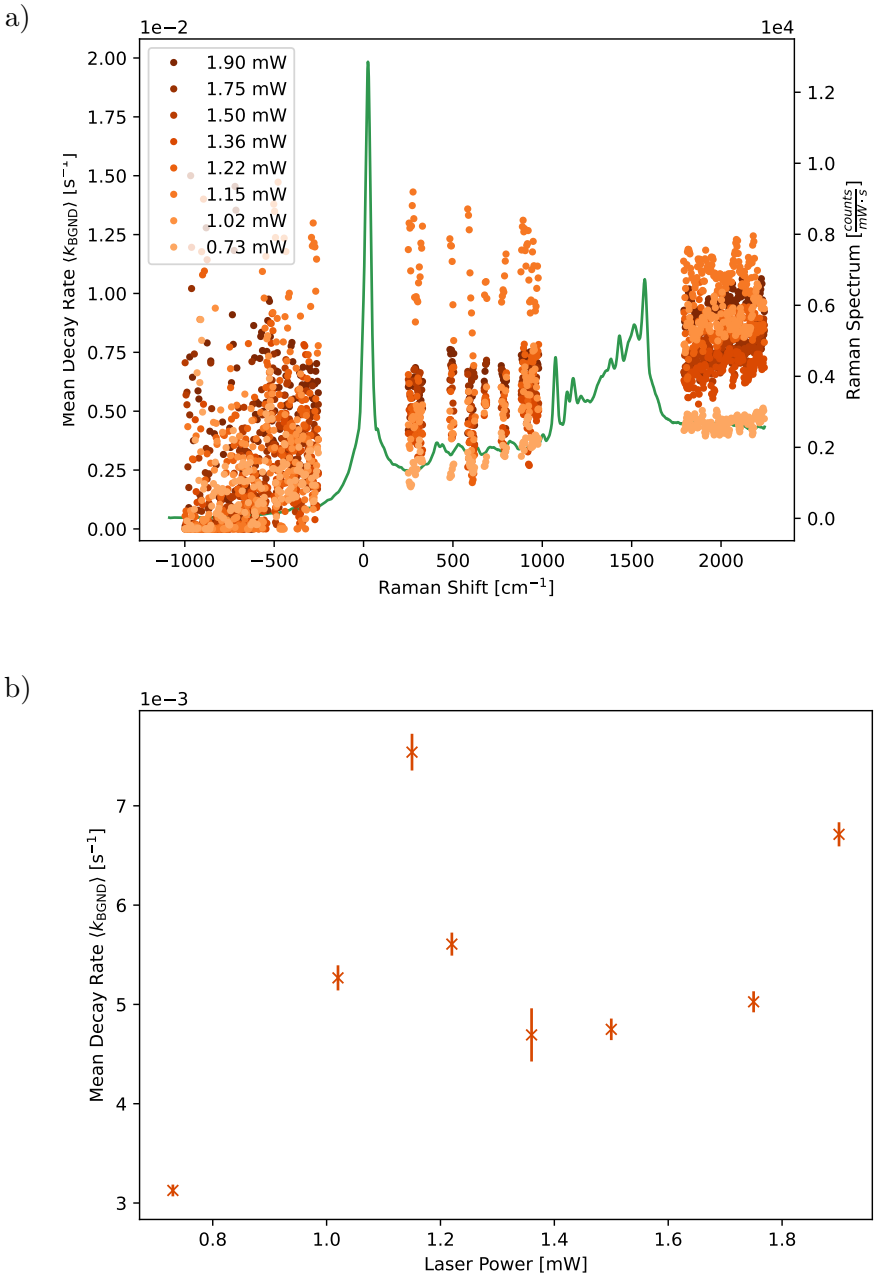

Figure 6.12: Mean decay rates $\langle k_{\mathrm{BGND}} \rangle$ of SERS spectra of Au nanoflowers coated with 4-ATP at different laser powers. a) shows the spectral resolved mean decay rates (orange) for distinct laser powers, as indicated by the legend. A representative SERS spectrum (green) is also depicted. In b), the average $\langle k_{\mathrm{BGND}} \rangle$ over all Raman shifts in the Stokes region are presented against the incident laser power. Error bars indicate the respective standard error of the mean.

6.5 Photoreaction

Furthermore, it can be demonstrated that the background decay operates independently of the photochemical reaction also induced by the irradiation. Therefore, the reaction from 4-NTP to DMAB is observed, see Koopman et al. [63] and Sarhan et al. [83] for more information about this reaction. The nanoflower response decay is triggered by low intensities at which the reaction rates and thus the changes of the molecular peak heights are not relevant as shown in Figure 6.13a). There is almost no DMAB peak visible at $1136\,\mathrm{cm}^{-1}$, which is the most pronounced. The reaction was accelerated directly afterward with a higher intensity in Figure 6.13b). The adsorbed 4-NTP molecules reacted, causing their corresponding peaks to decrease while the DMAB peaks raised. A change in the BGND is not observable since it could not recover in the meantime. This is further shown Figure 6.14 with $\langle k_{\mathrm{BGND}} \rangle$ presented for both measurements. However, this does not necessarily imply that the photoreaction has no impact on the SERS background. Charge transfer from the nanoparticles is the driving force in these reactions [10, 11, 13, 59, 77, 101]. Some kind of decay is expected in the course of the reactions, but this is no more influential than other transfer channels.

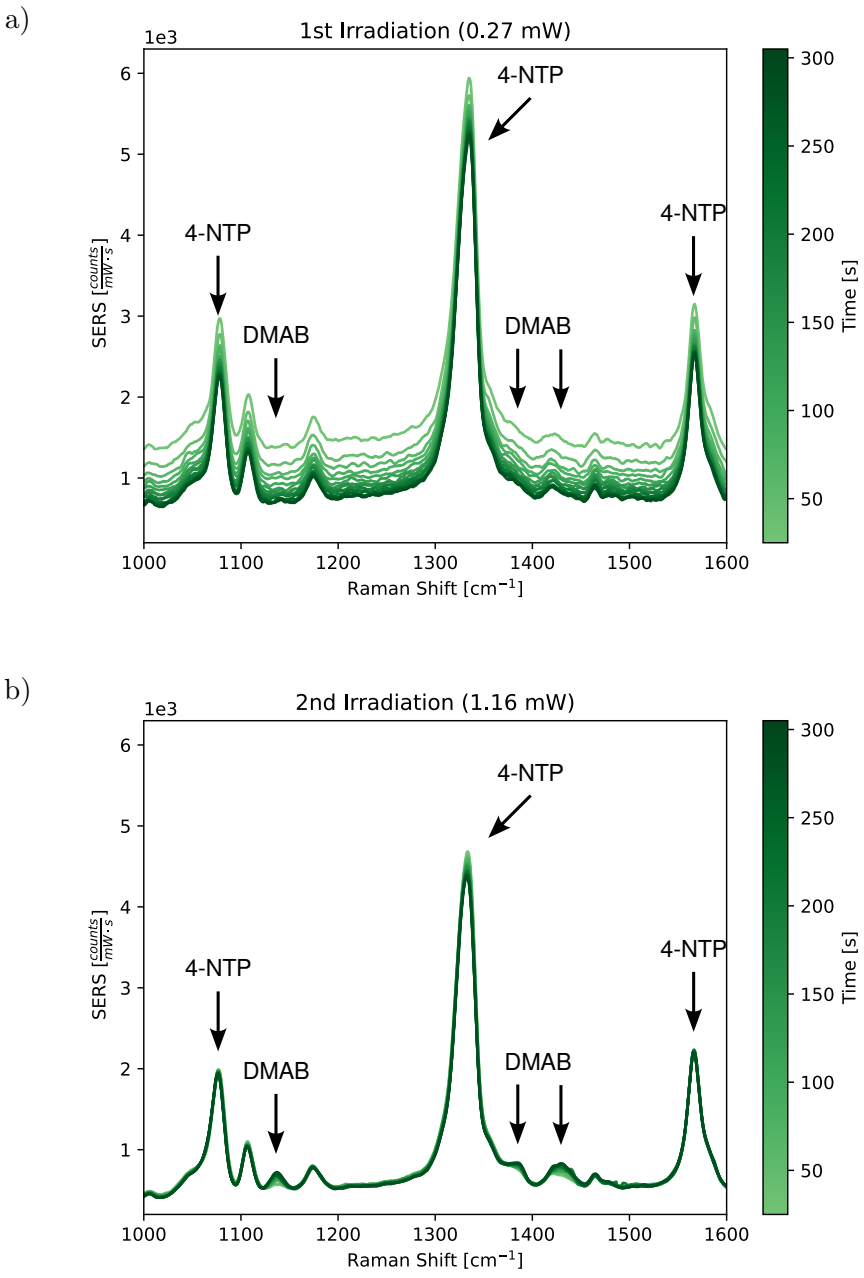

Figure 6.13: SERS spectra over time of irradiation of gold nanoflowers coated with 4-NTP. Positions of vibrational SERS peaks corresponding to 4-NTP and SERS are marked with arrows. a) The BGND decay is triggered with low laser power (0.27 mW), where nearly no reaction from 4-NTP to DMAB should be triggered. No DMAB peaks are clearly pronounced. b) Subsequent illumination with higher power (1.16 mW) raises the reaction rate to DMAB showing changes in the corresponding peaks. The BGND remains constant, as it already decayed into equilibrium.

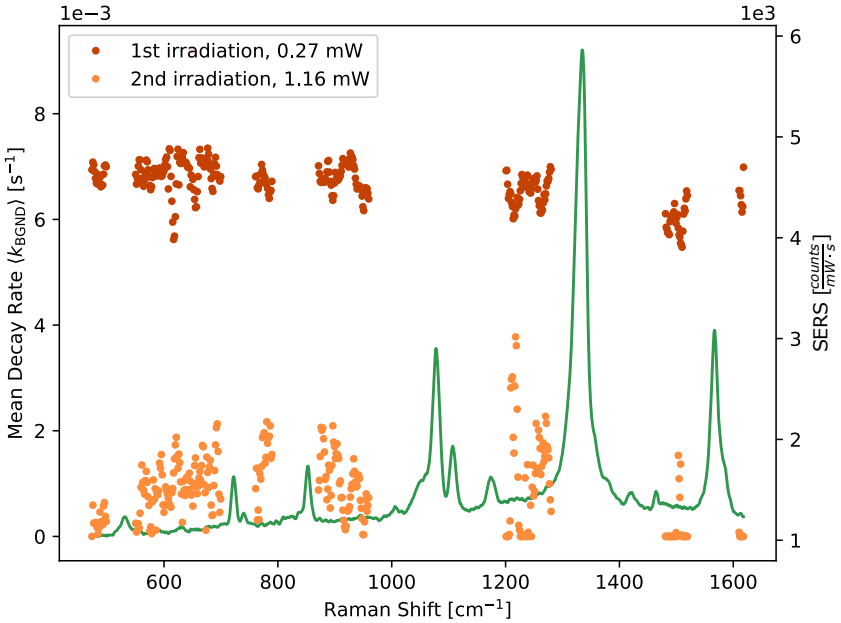

Figure 6.14: Spectrally resolved mean decay rates $\langle k_{\mathrm{BGND}} \rangle$ of both irradiation processes (orange) depicted in Figure 6.13, as indicated by the legend. A representative SERS spectrum (green) is also shown. $\langle k_{\mathrm{BGND}} \rangle$ vanishes in the second irradiation since there was almost no dark time between the measurements.

Chapter 7

Conclusions

This thesis investigated the always present background observed in SERS measurements, which arises from the response of the nanoparticles to the incident light [16, 49]. The dependence of clustered, high-faceted gold nanoflowers on various excitation wavelengths within the visible range was analyzed. Notably, the overall BGND signal's shape likely resembles the photonic density of states PDOS and, consequently, the localized surface plasmon resonance LSPR of the nanoflowers.This aligns with earlier studies [16, 33, 49]. However, a strong correlation between the overall signal strength and the incident photon energy was determined. With the aid of emission-dependent photoluminescence excitation (PLE) spectroscopy, this relationship is attributed to a substantial reliance on interband absorption. This aligns with literature showing that interband processes enhance the efficiency of nanoparticle emissions [16, 97]. Additionally, changes in the shape of the photoluminescence spectra were observed, which are contrary to the intraband-only emission processes, often presented in the literature [7, 33, 49, 82]. Thus, Auger processes, as proposed by Cai et al. [16], and inelastic interband reemission are suggested to enable excitation-dependent, Stokes-shifted, interband processes with visible emissions. Particularly emissions at shorter wavelengths are dominated by pure interband absorption. In contrast, emissions at high wavelengths can rely on additional, LSPR-enhanced absorption since an additional peak arises in the PLE spectra that overlaps well with the LSPR of the nanoflowers. This additional absorption can be attributed to either pure intraband processes or interband processes at the X-point. In this region, differences between the two analyzed samples were determined, that remain partially unresolved. Therefore, further analysis of distinct hot spots of gold nanoflowers is recommended. Clusters consisting of nanoparticles with simpler shapes, like nanospheres, offer further perspectives. This could improve the comprehension of the nanoparticle response due to their homogeneous single-particle LSPR while maintaining the strong enhancements of multimers [65].

Moreover, the anti-Stokes (AS) region of the nanoparticle response was investigated. Analysis of its power law indicates the significant reliance of AS emissions on the energetic electron distribution, in contrast to the Stokes region. This enables the extraction of information about the nanoparticles that are directly linked to their electron distribution. The temperature of the irradiated nanoparticle cluster and its close environment is commonly derived from the anti-Stokes signal [5, 15, 19, 49, 56, 94, 95]. Thus, an

expansion to the calibrated AS thermometry published by Xie and Cahill [95] was established. This advancement allows for the comparison of temperatures and SERS signals of different hot spots on inhomogeneous nanoparticle samples. As SERS facilitates non-destructive, time-resolved analysis of photocatalytic reactions, this approach holds the potential to be beneficial in experiments investigating the underlying physical and chemical mechanisms. This is particularly useful because high-faceted and clustered nanoparticles offer quite strong photocatalytic activity [14, 68, 96]. In kinetic measurements, an elevation in temperature occurring on the timescale of several minutes was noted. This could arise from the collective heating of surrounding nanoparticles [53, 58]. Hence, it is hypothesized that in this experiment the volume of nanoparticles the temperature is determined from is smaller than the volume of heated nanoparticles. Should this assumption hold true, the spatial recording capabilities of the setup can be optimized.

During each SERS and PL measurement, a decay of the nanoparticle background was observed over multiple minutes of irradiation. Different theories explaining the decay were considered. Currently, charge transfer from the nanoflowers into the environment is suspected to be the most likely. It is in agreement with the origin of the nanoparticle response and its dependence on electronic processes. Also, charge transfer is reversible matching the observations of this thesis. Additionally, a series of experiments was conducted to evaluate the impact of various properties of the environment and the incident light on the decay of the nanoflower response. It was demonstrated that the decay is not fully covered by the well-known charge transfer to adsorbed molecules for the purpose of photocatalysis. To quantify the decay, a Kohlrausch-William-Watts (KWW) function was employed. This approach includes the probability of multiple contributing decay channels and deviating decay rates from different nanoparticles in the illuminated cluster. This offers great utility. The decay rates are affected by examined aspects, including laser power, temperature, and chemical composition of the environment. In order to validate the observations, well-structured experiments need to reproduce them. Furthermore, if the total number of electrons is the crucial variable, electrochemical potentials in the close environment have to be investigated. Hence, different electron donors, like ethanol, and acceptors should be used in the environment of the nanoparticles and as adsorbed molecules. The impact of different shapes of nanoparticles would be of interest since it affects the hot carrier generation and thus possible charge transfers into the environment. Finally, excitations with high photon energies deviate from the otherwise uniform observations. The dependence on pure interband excitations in this regime changes the hot electron distribution and thus maybe the probability of the decay channels. In contrast, the shape of the emission spectra remains the same due to LSPR enhancement domination. In order to improve the picture of this nanoparticle BGND decay, the distributions of the decay rates against the emission wavelengths should also be examined more closely.

Appendix A

Supplementary Materials

A.1 Origin of the SERS Background

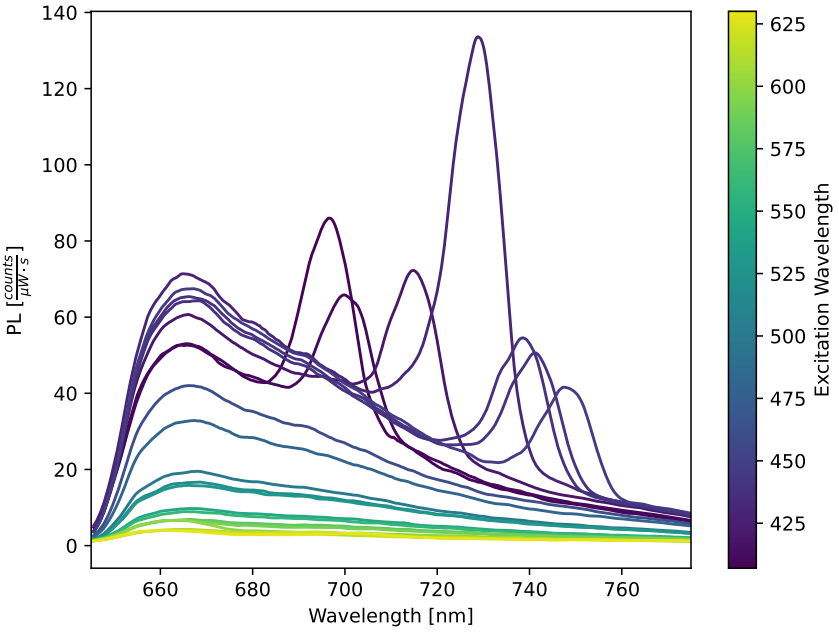

Figure A.1: Stokes gold nanoflower on glass photoluminescence (PL) spectra for several excitation wavelengths from 410 nm to 633 nm, as indicated by the color bar, with incident light blocked by a 650 nm long-pass filter in front of the spectrometer. All spectra have been measured at the same laser power at the sample and are shown normalized only to the laser power and exposure time of the spectrometer. Peaks shifting with the excitation wavelength between 700 and 750 nm originate from the light source. They vanish for higher excitation wavelengths since the light passes through a short-pass filter before hitting the sample blocking light above 750 nm. The overall signal strength shrinks with increasing excitation wavelengths.

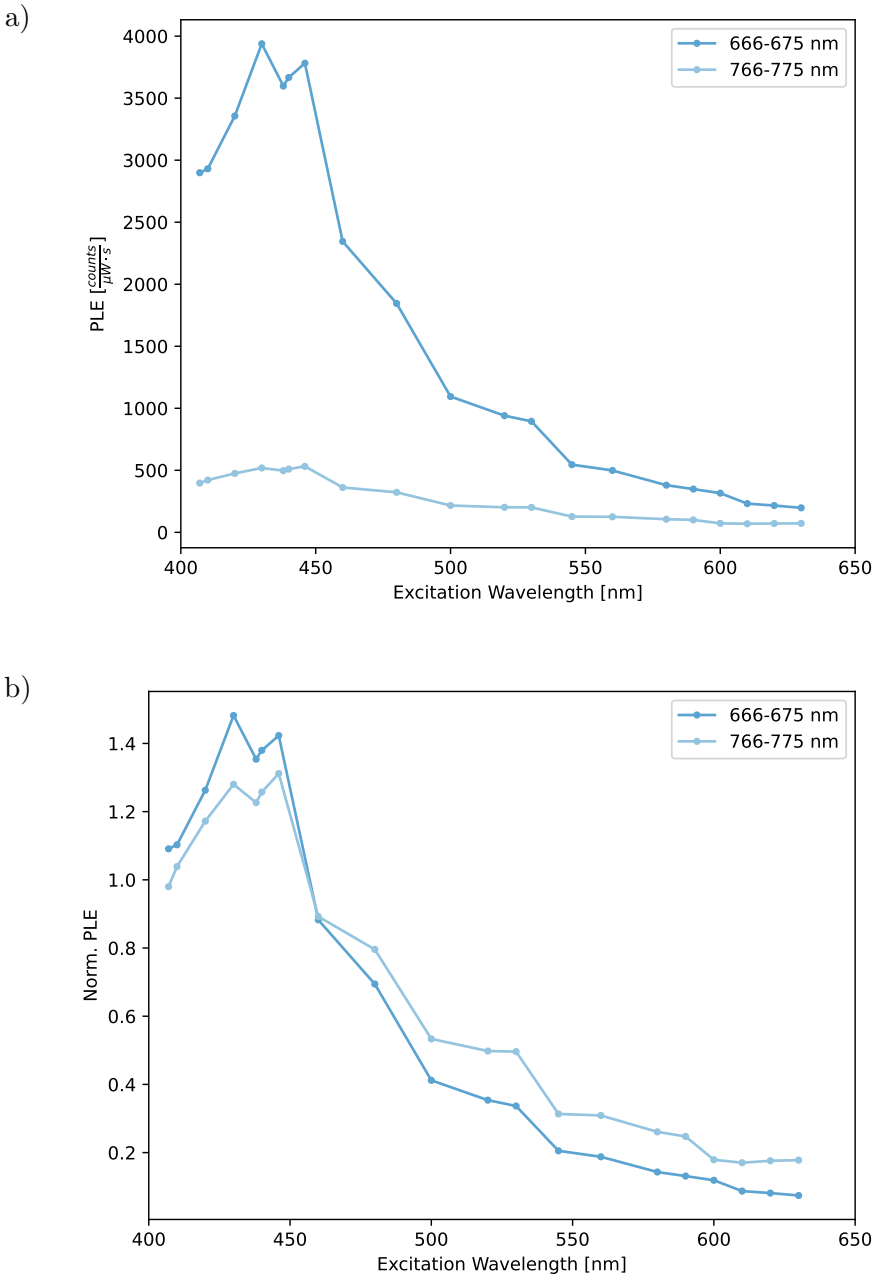

Figure A.2: Photoluminescence excitation (PLE) spectra of the Au nanoflowers on glass. To achieve this representation the photoluminescence spectra have been averaged over different ranges, as indicated by the legend, for each excitation wavelength. The region compromised by the laser feature (700 nm - 750 nm) was avoided. The PLE is shown in a) counts per laser power and exposure time and b) normalized to the average of the PLE in the excitation range from 445 nm to 495 nm.

a)

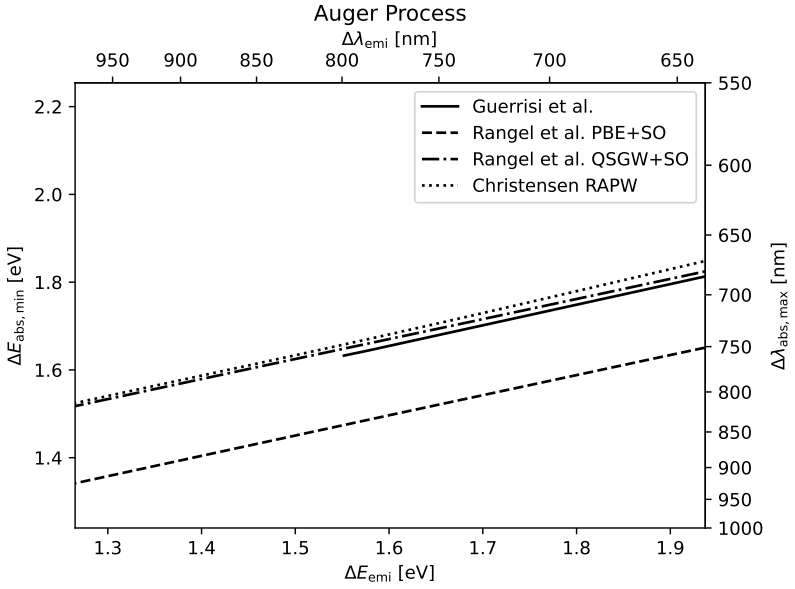

b)

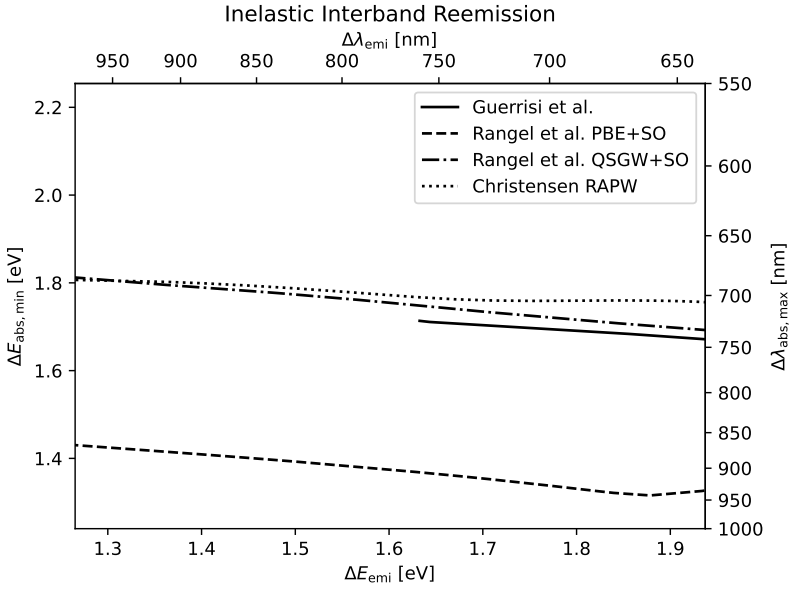

Figure A.3: Minimum required photon energy $\Delta E_{\mathrm{abs,min}}$ for emissions at energy ΔE_{emi} around the X-point with corresponding wavelengths $\Delta\lambda_{\mathrm{abs,max}}$ and $\Delta\lambda_{\mathrm{emi}}$ for a) Auger processes and b) inelastic interband reemission. The values are calculated via a) Equation 4.1-4.2 and b) Equation 4.3-4.4 from different band structures published by Guerrisi, Rosei, and Winsemius [41], Rangel et al. [81], and Christensen [25], as indicated by the legend. For the λ_{exc} used in this thesis, all emissions in the observed range are enabled.

A.2 Gold Nanoflowers as Thermometers

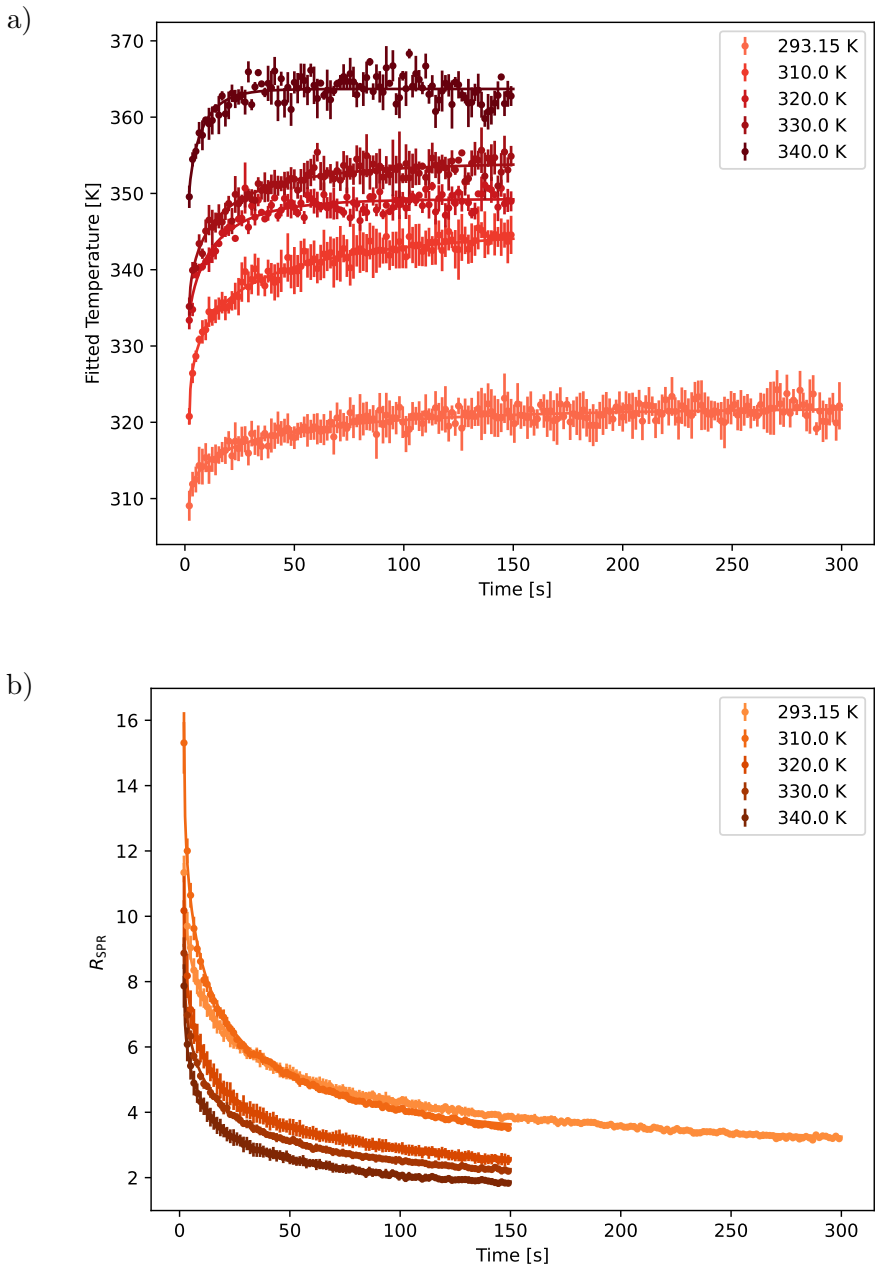

Figure A.4: a) Anti-Stokes temperatures T_{Au} (red dots) of the Au nanoflowers and b) plasmonic enhancement ratios R_{SPR} (orange dots) over time of irradiation for different environmental temperatures T_{env} as in Figure 5.5 and Figure 5.6, respectively, but with corresponding fits following Equation 6.1 (solid lines). Error bars show the standard error of the mean of all three spots measured at each T_{env}.

References

Literature

[1] W. Akemann and A. Otto. “Continuous secondary light emission from silver films: on the origin of the inelastic background in SERS”. *Surface Science* 307-309 (1994), pp. 1071–1075. DOI: 10.1016/0039-6028(94)91542-3 (cit. on pp. 1, 9, 23).

[2] Ramón A. Álvarez-Puebla. “Effects of the Excitation Wavelength on the SERS Spectrum”. *The journal of physical chemistry letters* 3.7 (2012), pp. 857–866. DOI: 10.1021/jz201625j (cit. on pp. 1, 5, 9).

[3] Gaspar Armelles et al. “Magnetoplasmonics: Combining Magnetic and Plasmonic Functionalities”. *Advanced Optical Materials* 1.1 (2013), pp. 10–35. DOI: 10.1002/adom.201200011 (cit. on p. 2).

[4] Sung-June Baek et al. “Baseline correction using asymmetrically reweighted penalized least squares smoothing”. *The Analyst* 140.1 (2015), pp. 250–257. DOI: 10.1039/c4an01061b (cit. on p. 38).

[5] Guillaume Baffou. “Anti-Stokes Thermometry in Nanoplasmonics”. *ACS nano* 15.4 (2021), pp. 5785–5792. DOI: 10.1021/acsnano.1c01112 (cit. on pp. 2, 12, 13, 41, 68).

[6] Stephen M. Barnett, Nadine Harris, and Jeremy J. Baumberg. “Molecules in the mirror: how SERS backgrounds arise from the quantum method of images”. *Physical chemistry chemical physics : PCCP* 16.14 (2014), pp. 6544–6549. DOI: 10.1039/c4cp00093e (cit. on pp. 1, 9, 38).

[7] Michael R. Beversluis, Alexandre Bouhelier, and Lukas Novotny. “Continuum generation from single gold nanostructures through near-field mediated intraband transitions”. *Physical Review B* 68.11 (2003). DOI: 10.1103/PhysRevB.68.115433 (cit. on pp. 1, 9, 23, 68).

[8] Ronald Birke. *Application of SERS for Nanomaterials*. Basel: MDPI - Multidisciplinary Digital Publishing Institute, 2022. DOI: 78733 (cit. on p. 4).

[9] Martin G. Blaber, Matthew D. Arnold, and Michael J. Ford. “Search for the Ideal Plasmonic Nanoshell: The Effects of Surface Scattering and Alternatives to Gold and Silver”. *The Journal of Physical Chemistry C* 113.8 (2009), pp. 3041–3045. DOI: 10.1021/jp810808h (cit. on pp. 8, 29, 32).

[10] Calvin Boerigter, Umar Aslam, and Suljo Linic. “Mechanism of Charge Transfer from Plasmonic Nanostructures to Chemically Attached Materials”. *ACS nano* 10.6 (2016), pp. 6108–6115. DOI: 10.1021/acsnano.6b01846 (cit. on pp. 1, 2, 5, 65).

[11] Calvin Boerigter et al. “Evidence and implications of direct charge excitation as the dominant mechanism in plasmon-mediated photocatalysis”. *Nature Communications* 7.1 (2016), p. 10545. DOI: 10.1038/ncomms10545 (cit. on pp. 1, 2, 5, 12, 65).

[12] Svetlana V. Boriskina et al. “Losses in plasmonics: from mitigating energy dissipation to embracing loss-enabled functionalities”. *Advances in Optics and Photonics* 9.4 (2017), p. 775. DOI: 10.1364/AOP.9.000775 (cit. on p. 8).

[13] Nathaniel C. Brandt, Emily L. Keller, and Renee R. Frontiera. “Ultrafast Surface-Enhanced Raman Probing of the Role of Hot Electrons in Plasmon-Driven Chemistry”. *The journal of physical chemistry letters* 7.16 (2016), pp. 3179–3185. DOI: 10.1021/acs.jpclett.6b01453 (cit. on pp. 2, 5, 65).

[14] Nathan D. Burrows et al. “Anisotropic Nanoparticles and Anisotropic Surface Chemistry”. *The journal of physical chemistry letters* 7.4 (2016), pp. 632–641. DOI: 10.1021/acs.jpclett.5b02205 (cit. on pp. 1, 6, 21, 38, 69).

[15] Yi-Yu Cai et al. “Anti-Stokes Emission from Hot Carriers in Gold Nanorods”. *Nano letters* 19.2 (2019), pp. 1067–1073. DOI: 10.1021/acs.nanolett.8b04359 (cit. on pp. 2, 11–14, 39, 41, 68).

[16] Yi-Yu Cai et al. “Light emission from plasmonic nanostructures”. *The Journal of Chemical Physics* 155.6 (2021), p. 060901. DOI: 10.1063/5.0053320 (cit. on pp. 1, 5, 9, 10, 21, 23, 25, 29, 31, 34, 38, 52, 68).

[17] Yi-Yu Cai et al. “Photoluminescence of Gold Nanorods: Purcell Effect Enhanced Emission from Hot Carriers”. *ACS nano* 12.2 (2018), pp. 976–985. DOI: 10.1021/acsnano.7b07402 (cit. on p. 9).

[18] Pedro H.C. Camargo and Emiliano Cortés, eds. *Plasmonic Catalysis: From Fundamentals to Applications*. 1. Auflage. Weinheim: Wiley-VCH GmbH, 2021. URL: http://nbn-resolving.org/urn:nbn:de:bsz:31-epflicht-1857020 (cit. on p. 1).

[19] Aquiles Carattino, Martín Caldarola, and Michel Orrit. “Gold Nanoparticles as Absolute Nanothermometers”. *Nano letters* 18.2 (2018), pp. 874–880. DOI: 10.1021/acs.nanolett.7b04145 (cit. on pp. 2, 12–14, 41, 68).

[20] R. Carles et al. “Plasmon-resonant Raman spectroscopy in metallic nanoparticles: Surface-enhanced scattering by electronic excitations”. *Physical Review B* 92.17 (2015). DOI: 10.1103/PhysRevB.92.174302 (cit. on pp. 5, 25).

[21] Jixing Chen et al. “Interior Melting of Rapidly Heated Gold Nanoparticles”. *The journal of physical chemistry letters* 12.34 (2021), pp. 8170–8177. DOI: 10.1021/acs.jpclett.1c02081 (cit. on p. 52).

[22] Oscar Hsu-Cheng Cheng, Dong Hee Son, and Matthew Sheldon. “Light-induced magnetism in plasmonic gold nanoparticles”. *Nature Photonics* 14.6 (2020), pp. 365–368. DOI: 10.1038/s41566-020-0603-3 (cit. on p. 2).

[23] Yuqing Cheng et al. “Luminescence quantum yields of gold nanoparticles varying with excitation wavelengths”. *Nanoscale* 8.4 (2016), pp. 2188–2194. DOI: 10.1039/C5NR07343J (cit. on pp. 1, 9, 38).

[24] Han-Kyu Choi et al. “Metal-Catalyzed Chemical Reaction of Single Molecules Directly Probed by Vibrational Spectroscopy”. *Journal of the American Chemical Society* 138.13 (2016), pp. 4673–4684. DOI: 10.1021/jacs.6b01865 (cit. on pp. 1, 4, 5).

[25] N. E. Christensen. “High-energy band structure of gold”. *Physical Review B* 13.6 (1976), pp. 2698–2701. DOI: 10.1103/PhysRevB.13.2698 (cit. on pp. 35, 37, 72).

[26] Kevin T. Crampton et al. “Junction Plasmon Driven Population Inversion of Molecular Vibrations: A Picosecond Surface-Enhanced Raman Spectroscopy Study”. *Nano letters* 18.9 (2018), pp. 5791–5796. DOI: 10.1021/acs.nanolett.8b02438 (cit. on pp. 1, 9, 23).

[27] Gobind Das et al. “Nano-patterned SERS substrate: application for protein analysis vs. temperature”. *Biosensors & bioelectronics* 24.6 (2009), pp. 1693–1699. DOI: 10.1016/j.bios.2008.08.050 (cit. on pp. 1, 4).

[28] S. Dey et al. “Observation and analysis of Fano-like lineshapes in the Raman spectra of molecules adsorbed at metal interfaces”. *Physical Review B* 93.3 (2016). DOI: 10.1103/physrevb.93.035411 (cit. on pp. 1, 9, 23).

[29] Robert H. Doremus. “Optical Properties of Small Gold Particles”. *The Journal of Chemical Physics* 40.8 (1964), pp. 2389–2396. DOI: 10.1063/1.1725519 (cit. on p. 44).

[30] Mildred Dresselhaus et al. *Solid State Properties*. Berlin, Heidelberg: Springer Berlin Heidelberg, 2018. DOI: 10.1007/978-3-662-55922-2 (cit. on pp. 6–8).

[31] P. Englebienne. “Use of colloidal gold surface plasmon resonance peak shift to infer affinity constants from the interactions between protein antigens and antibodies specific for single or multiple epitopes”. *The Analyst* 123.7 (1998), pp. 1599–1603. DOI: 10.1039/a804010i (cit. on pp. 1, 4).

[32] William R. Erwin, Roderick C. I. MacKenzie, and Rizia Bardhan. “Understanding the Limits of Plasmonic Enhancement in Organic Photovoltaics”. *The Journal of Physical Chemistry C* 122.14 (2018), pp. 7859–7866. DOI: 10.1021/acs.jpcc.8b00786 (cit. on p. 2).

[33] Ying Fang et al. “Plasmon emission quantum yield of single gold nanorods as a function of aspect ratio”. *ACS nano* 6.8 (2012), pp. 7177–7184. DOI: 10.1021/nn3022469 (cit. on pp. 9, 21, 29, 31, 68).

[34] Cosmin Farcau and Simion Astilean. “Evidence of a surface plasmon-mediated mechanism in the generation of the SERS background”. *Chemical communications (Cambridge, England)* 47.13 (2011), pp. 3861–3863. DOI: 10.1039/c0cc05190j (cit. on p. 5).

[35] M. Fleischmann, P. J. Hendra, and A. J. McQuillan. “Raman spectra of pyridine adsorbed at a silver electrode”. *Chemical Physics Letters* 26.2 (1974), pp. 163–166. DOI: 10.1016/0009-2614(74)85388-1 (cit. on p. 1).

[36] T. E. Furtak and J. Reyes. “A critical analysis of theoretical models for the giant Raman effect from adsorbed molecules”. *Surface Science* 93.2-3 (1980), pp. 351–382. DOI: 10.1016/0039-6028(80)90270-8 (cit. on pp. 1, 9).

[37] M. Futamata, Y. Maruyama, and M. Ishikawa. “Local Electric Field and Scattering Cross Section of Ag Nanoparticles under Surface Plasmon Resonance by Finite Difference Time Domain Method”. *The Journal of Physical Chemistry B* 107.31 (2003), pp. 7607–7617. DOI: 10.1021/jp022399e (cit. on pp. 1, 10, 15, 32).

[38] Qiaoqiang Gan, Filbert J. Bartoli, and Zakya H. Kafafi. “Plasmonic-enhanced organic photovoltaics: breaking the 10% efficiency barrier”. *Advanced materials (Deerfield Beach, Fla.)* 25.17 (2013), pp. 2385–2396. DOI: 10.1002/adma.201203323 (cit. on p. 2).

[39] F. J. García-Vidal and J. B. Pendry. “Collective Theory for Surface Enhanced Raman Scattering”. *Physical Review Letters* 77.6 (1996), pp. 1163–1166. DOI: 10.1103/PhysRevLett.77.1163 (cit. on pp. 1, 10, 15, 32).

[40] Rudolf Gross and Achim Marx. *Festkörperphysik*. 2., aktualisierte Aufl. De Gruyter eBook-Paket Mathematik und Physik. Berlin: De Gruyter Oldenbourg, 2014. DOI: 10.1524/9783110358704 (cit. on p. 6).

[41] M. Guerrisi, R. Rosei, and P. Winsemius. “Splitting of the interband absorption edge in Au”. *Physical Review B* 12.2 (1975), pp. 557–563. DOI: 10.1103/physrevb.12.557 (cit. on pp. 25, 35, 37, 72).

[42] Amanda J. Haes et al. “Detection of a biomarker for Alzheimer’s disease from synthetic and clinical samples using a nanoscale optical biosensor”. *Journal of the American Chemical Society* 127.7 (2005), pp. 2264–2271. DOI: 10.1021/ja044087q (cit. on pp. 1, 4).

[43] Rebecca A. Halvorson and Peter J. Vikesland. “Surface-enhanced Raman spectroscopy (SERS) for environmental analyses”. *Environmental Science & Technology* 44.20 (2010), pp. 7749–7755. DOI: 10.1021/es101228z (cit. on p. 4).

[44] Weiming He et al. “Significant temperature effect on the LSPR properties of noble metal nanoparticles”. *Journal of Optics* 51.1 (2022), pp. 142–153. DOI: 10.1007/s12596-021-00766-z (cit. on p. 44).

[45] Yingbo He et al. “Surface enhanced anti-Stokes one-photon luminescence from single gold nanorods”. *Nanoscale* 7.2 (2015), pp. 577–582. DOI: 10.1039/C4NR04879B (cit. on pp. 13, 41).

[46] José Hodak, Ignacio Martini, and Gregory V. Hartland. “Ultrafast study of electron–phonon coupling in colloidal gold particles”. *Chemical Physics Letters* 284.1-2 (1998), pp. 135–141. DOI: 10.1016/S0009-2614(97)01369-9 (cit. on p. 52).

[47] Wenbo Hou and Stephen B. Cronin. “A Review of Surface Plasmon Resonance-Enhanced Photocatalysis”. *Advanced Functional Materials* 23.13 (2013), pp. 1612–1619. DOI: 10.1002/adfm.201202148 (cit. on pp. 1, 4, 5).

[48] Jingyu Huang et al. “Resonant secondary light emission from plasmonic Au nanostructures at high electron temperatures created by pulsed-laser excitation”. *Proceedings of the National Academy of Sciences of the United States of America* 111.3 (2014), pp. 906–911. DOI: 10.1073/pnas.1311477111 (cit. on pp. 12, 13).

[49] James T. Hugall and Jeremy J. Baumberg. "Demonstrating photoluminescence from Au is electronic inelastic light scattering of a plasmonic metal: the origin of SERS backgrounds". *Nano letters* 15.4 (2015), pp. 2600–2604. DOI: 10.1021/acs.nanolett.5b00146 (cit. on pp. 1, 2, 5, 9, 10, 12, 13, 21, 23, 41, 68).

[50] James T. Hugall, Jeremy J. Baumberg, and Sumeet Mahajan. "Disentangling the Peak and Background Signals in Surface-Enhanced Raman Scattering". *The Journal of Physical Chemistry C* 116.10 (2012), pp. 6184–6190. DOI: 10.1021/jp3002977 (cit. on pp. 1, 5, 38).

[51] Motoharu Inagaki et al. "Electronic and vibrational surface-enhanced Raman scattering: from atomically defined Au(111) and (100) to roughened Au". *Chemical science* 11.36 (2020), pp. 9807–9817. DOI: 10.1039/D0SC02976A (cit. on pp. 1, 9, 23).

[52] Susumu Inasawa, Masakazu Sugiyama, and Yukio Yamaguchi. "Laser-induced shape transformation of gold nanoparticles below the melting point: the effect of surface melting". *The Journal of Physical Chemistry B* 109.8 (2005), pp. 3104–3111. DOI: 10.1021/jp045167j (cit. on p. 52).

[53] Liselotte Jauffred et al. "Plasmonic Heating of Nanostructures". *Chemical reviews* 119.13 (2019), pp. 8087–8130. DOI: 10.1021/acs.chemrev.8b00738 (cit. on pp. 15, 44, 69).

[54] David L. Jeanmaire and Richard P. van Duyne. "Surface raman spectroelectrochemistry". *Journal of Electroanalytical Chemistry and Interfacial Electrochemistry* 84.1 (1977), pp. 1–20. DOI: 10.1016/S0022-0728(77)80224-6 (cit. on pp. 1, 4).

[55] Hanwen Jin et al. "Plasmon-Induced Hot Carriers from Interband and Intraband Transitions in Large Noble Metal Nanoparticles". *PRX Energy* 1.1 (2022), p. 013006. DOI: 10.1103/PRXEnergy.1.013006 (cit. on p. 33).

[56] Thomas Jollans et al. "Effective Electron Temperature Measurement Using Time-Resolved Anti-Stokes Photoluminescence". *The journal of physical chemistry. A* 124.34 (2020), pp. 6968–6976. DOI: 10.1021/acs.jpca.0c06671 (cit. on pp. 12, 13, 39, 41, 68).

[57] Yohji Kawasaki, Hiroshi Watanabe, and Takashi Uneyama. "A Note for Kohlrausch-Williams-Watts Relaxation Function". *Nihon Reoroji Gakkaishi* 39.3 (2011), pp. 127–131. DOI: 10.1678/rheology.39.127 (cit. on p. 54).

[58] Pawel Keblinski et al. "Limits of localized heating by electromagnetically excited nanoparticles". *Journal of Applied Physics* 100.5 (2006). DOI: 10.1063/1.2335783 (cit. on pp. 47, 69).

[59] Emily L. Keller and Renee R. Frontiera. "Ultrafast Nanoscale Raman Thermometry Proves Heating Is Not a Primary Mechanism for Plasmon-Driven Photocatalysis". *ACS nano* 12.6 (2018), pp. 5848–5855. DOI: 10.1021/acsnano.8b01809 (cit. on pp. 1, 2, 5, 65).

[60] Katrin Kneipp et al. “Near-infrared surface-enhanced Raman scattering can detect single molecules and observe ‘hot’ vibrational transitions”. *Journal of Raman Spectroscopy* 29.8 (1998), pp. 743–747. DOI: 10.1002/(SICI)1097-4555(199808)29:8{\textless}743::AID-JRS294{\textgreater}3.0.CO;2-M (cit. on pp. 1, 4, 5, 12).

[61] Katrin Kneipp et al. “Surface-enhanced Raman scattering and biophysics”. *Journal of Physics: Condensed Matter* 14.18 (2002), R597–R624. DOI: 10.1088/0953-8984/14/18/202 (cit. on p. 5).

[62] Krystyna Kolwas and Anastasiya Derkachova. “Impact of the Interband Transitions in Gold and Silver on the Dynamics of Propagating and Localized Surface Plasmons”. *Nanomaterials (Basel, Switzerland)* 10.7 (2020). DOI: 10.3390/nano10071411 (cit. on pp. 25, 35).

[63] Wouter Koopman et al. “Decoding the kinetic limitations of plasmon catalysis: the case of 4-nitrothiophenol dimerization”. *Nanoscale* 12.48 (2020), pp. 24411–24418. DOI: 10.1039/d0nr06039a (cit. on pp. 1, 5, 65).

[64] Joseph R. Lakowicz. *Principles of fluorescence spectroscopy*. 3. ed. Boston, MA: Springer Science+Business Media LLC, 2006. DOI: 10.1007/978-0-387-46312-4 (cit. on p. 54).

[65] Seunghoon Lee et al. “Core–Shell Bimetallic Nanoparticle Trimers for Efficient Light-to-Chemical Energy Conversion”. *ACS Energy Letters* 5.12 (2020), pp. 3881–3890. DOI: 10.1021/acsenergylett.0c02110 (cit. on pp. 1, 4, 10, 15, 32, 38, 68).

[66] Ming Li, Scott K. Cushing, and Nianqiang Wu. “Plasmon-enhanced optical sensors: a review”. *The Analyst* 140.2 (2015), pp. 386–406. DOI: 10.1039/c4an01079e (cit. on pp. 1, 4).

[67] Qi Li et al. “High surface-enhanced Raman scattering performance of individual gold nanoflowers and their application in live cell imaging”. *Small (Weinheim an der Bergstrasse, Germany)* 9.6 (2013), pp. 927–932. DOI: 10.1002/smll.201201065 (cit. on p. 4).

[68] Ferenc Liebig et al. “A new route to gold nanoflowers”. *Nanotechnology* 29.18 (2018), p. 185603. DOI: 10.1088/1361-6528/aaaffd (cit. on pp. 1, 6, 21, 38, 69).

[69] Kai-Qiang Lin et al. “Intraband Hot-Electron Photoluminescence from Single Silver Nanorods”. *ACS Photonics* 3.7 (2016), pp. 1248–1255. DOI: 10.1021/acsphotonics.6b00238 (cit. on pp. 1, 9, 23).

[70] Nathan C. Lindquist, Ariadne Tückmantel Bido, and Alexandre G. Brolo. “Single-Molecule SERS Hotspot Dynamics in Both Dry and Aqueous Environments”. *The Journal of Physical Chemistry C* 126.16 (2022), pp. 7117–7126. DOI: 10.1021/acs.jpcc.2c00319 (cit. on pp. 1, 4).

[71] Yu Liu, Eric N. Mills, and Russell J. Composto. “Tuning optical properties of gold nanorods in polymer films through thermal reshaping”. *Journal of Materials Chemistry* 19.18 (2009), p. 2704. DOI: 10.1039/b901782h (cit. on p. 52).

[72] L. A. Lyon et al. “Raman spectroscopy”. *Analytical Chemistry* 70.12 (1998), 341R–361R. DOI: 10.1021/a1980021p (cit. on p. 5).

[73] Sumeet Mahajan et al. “Understanding the Surface-Enhanced Raman Spectroscopy “Background””. *The Journal of Physical Chemistry C* 114.16 (2010), pp. 7242–7250. DOI: 10.1021/jp907197b (cit. on pp. 1, 5, 9, 61).

[74] Stefan A. Maier. *Plasmonics: Fundamentals and applications*. New York, NY: Springer, 2007. DOI: 10.1007/0-387-37825-1 (cit. on pp. 4, 5, 31).

[75] Jan Mertens et al. “How Light Is Emitted by Plasmonic Metals”. *Nano letters* 17.4 (2017), pp. 2568–2574. DOI: 10.1021/acs.nanolett.7b00332 (cit. on pp. 1, 9, 10, 23).

[76] Martin Moskovits. “Surface-enhanced Raman spectroscopy: a brief retrospective”. *Journal of Raman Spectroscopy* 36.6-7 (2005), pp. 485–496. DOI: 10.1002/jrs.1362 (cit. on pp. 1, 5, 8, 10, 15).

[77] Syed Mubeen et al. “An autonomous photosynthetic device in which all charge carriers derive from surface plasmons”. *Nature Nanotechnology* 8.4 (2013), pp. 247–251. DOI: 10.1038/nnano.2013.18 (cit. on pp. 2, 5, 65).

[78] Robert L. Olmon et al. “Optical dielectric function of gold”. *Physical Review B* 86.23 (2012), p. 235147. DOI: 10.1103/PhysRevB.86.235147 (cit. on pp. 7, 8, 29, 31, 32).

[79] Andreas Otto, Walter Akemann, and Annemarie Pucci. “Normal Bands in Surface-Enhanced Raman Scattering (SERS) and Their Relation to the Electron-Hole Pair Excitation Background in SERS”. *Israel Journal of Chemistry* 46.3 (2006), pp. 307–315. DOI: 10.1560/IJC{\textunderscore }46{\textunderscore }3{\textunderscore }307 (cit. on pp. 22, 55).

[80] Zhiwei Qiao, Haijun Feng, and Jian Zhou. “Molecular dynamics simulations on the melting of gold nanoparticles”. *Phase Transitions* 87.1 (2014), pp. 59–70. DOI: 10.1080/01411594.2013.798410 (cit. on p. 52).

[81] T. Rangel et al. “Band structure of gold from many-body perturbation theory”. *Physical Review B* 86.12 (2012), p. 125125. DOI: 10.1103/PhysRevB.86.125125 (cit. on pp. 35, 37, 72).

[82] Lukas Roloff et al. “Light Emission from Gold Nanoparticles under Ultrafast Near-Infrared Excitation: Thermal Radiation, Inelastic Light Scattering, or Multiphoton Luminescence?” *Nano letters* 17.12 (2017), pp. 7914–7919. DOI: 10.1021/acs.nanolett.7b04266 (cit. on pp. 1, 9, 23, 39, 68).

[83] Radwan M. Sarhan et al. “The importance of plasmonic heating for the plasmon-driven photodimerization of 4-nitrothiophenol”. *Scientific reports* 9.1 (2019), p. 3060. DOI: 10.1038/s41598-019-38627-2 (cit. on pp. 1, 16, 17, 65).

[84] R. Schürmann and I. Bald. “Real-time monitoring of plasmon induced dissociative electron transfer to the potential DNA radiosensitizer 8-bromoadenine”. *Nanoscale* 9.5 (2017), pp. 1951–1955. DOI: 10.1039/c6nr08695k (cit. on p. 5).

[85] Felix Stete. “Gold at the nanoscale: Doctoralthesis”. PhD thesis. Universität Potsdam, 2021. DOI: 10.25932/publishup-49605 (cit. on pp. 1, 4, 7, 9, 11, 12, 19, 20, 34).

[86] Jacek Szczerbiński et al. “Plasmon-Driven Photocatalysis Leads to Products Known from E-beam and X-ray-Induced Surface Chemistry”. *Nano letters* 18.11 (2018), pp. 6740–6749. DOI: 10.1021/acs.nanolett.8b02426 (cit. on pp. 1, 13, 14, 22, 41).

[87] Alexei Tcherniak et al. “One-Photon Plasmon Luminescence and Its Application to Correlation Spectroscopy as a Probe for Rotational and Translational Dynamics of Gold Nanorods”. *The Journal of Physical Chemistry C* 115.32 (2011), pp. 15938–15949. DOI: 10.1021/jp206203s (cit. on pp. 1, 38).

[88] Furong Tian et al. “Surface enhanced Raman scattering with gold nanoparticles: effect of particle shape”. *Anal. Methods* 6.22 (2014), pp. 9116–9123. DOI: 10.1039/C4AY02112F (cit. on pp. 1, 9).

[89] Jan Toporski, Thomas Dieing, and Olaf Hollricher. *Confocal Raman microscopy*. Second edition. Vol. volume 66. Springer series in surface sciences. Cham: Springer, 2018. DOI: 10.1007/978-3-319-75380-5 (cit. on p. 5).

[90] Daniel R. Ward et al. “Electromigrated nanoscale gaps for surface-enhanced Raman spectroscopy”. *Nano letters* 7.5 (2007), pp. 1396–1400. DOI: 10.1021/nl070625w (cit. on pp. 1, 10, 15, 32).

[91] Haoran Wei et al. “Improved Quantitative SERS Enabled by Surface Plasmon Enhanced Elastic Light Scattering”. *Analytical Chemistry* 90.5 (2018), pp. 3227–3237. DOI: 10.1021/acs.analchem.7b04667 (cit. on p. 44).

[92] Katherine A. Willets and Richard P. van Duyne. “Localized surface plasmon resonance spectroscopy and sensing”. *Annual review of physical chemistry* 58 (2007), pp. 267–297. DOI: 10.1146/annurev.physchem.58.032806.104607 (cit. on pp. 1, 4, 5, 9).

[93] Tom Wirtanen, Eduardo Rodrigo, and Siegfried R. Waldvogel. “Recent Advances in the Electrochemical Reduction of Substrates Involving N−O Bonds”. *Advanced Synthesis & Catalysis* 362.11 (2020), pp. 2088–2101. DOI: 10.1002/adsc.202000349 (cit. on p. 61).

[94] Shengxiang Wu et al. “The connection between plasmon decay dynamics and the surface enhanced Raman spectroscopy background: Inelastic scattering from non-thermal and hot carriers”. *Journal of Applied Physics* 129.17 (2021), p. 173103. DOI: 10.1063/5.0032763 (cit. on pp. 2, 12, 14, 22, 41, 44, 55, 68).

[95] Xu Xie and David G. Cahill. “Thermometry of plasmonic nanostructures by anti-Stokes electronic Raman scattering”. *Applied Physics Letters* 109.18 (2016), p. 183104. DOI: 10.1063/1.4966289 (cit. on pp. 2, 12, 13, 15, 41–43, 68, 69).

[96] Qingfeng Zhang and Hui Wang. “Facet-Dependent Catalytic Activities of Au Nanoparticles Enclosed by High-Index Facets”. *ACS Catalysis* 4.11 (2014), pp. 4027–4033. DOI: 10.1021/cs501445h (cit. on pp. 1, 6, 9, 21, 38, 69).

[97] Xinping Zhang et al. “Transient localized surface plasmon induced by femtosecond interband excitation in gold nanoparticles”. *Scientific Reports* 8.1 (2018), p. 10499. DOI: 10.1038/s41598-018-28909-6 (cit. on pp. 1, 10, 29, 38, 68).

[98] Xuming Zhang et al. “Plasmonic photocatalysis”. *Reports on Progress in Physics* 76.4 (2013), p. 046401. DOI: 10.1088/0034-4885/76/4/046401 (cit. on p. 52).

[99] Zhenglong Zhang. *Plasmonic Photocatalysis: Principles and Applications*. 1st ed. 2022. Nanoscience and Nanotechnology. Singapore: Springer Nature Singapore and Imprint Springer, 2022. DOI: 10.1007/978-981-19-5188-6 (cit. on pp. 1, 5, 6).

[100] Zhi-Min Zhang et al. "An intelligent background-correction algorithm for highly fluorescent samples in Raman spectroscopy". *Journal of Raman Spectroscopy* 41.6 (2010), pp. 659–669. DOI: 10.1002/jrs.2500 (cit. on p. 38).

[101] Zhaoke Zheng and Tetsuro Majima. "Nanoplasmonic Photoluminescence Spectroscopy at Single-Particle Level: Sensing for Ethanol Oxidation". *Angewandte Chemie (International ed. in English)* 55.8 (2016), pp. 2879–2883. DOI: 10.1002/anie.201511764 (cit. on pp. 2, 5, 65).

[102] Na Zhou et al. "Plasmon-enhanced light harvesting: applications in enhanced photocatalysis, photodynamic therapy and photovoltaics". *RSC Advances* 5.37 (2015), pp. 29076–29097. DOI: 10.1039/C5RA01819F (cit. on pp. 1, 2, 4).

[103] V. P. Zhukov, E. V. Chulkov, and P. M. Echenique. "Lifetimes of d holes in Cu and Au: Full-potential LMTO approach". *Physical Review B* 68.4 (2003). DOI: 10.1103/PhysRevB.68.045102 (cit. on p. 34).

[104] P. Zijlstra and M. Orrit. "Single metal nanoparticles: optical detection, spectroscopy and applications". *Reports on Progress in Physics* 74.10 (2011), p. 106401. DOI: 10.1088/0034-4885/74/10/106401 (cit. on pp. 1, 4, 5, 9, 10).

[105] Attilio Zilli. "Measuring and modelling the absolute optical cross-sections of individual nano-objects". PhD thesis. Cardiff: Cardiff University, 2018. URL: https://orca.cardiff.ac.uk/id/eprint/109908/ (cit. on p. 5).

[106] Alyssa B. Zrimsek et al. "Single-Molecule Chemistry with Surface- and Tip-Enhanced Raman Spectroscopy". *Chemical reviews* 117.11 (2017), pp. 7583–7613. DOI: 10.1021/acs.chemrev.6b00552 (cit. on pp. 1, 4, 5).

Declaration

I hereby declare and confirm that this thesis is entirely the result of my own original work. Where other sources of information have been used, they have been indicated as such and properly acknowledged. I further declare that this or similar work has not been submitted for credit elsewhere. This printed copy is identical to the submitted electronic version.

Universität Potsdam, October 18, 2023

Jan Kutschera